UNIVERSITY OF EXETER

DOCTORAL THESIS

Time-resolved imaging of magnetisation dynamics using x-ray holography with extended reference and autocorrelation by linear differential operator (HERALDO)

Author:

Nicholas Bukin

Supervisors:

Prof. Feodor Y. Ogrin

Prof. Gerrit van der Laan

Submitted by Nicholas Bukin to the University of Exeter

as a thesis for the degree of

Doctor of Philosophy in Physics

September 2018

I certify that all material in this thesis which is not my own work has been identified and that no material has previously been submitted and approved for the award of a degree by this or any other university.

Nicholas Bukin

April 2019

Abstract

Within this thesis the theory and practicality of the holography with extended reference autocorrelation by linear differential operator (HERALDO) technique will be presented and discussed in detail along with the results of a series of experiments performed on nano-scale magnetic elements using this technique. The aim was to investigate the static and dynamic time-dependent behaviour of thin-film square magnetic elements. The magnetic elements were predominantly Permalloy (Py) squares however some contained topological structures whilst others were formed from multiple square elements, creating a larger conjoined structure. Magnetic dynamics were studied by exciting the ground state of the magnetic elements with a pulsed Oersted field produced by applying an electronic pulse through the central signal line of an integrated co-planar waveguide (CPW) which supported the elements. These dynamics were then observed by utilising circularly polarised x-rays from synchrotron sources and exploiting the x-ray magnetic circular dichroism (XMCD) effect. The experimental set-up, data collection and analytical process for each experiment will be discussed in detail with a particular focus on the HERALDO technique and any remarkable results obtained on each of the samples. These results have been supplemented with micromagnetic simulations in order to gain a deeper understanding of what is causing the effects seen.

The results of the experiments show that for thicker Py elements ($>$50 nm) there is a complex three-dimensional structure to the magnetic states that exist within, specifically that out-of-plane magnetic moments are more prominent. Interpretation of the experimental results with micromagnetic simulations showed

that the square elements contained out-of-plane magnetic singularities at each corner of the square which could be switched in polarity by magnetic bullet-modes which propagate along the domain walls when the vortex core is excited to gyrate. In addition, when the element is exposed to a moderate strength magnetic field that remains below its saturation magnetisation strength the vortex core distorts into an extended domain wall-like region of both in-plane and out-of-plane magnetisation. Concerning simulations of an element with an off-centre topological structure (defect), when the vortex core gyrates, a series of events occur that cause the polarity of the core to switch. Regarding a structure formed of multiple elements, these samples are able to exhibit one of two ground states: an anti-vortex (AV) state or a continuous state. The continuous state was observed to result in a more regular vortex core gyration pattern. This result opens up potential for gyration synchronisation of multiple vortex cores which could overcome the limitations of current methods by allowing direct interaction between vortices via the exchange interaction, as opposed to the weaker stray field effects or complex nano-contact spin-torque driven devices.

Acknowledgements

Four years worth of work, summed up in a little under 200 pages and which could not have been possible without the support, advice and guidance of many wonderful people. And coffee, lots and lots of coffee. Firstly I would like to thank my supervisors Prof. Feodor Ogrin and Prof. Gerrit van der Laan for giving me the opportunity to study this PhD and allowing me to achieve my life goal of becoming a Doctor. From their guidance I am now ready to enter the real world with a career in R&D thanks to their efforts and expertise.

I also wish to thank everyone from the office of G7, in which I owned a desk for the entirety of my PhD, and individuals from the CDT office in G33 and Harrison building for all of the helpful advice and, shall we say, interesting conversations that kept me thinking outside of the box, allowing me to engage in self-reflection and ultimately keeping me sane. You all helped me through some very hard times and I wish you all the very best in the future. A special thank you to Dr. Rob Valkass for introducing me to LaTex. Trying to write this thesis in Microsoft Word would have likely, no, definitely threatened my continued existence on this planet. Another special thank you to Dr. Tom Loughran for his SEM/FIB dualbeam expertise and insightful knowledge on a plethora of subjects, ranging from academic all the way to ”other”.

The week-long synchrotron experiments wouldn't have been the same without Dr. Erick Burgos-Parra. Your expansive repertoire of memes made the 16-hour work days not only bearable but absolutely enjoyable. Keep being you, man, and thank yeeee!

To my parents I can only say thank you so much for all of your efforts that got me to where I am today. I literally couldn't have done this without you both.

Finally I want to thank my fiancée, who had to put up with me being somewhat of a troglodyte for a while in order to get this thesis written in time. You were always there when I needed you and loved and supported me to no end.

Apologies to anyone not personally mentioned but I'm not very good at writing these kinds of things and I don't want it dragging on for too long. Just know that I remember and appreciate everything that you/we did. Yes, including that.

Contents

List of Figures

List of Tables

Acronyms

AV anti-vortex.

CCD charge coupled device.

CPW co-planar waveguide.

DLS Diamond Light Source.

EBL electron-beam lithography.

ESRF European Synchrotron Radiation Facility.

FFT fast Fourier transform.

FIB focussed ion beam.

FTH Fourier transform holography.

HERALDO holography with extended reference autocorrelation by linear differential operator.

LLG Landau-Lifshitz-Gilbert.

MFM magnetic force microscopy.

MOKE magneto optical Kerr effect.

NC-STO nano-contact spin-torque oscillator.

PEEM photoelectron emission microscopy.

PMA perpendicular magnetic anisotropy.

POMS portable octopole magnet system.

Py Permalloy.

SEM scanning electron microscopy.

SOLEIL Source optimisée de lumière d'énergie intermédiaire du LURE.

STO spin-torque oscillator.

STXM scanning transmission x-ray microscopy.

TR-MOKE time-resolved magneto optical Kerr effect.

TR-TXM time-resolved transmission x-ray microscopy.

TR-XPEEM time-resolved x-ray photoemission electron microscopy.

TRSKM time-resolved scanning Kerr microscopy.

TXM transmission x-ray microscopy.

XMCD x-ray magnetic circular dichroism.

XMLD x-ray magnetic linear dichroism.

XPEEM x-ray photoelectron emission microscopy.

Chapter 1

Introduction

The study of magnetic vortex closure domains has been a topic of great interest within the scientific community over the past few decades due to their model behaviour and intriguing dynamic properties. These magnetic vortex domain states are most commonly found formed within nanoscale soft-magnetic thin-film elements of varying geometries, such as squares, rectangles and circles. The magnetic state behaves like a classical harmonic oscillator, offering a potential capability to produce novel spintronic devices with a highly tuneable frequency range, narrow linewidth and lower power draw compared to existing technologies [6, 7, 8, 9]. Whilst magnetic flux-closure domain states have been theorised to exist since the 1940's [10] it would not be until 1984 that they would be observed experimentally [11].

There are reports which investigated these nanoscale magnetic elements and point to their potential application in producing new magneto-electronic devices that could be used as non-volatile, high-density storage media [12, 13], create dynamic skyrmion excitations [14, 15, 16] and be used as magnetic vortex generators [7, 8, 9, 17]. One such structure that has the potential for use in creating non-volatile data storage devices are nanoscale thin-film elements which contain the Landau magnetic vortex flux-closure domain state [10, 18, 19]. By examining the full three-dimensional static configuration of this structure and the gyration

dynamics of the vortex core we can obtain a deeper fundamental understanding of how such a device might operate and what we can do to exploit these characteristics.

Magnetic Landau flux-closure vortex states within nanoscale elements are potentially well suited for use in making non-volatile magnetic storage media due to the stability of the vortex domain state since it is the lowest energy ground state these elements exhibit on this scale for soft magnetic materials. This means that the vortex state will not undergo a spontaneous change of state without the presence of a strong magnetic field. As their name implies, these structures contain a magnetic vortex core at its centre, an out-of-plane magnetised singularity within a region of in-plane magnetic vectors which curve around this core. The vortex has two possible states, known as its polarity; +1 (up) or -1 (down), and it is this property which leads to their potential for use in the storage of electronic information as bits. To make use of this property a direct control of the vortex core polarity is essential, in particular having the ability to switch the core from one polarity state to the other and back when necessary. This has been reported via multiple methods involving; physical defects within the magnetic element [20, 21, 22], application of an oscillating in-plane magnetic pulse [23, 24, 25, 26, 27], application of a rotating magnetic field [28] and using spin-polarised currents [29, 30, 31].

In order to further investigate alternative methods of achieving efficient vortex core polarity reversal, the gyration dynamics of the core must also be observed. However there exists only a few techniques available today with sufficient spatio-temporal resolutions to directly observe these dynamic effects. These techniques are XPEEM, STXM, FTH and HERALDO. This thesis will focus on the HERALDO technique, a form of x-ray holography that is closely related to FTH but with some improvements, particularly with the achievable spatial resolution, which will be explained in great detail in part of chapter 2.

X-ray FTH and HERALDO have some noted advantages over the other aforementioned techniques, particularly they can achieve comparable spatio-temporal

resolutions without the use of optics (lensless). This is significant because optics are often the limiting factor to the achievable spatial resolution of the obtained image since they have inherent imperfections, known as spherical and chromatic aberrations. In place of these optics, the lensless holographic techniques instead make use of a reference point in close proximity to the observed region, forming a diffraction pattern from the incident beam of coherent light (x-rays) that is mathematically reconstructed using the Fourier transform to obtain an image of the sample. This method is more robust against drifting of the x-ray beam compared to those using optics.

The work presented in this thesis aimed to experimentally observe the dynamics within Landau magnetic vortex core structures whilst investigating novel methods to achieve the synchronisation of an array of gyrating vortices and the manipulation of the vortex core polarity. Investigation was carried out using the x-ray HERALDO technique whilst simultaneously attempting to improve upon the attainable spatial resolution by way of optimising sample fabrication.

In chapter 2 the relevant theoretical concepts will be discussed that are required to understand the results presented within this thesis. This includes a general overview of the classical and quantum-mechanical origins of magnetism and how they relate to the formation of a Landau vortex closure domain state in nanoscale magnetic elements. Thereafter will be a section outlining the most popular techniques used for direct imaging of magnetic domains, their respective advantages and drawbacks and a comparison between them.

Chapter 3 will cover the processes used to fabricate the samples examined by HERALDO in this thesis. It also contains explanations behind the particular sample geometries chosen.

The first series of experiments that obtained time-resolved data on nanoscale magnetic elements and their vortex dynamics using the HERALDO technique are presented in chapter 4. These results were published and would form the basis of our experimental methodology for subsequent experiments.

Chapter 5, presents the series of experiments regarding a novel method for achieving vortex polarity control by use of a physical defect. The results discussed differ from other published material involving physical defects being used to control vortex polarity since the switching effect we investigated did not rely on the pinning of the vortex core itself to the defect, but rather of the domain walls during the gyration initiation cycle.

Chapter 6 contains the results and discussion of a series of experiments involving multiple magnetic square elements that were physically joined together by overlapping the corners of adjacent elements. This was in order to investigate a novel method of achieving vortex core gyration synchronisation and increasing the density of an array of elements that could be achieved.

The final section, chapter 7 reports on the results obtained from field-dependent imaging of the Landau state and the formation of a double-Landau state that is rarely seen in square geometries of thin-films. There will also be a discussion regarding the distortion of the vortex core that is observed only in thicker magnetic thin-films which was observed experimentally here.

Chapter 2

Background

Here we introduce, define and explain the necessary terms and concepts relating to magnetism imaging techniques and the principles of holography and using the HERALDO technique which will be relevant for this thesis. The chapter will be split into three main parts: the first detailing the theoretical side of the related concepts of magnetism, the second will cover imaging magnetic domains using x-rays along with alternative magnetic imaging techniques and their advantages/disadvantages and the third will cover holographic principles and using the HERALDO technique for imaging magnetic dynamics on the nanoscale.

2.1 Background Concepts of Ferromagnetism

2.1.1 Definitions of Magnetic Terms

Before we begin detailing the equations relevant to ferromagnetism it is important to define the magnetic terms that will be used throughout this thesis. First and foremost is that every material that is placed within an external magnetic field, **H**, acquires a magnetic moment. For this material, the dipole moment per unit volume, also known as the *magnetisation*, is defined by the vector **M**. For most materials, particularly diamagnets and paramagnets, **M** is proportional to **H**, the

relationship of which can be written as such:

$$\mathbf{M} = \chi \mathbf{H}, \tag{2.1}$$

where χ is called the *magnetic susceptibility* of the material and determines whether a material is attracted to or repelled by an external magnetic field. Diamagnetic materials have a negative susceptibility and therefore repel a magnetic field, whilst paramagnetic materials have a positive susceptibility and are thus attracted to a magnetic field. Both types of material require an external magnetic field in order to become magnetised in this way.

However, instead of **M** we usually derive the magnetisation of a material from Maxwell's equations like so:

$$\mathbf{B} = \mu_0(\mathbf{H} + \gamma_B \mathbf{M}), \tag{2.2}$$

where μ_0 is the magnetic permeability of free space and **B** is the induced magnetism within the material inside the external magnetic field, **H**. γ_B is a notation term introduced by Brown which allows conversion between SI units, where $\gamma_B = 1$, and Gaussian, cgs units where $\gamma_B = 4\pi$ [1]. If eq. (2.1) is fulfilled then we can rewrite it like so:

$$\mathbf{B} = \mu \mathbf{H}, \tag{2.3}$$

where μ is the magnetic permeability of the material and is defined as such:

$$\mu = \mu_0(1 + \gamma_B \chi), \tag{2.4}$$

where μ_0 is the permeability of free space and relates to the amount of resistance encountered when forming a magnetic field in a vacuum. For paramagnetic

materials, $\mu > \mu_0$ and for diamagnetic materials, $\mu < \mu_0$. Permeability is what defines a materials ability to retain a magnetic moment after exposure to an external field, **H**.

2.1.2 Ferromagnetism

Ferromagnetic materials are those that undergo a spontaneous magnetisation and do not interact linearly with external magnetic fields since the magnetisation, **M**, is not proportional to the externally applied field, **H**. Instead ferromagnetic magnetisation is dependent upon the history of the applied field, leading to a magnetic hysteresis within the material and therefore **M** may be non-zero when **H** $= 0$. Within this hysteresis there are three key terms. The first of which is called the *saturation magnetisation*, $\mathbf{M}_s$, which is the maximum value of magnetisation that a material can acquire when within an external magnetic field, **H**. The second term is the *coercivity*, $\mathbf{H}_c$, which represents the strength of applied magnetic field required to return the magnetisation to zero from a non-zero value. The final term is called *remanent magnetisation*, $\mathbf{M}_r$, and is the value of **M** when **H**$= 0$.

Saturation magnetisation is an intrinsic property of ferromagnetic materials and is temperature dependent: M_s decreases as temperature increases. If the material is heated to or beyond its *Curie temperature*, T_c, then the value of $\mathrm{M}_s = 0$ at zero applied field. In particular for Py, the ferromagnetic material investigated throughout this thesis, its value of $\mathrm{M}_s = 8e^5 A/m$.

2.1.3 Magnetic Domain Theory

The samples investigated in this thesis were nanoscale, square-shaped thin-films which contained a magnetic *Landau vortex closure domain state*. This magnetic structure is the ground state for samples of this size and geometry and forms in order to reduce the total internal magnetic energy of the sample, of which there are multiple energy terms that contribute to this. It is not exclusive to square

geometries however as it is also the ground state for similarly sized cylindrical elements, among other geometries.

In total there are four magnetic energy terms that govern the internal magnetic state of ferromagnetic materials. They are the *exchange energy*, *magnetostatic energy*, *magnetocrystalline anisotropy energy* and *Zeeman energy*. The total magnetic energy is defined as such:

$$E_{tot} = E_{ex} + E_{ms} + E_{ani} + E_{Zee}. \tag{2.5}$$

This equation denotes that the total magnetic energy of a material is the sum of the four separate energies: exchange (E_{ex}), magnetostatic (E_{ms}), anisotropy (E_{ani}) and Zeeman (E_{Zee}) energies respectively. The anisotropy term itself is the sum of all forms of anisotropy, such as shape, magnetorestrictive, volume and surface anisotropy. This thesis will only cover shape anisotropy since the other terms do not contribute significantly to the magnetic energy within the samples we used.

Exchange Interaction

Whilst paramagnetic and diamagnetic materials only interact with an externally applied magnetic field, the atomic spins within ferromagnetic materials interact with one another in such a way that they attempt to align neighbouring atomic spins in the same direction as itself. These spins are aligned by a force known as the *exchange interaction*, which can be expressed as an exchange energy between spins $\mathbf{S}_i$ and $\mathbf{S}_j$ like so:

$$E = -\sum_{ij}{}' J_{ij}\mathbf{S}_i \cdot \mathbf{S}_j - \sum_i g\mu_B \mathbf{S}_i \cdot \mathbf{H}, \tag{2.6}$$

where J_{ij} is the exchange integral and, when positive, results in a lower energy for making parallel spins, which is the case for ferromagnetic materials. The term

g is the Landé g factor and μ_B is the Bohr magneton, a constant which represents the magnetic moment of an electron resulting from either its orbital or spin angular momentum.

The exchange interaction is short ranged ($\sim$5 nm) and competes against thermal effects which introduces kinetic energy that disturbs the magnetic moments [32]. If the temperature goes above a critical value, known as the *Curie temperature*, the ferromagnet will become paramagnetic due to the local ordering of moments being disrupted.

Magnetostatic Energy

The magnetostatic self-energy term, also known as the dipole energy, represents the magnetic dipolar interaction between all spins within a material with each other. It relates to the demagnetising field that exists within a ferromagnetic material and is responsible for the division of a materials magnetisation into domains of locally aligned spins. Neighbouring domains may point in opposite directions to one another and contain a domain wall between them. This domain wall is the region of space between domains where the spins rotate from alignment with one domain to the next. The magnetostatic energy term competes directly with the exchange energy and has a much longer effective range, however it is orders of magnitude weaker.

If we consider a single domain material its exchange energy will be very low since all spins are aligned parallel to one another, however the magnetostatic energy will be very large which is undesirable. Dividing this single, uniform domain into multiple oppositely magnetised domains will greatly reduce the magnetostatic energy. The domain walls between each of the formed domains require an input of energy due to it competing with the exchange energy (i.e. forming a domain wall will increase the exchange energy due to the disruption of the local spins from aligning with each other). Therefore so long as the reduction in magnetostatic energy is greater than the energy gained from forming the domain wall between the

two domains, then the sample will form a multi-domain structure. This energy term is based on some of Maxwell's equations, particularly:

$$\bigtriangledown \cdot \mathbf{B} = 0, \tag{2.7}$$

where **B** is the magnetic induction defined in eq. (2.2). The magnetostatic energy can then be defined as such:

$$E_{ms} = -\frac{1}{2} \int \mathbf{M} \cdot \mathbf{B} d\tau, \tag{2.8}$$

where integration is performed over the entire ferromagnetic body. We can think of this energy term as the interaction of each dipole with the field created by the other dipoles, **B**. There is a factor of a half in order to prevent counting the interactions twice (i.e. A with B, and B with A) [1].

Let us then consider a film of magnetisation, **M**, from which a stray field, $\mathbf{H}_{stray}$, is created due to the surface magnetic charges that exist from the film's magnetisation. A field would exist within the film which has an equal amplitude to $\mathbf{H}_{stray}$, however in the opposite direction to **M**. This is called the *demagnetising field*, $\mathbf{H}_{demag}$. Assuming a magnetic material of homogeneous susceptibility, the demagnetising field can be characterised by the demagnetising factor, N. This factor is affected by the shape of the structure and is often approximated to an ellipsoid due to its convenience, since it is the only second degree structure that has a surface of a finite size [33]. The demagnetising field within a material is determined by:

$$\mathbf{H}_{demag} = -N \cdot \mathbf{M} = -\gamma_B D \cdot \mathbf{M}, \tag{2.9}$$

where $N = \gamma_B D$ and D are tensors. If **M** is parallel to one of the principal axes of the ellipsoid then both N and D are numbers, known as demagnetisation factors, of which the traces are γ_B and 1 respectively. This leads to the demag-

netising factors having values of $D_x = D_y = D_z = 1/3$ for a sphere and $D_z = 0$ whilst $D_x = D_y = 1/2$ for an infinite cylinder. We can substitute eq. (2.9) into eq. (2.8) to obtain an equation for the magnetostatic self-energy of a uniformly magnetised ellipsoid of volume V:

$$E_{dm} = \frac{1}{2}V(N_x {M_x}^2 + N_y {M_y}^2 + N_z {M_z}^2), \tag{2.10}$$

which is the *shape anisotropy* term. This term is particularly important for our thin-film samples since the demagnetising factors N_x and N_y are smaller than N_z and thus magnetisation tends to prefer alignment along the x and y axes (i.e. an in-plane magnetisation is preferred).

Zeeman Energy

The Zeeman energy term describes the energy change of magnetisation vectors within a magnetic material that occurs once an external magnetic field is applied across it. It can be calculated by using the equation:

$$E_{Zee} = -\mu_0 \int_V \mathbf{M} \cdot \mathbf{H} dV, \tag{2.11}$$

where **H** represents the external magnetic field and its interaction with the ferromagnetic materials internal magnetisation, **M**. μ_0 is the samples permeability and represents its ability to form and support a magnetic field: a larger value will lead to a more strongly magnetised sample and thus a higher saturating magnetisation value. This equation is for a uniform external field and depends only on the samples average magnetisation, not on its domain structure or sample shape [34]. Zeeman energy is reduced when the magnetisation within the sample aligns with the external field.

Anisotropy Energy

This energy term is a result of the spin-orbit interaction, specifically the electron orbits that are bound to the crystallographic structure of the material. Their interactions with electron spin causes them to prefer alignment along the crystallographic axis, which is well-defined. This creates a spatial preference of direction for magnetisation of the crystal, called the easy-axis, which has a lower energy requirement of formation than along other axes, denoted the hard-axis. This essentially makes it a direction-dependent energy term [1]. This term therefore represents the energy needed to rotate a magnetic vector from the easy axis to the direction of the hard axis. For cubic crystals, such as nickel and iron [1], there are multiple easy axes and we can define the cubic anisotropy energy density via the expression:

$$E_{cubic} = K_1({m_x}^2{m_y}^2 + {m_y}^2{m_z}^2 + {m_z}^2{m_x}^2) + K_2{m_x}^2{m_y}^2{m_z}^2, \tag{2.12}$$

where, the coefficients K_1 and K_2 can be found experimentally and are temperature dependent [1]. K can be taken to higher orders but is not necessary for ferromagnets at room temperature.

The magnetocrystalline anisotropy energy is relatively small compared to the exchange energy and is practically negligible in almost all ferromagnetic materials [1]. Within this thesis Py is the only ferromagnetic material that is used which is considered isotropic, therefore $K_1 = K_2 = 0$, thus there is no contribution from this anisotropy to the total energy.

2.1.4 Magnetic Domains

Once minimisation of total magnetic energy has been calculated using eq. (2.5) the ferromagnetic sample will likely create domains, this work was lead by Landau and Lifshitz [18]. As mentioned above, domains are regions within a magnetic

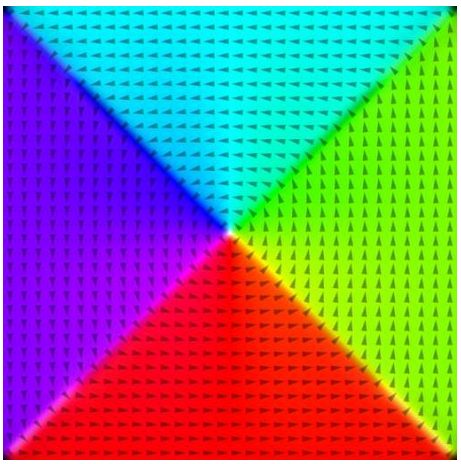

Figure 2.1: Simulated image of the Landau flux-closure domain state. Colour represents the direction of the in-plane magnetic vectors whilst white (black) represent out-of-plane vectors up (down). Note that the domain walls have pale (white) and dark (black) regions which implies they have an out-of-plane characteristic such as those seen in Bloch walls.

material where all neighbouring magnetic vectors align parallel to one another, whilst neighbouring domains may point in opposite directions or at any angle that is not parallel to one another. These domains are separated by domain walls: regions where the magnetisation vectors rotate from alignment with one domain to the next. If the sample is subjected to a bias field that is strong enough to saturate the sample, all domains will have their spins align parallel along the axis of the bias field, thus creating a uniformly magnetised sample.

Small elements, and even uniaxial crystals, tend to form 'open' magnetic structures where the overall sample magnetisation has a non-zero value in a zero-field environment which is due to their large anisotropy. Larger elements however tend to form 'closed' structures due to their smaller anisotropy. These closed structures have practically no overall magnetisation in zero-field since they are composed of equal magnitudes of magnetic vectors in all directions, resulting in them effectively cancelling each other out. An example of the magnetic Landau flux-closure domain state is displayed in fig. 2.1.

2.1.5 Domain Walls

Domain walls form between neighbouring domains within the Landau structures that are investigated within this thesis. As mentioned previously in section 2.1.3, the formation of magnetic domains is dominated by the magnetostatic self-energy term which acts over much longer distances than the exchange energy. Because of this, small angles between neighbouring spins can produce a large angle over a distance of many atoms, incurring a minimal exchange energy cost to domain formation. This region of spins rotating from alignment with one domain to the next is called a domain wall. The exchange energy tends to make domain walls as wide as possible as this reduces the angle between neighbouring spins, making them more in-line with one another, reducing the exchange energy.

We can modify eq. (2.6) to find the change in exchange energy when the nearest neighbouring spin is altered by a particular angle:

$$\varepsilon_{ex} = -\sum_{ij}{}' J_{i,j}\mathbf{S}_i \cdot \mathbf{S}_j = -JS^2 \sum_{neighbours} cos\phi_{i,j}, \tag{2.13}$$

where $\phi_{i,j}$ is the angle in radians between $\mathbf{S}_i$ and $\mathbf{S}_j$ and S is the spin number. If we consider a case where the direction of spins changes from $\phi = 0$ to π over N number of planes, where $\phi_{i,j} = \pi/N$, we can calculate the exchange energy loss like so:

$$\delta\varepsilon_{ex} = JS^2 n \sum_i (\frac{\pi}{N})^2 = \frac{JS^2 n\pi^2}{N}. \tag{2.14}$$

The loss in exchange energy over the wall is N times smaller than an immediate jump from $\phi = 0$ to $\phi = \pi$ [1]. If N is large enough then the loss in exchange energy can be small enough to be compensated by the magnetostatic energy gained from the domain wall formation, making the creation of domains favourable compared to a uniform magnetisation.

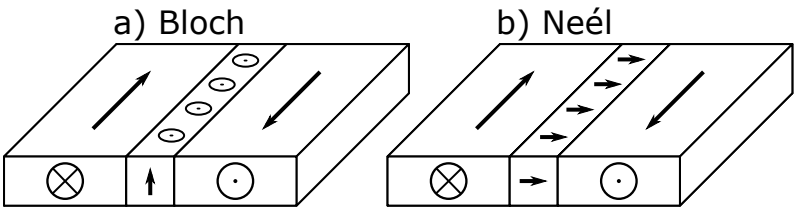

Figure 2.2: Sketch of a) a Bloch wall and b) a Néel wall. Within a Bloch wall the magnetisation vectors rotate out-of-plane whilst the vectors within a Néel wall rotate in-plane.

The complication is that in order to create these domains, a domain wall must be formed, and whilst the exchange energy of the spins may lie along the easy-axes, the wall will contain spins that turn towards one of the hard-axes, thus requiring the anisotropy energy to aid in domain wall formation. There is then a competition between the exchange energy desiring a thicker wall to minimise the angle between neighbouring spins, whilst the anisotropy energy tries to enforce a thinner wall.

Bloch and Néel Walls

There is a third determining factor to domain wall formation within thin-films: the thickness of the film, which affects the type of wall formed. The two types of domain wall that can be formed are *Néel* or *Bloch* walls, see fig. 2.2 to see a comparison between them. Néel walls comprise of an in-plane rotation of spins whilst Bloch walls utilise an out-of-plane rotation of spins in order to achieve rotation of the magnetic vectors in the space between the domains.

The most significant difference between the two types of domain wall is that the Néel wall has a volume magnetic charge and no surface magnetic charge, whilst the Bloch wall has a surface magnetic charge but no volume magnetic charge. Films that have a thickness greater than 50 nm tend to favour Bloch walls due to the increased ratio of volume compared to the surface area [1]. If the film is thinner than 50 nm then the surface magnetic charge will be larger, and thus less energetically favourable, than a volume magnetic charge due to its larger surface area compared to its volume size, leading to the formation of Néel walls. See

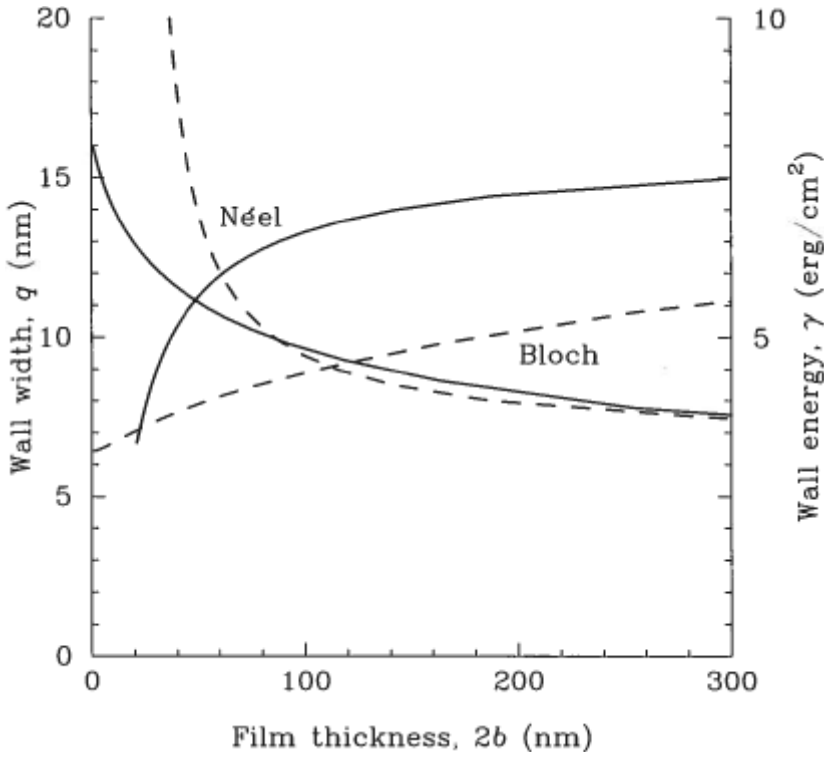

Figure 2.3: The domain wall width, q (dashed curves), and energy per unit wall area, γ, for Bloch and Néel walls in thin permalloy films. Figure taken from [1].

fig. 2.3 for a visual representation of domain wall energy and width as a function of permalloy film thickness. Note the crossover of domain wall energy (solid lines) at $\sim$50 nm.

The energy terms used in expressions for each wall type must be defined in terms of unit wall area instead of per unit wall length. The exchange energy per unit wall area, γ_{ex}, is defined as such:

$$\gamma_{ex} = \frac{\varepsilon_{ex}}{2b} = \frac{1}{2b}\int_{-b}^{b}\int_{-\infty}^{\infty}\omega_{ex}dxdy = \frac{\pi A}{q}(\sqrt{2}-1), \tag{2.15}$$

where ε_{ex} corresponds to the exchange energy per unit length, $2b$ is the film thickness, ω_{ex} is the exchange energy density, q is the wall width (an adjustable parameter) and A is the exchange energy constant [1]. This tells us that a thicker sample would reduce the exchange energy per unit wall area, γ_{ex}. Assuming the anisotropy is uniaxial, the anisotropy energy per unit wall area is then:

$$\gamma_{ani} = \frac{\varepsilon_{ani}}{2b} = \frac{1}{2b}\int_{-b}^{b}\int_{\infty}^{\infty}\omega_{uni}dxdy = \frac{\pi q}{2}K_1, \tag{2.16}$$

where, similarly, ε_{ani} is the anisotropy energy per unit length and ω_{uni} is the uniaxial anisotropy energy density. Overall a smaller wall width, q, would reduce ε_{ani} but increase γ_{ex}. In both of these expressions the energies do not depend on ϕ, the angle in radians that the spins make from the easy axis.

When $\phi = \frac{\pi}{2}$ the volume charge in the wall disappears which corresponds to a Bloch wall, whilst the surface charge vanishes when $\phi = 0$ for a Néel wall. There are therefore two solutions, one for the Bloch wall:

$$\gamma_{Bloch} = \frac{\pi C}{q}(\sqrt{2}-1) + \frac{\pi q}{2}K_1 + \frac{\pi^2 M_s^2 q^2}{b}log(1+\frac{b}{q}), \tag{2.17}$$

and another for the Neél wall:

$$\gamma_{Néel} = \frac{\pi C}{q}(\sqrt{2}-1) + \frac{\pi q}{2}K_1 + \pi^2 M_s^2 q^2[(1-\frac{q}{b}log(1+\frac{b}{q}))]. \tag{2.18}$$

In both cases the exchange energy term is attempting to make the wall width, q, as large as possible whilst the anisotropy term is trying to make the wall as small as possible [1]. The magnetostatic energy term, M_s, is less important here due to the dependence on film thickness, $2b$. Ultimately these equations can be reduced such that only the limit of $b \to \infty$ or $b \to 0$ can give a solution:

$$lim_{b\to 0}\gamma_{Néel} = lim_{b\to\infty}\gamma_{Bloch} = \pi\sqrt{2AK_1(\sqrt{2}-1)}. \tag{2.19}$$

If this equation is solved for both wall types we find that as film thickness increases, the energy of a Bloch wall decreases whilst for a Néel wall it increases. Wall widths also slowly increase (Bloch) and rapidly decrease (Néel) when film thickness increases. At roughly 50 nm film thickness the energy levels of the two wall types converge, therefore proving that samples below 50 nm preferentially

form Néel walls whilst samples thicker than 50 nm form Bloch walls. The widths of these walls are typically 30-100 nm for Néel walls and $>$30 nm for Bloch walls, increasing along with sample thickness in a somewhat linear fashion [35].

The Py samples used throughout this thesis had a structure of thickness 80 nm, therefore by using fig. 2.3 the domain walls are of the Bloch variety and have a width of $\sim$75 nm [1].

2.1.6 Landau-Lifshitz-Gilbert Equation

The Landau-Lifshitz-Gilbert (LLG) equation allows calculation of the dynamic magnetic precession that occurs within a magnetic sample once it is subjected to an external magnetic field. This equation combined the Landau-Lifshitz equation of magnetic precession, discovered in 1935 by Landau and Lifshits [18], with the damping effect discovered later in 1955 by Gilbert [36]. The dimensionless damping parameter, α, is necessary since without it the magnetic precession can be considered as infinite which is clearly unrealistic because magnetic precession decays over a finite period of time. The LLG equation is as follows:

$$\frac{d\mathbf{M}}{dt} = -\gamma_0 \mathbf{M} \times (\mathbf{H} - \alpha \frac{d\mathbf{M}}{dt}). \tag{2.20}$$

The first part of this equation, $-\gamma_0 \mathbf{M} \times \mathbf{H}$, contains the gyromagnetic ratio, γ_0, and describes the indefinite precessional motion of the magnetic moment around the applied external magnetic field, **H**. The second part, $-\alpha \frac{d\mathbf{M}}{dt}$, includes the damping term and describes the dampening of the magnetic precession such that its amplitude decays until magnetic equilibrium is reached when the magnetic moment, **M**, lies parallel along the applied field, **H**. The LLG equation allows us to find the time-dependent variation of magnetisation within a material directly from the quantum-mechanical expression of magnetisation precession in an effective magnetic field. Figure 2.4 shows the effect the damping parameter has upon the magnetisation vectors within a ferromagnetic material.

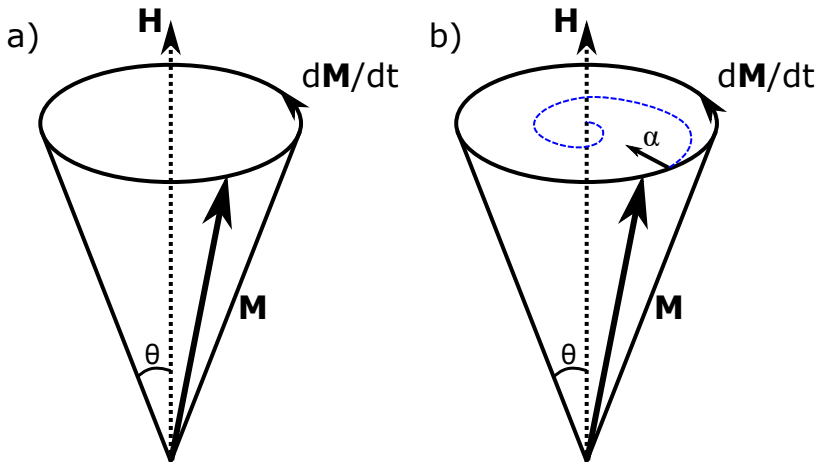

Figure 2.4: Sketch of magnetic precession within a ferromagnet when a bias field, **H**, is applied when the sample has either a) no damping term or b) with the damping term, α as shown in eq. (2.20).

The damping term is necessary to consider not only because it gives a more accurate representation of magnetisation dynamics within simulations, but using the correct value for the material in question is critical in determining what dynamics can be expected. This will become particularly important in chapter 5 since if the damping term is too high then the vortex switching effect is not observed, however if the damping value is below a critical value then defect-mediated vortex switching is observed. For Py the damping parameter is often cited as as being between 0.006 [37] and 0.01 [38], so a value of 0.008 was used for simulations throughout this thesis. Defect-mediated switching was observed in simulations using a damping coefficient of 0.012 or lower, however a value of 0.014 and higher was seen to not exhibit polarity switching for a defect 100 nm in diameter, 40 nm deep (from the sample surface) and 200 nm up (y-axis) from the centre of a 2000 nm x 2000 nm x 80 nm Py square element (discussed further in chapter 5).

2.2 Applications of the Landau Closure State

The Landau vortex flux-closure domain state that forms within nanoscale soft-magnetic elements is of interest because it behaves as a model system for the study of magnetic dynamics on the nanoscale. Acting like a harmonic oscillator,

the vortex core will gyrate when exposed to an external magnetic field according to the LLG equation and at particular frequencies based on sample geometry and material parameters. Since the development of techniques capable of observing magnetic contrast with sub-10 nm and sub-100 fs spatio-temporal resolutions, explained in section 2.3, investigation into the dynamics that occur on this scale are able to be made in order to gain a deeper understanding of magnetic interactions.

A potential practical application for patterned nanoscale magnetic elements which contain Landau flux-closure domain states is in high-density, non-volatile magnetic storage media [39]. Since the vortex core polarity can exist in one of two states: up (+1) and down (-1), it can be read like a binary bit with one polarity corresponding to a 0 state and the other to a 1 state. Multiple theoretical and experimental studies have proven that the vortex core polarity can be switched by using a variety of different methods. One such method involved applying a large out-of-plane bias field [40], others utilised spin-polarised alternating currents [29, 30] or an ultra-fast oscillating in-plane bias field [23, 24, 41, 42]. Having this level of control over the vortex polarity creates the potential for their use in such a non-volatile data storage device since the Landau vortex states within each magnetic element can be written to in order to store and change data. The chirality of the surrounding in-plane magnetism may curl counter-clockwise (+1) or clockwise (-1) around the vortex core. Whilst chirality is difficult to switch on a per-element basis, it is less pertinent when it comes to creating a device for non-volatile data storage since the data will be stored in the vortex core polarity and not necessarily the chirality.

Another potential use of the Landau vortex domain state is the generation of spin-waves. Wintz et. al. have reported that multiple stacked nanoscale square magnetic elements of different materials can achieve spin-wave generation and propagation when excited by a magnetic pulse [43]. The two square elements are separated by a non-magnetic layer and each contain a magnetic Landau closure-domain state. Once the system is excited by a magnetic pulse, spin waves are formed by the interaction of the two vortices which then propagate outwards from

the core gyration path. These spin waves can be directed along domain walls to the edge of the element [44], allowing potential applications for directing signal propagations of spin waves.

2.3 Magnetic Imaging Techniques

This section will introduce and summarise the popular x-ray-based techniques that are used in the observation of magnetic domains, along with a comparison between their advantages and limitations. Magneto-optical techniques will also be discussed to some extent since they are also prevalent for investigating magnetic dynamics. This comparison is provided in order to justify the use of HERALDO and highlight its advantages and limitations with regards to other available techniques.

2.3.1 Magneto-Optical Techniques

Magneto-optical microscopy techniques focus linearly polarised light onto the surface of a magnetic sample where the phase of the light becomes altered by the strength and orientation of the magnetism within the sample. The light leaving the sample now contains a small component of polarisation perpendicular to the incident polarisation. From this the samples response to an externally applied magnetic field can be measured without this field affecting the incident or reflected/transmitted light. The polarised light exploits either the Faraday effect when passing through a magnetic material [45], or the Kerr effect when reflected off the surface of a magnetic sample [46]. Kerr microscopy is more flexible since the samples do not need to be transparent to the incident light in order to observe the effect.

Kerr techniques such as time-resolved magneto optical Kerr effect (TR-MOKE) and time-resolved scanning Kerr microscopy (TRSKM) utilise a linearly polarised

monochromatic laser capable of emitting a probing pulse every few 100 fs [47, 48, 49, 50]. By introducing a time delay between when the probe pulse is incident upon the sample and when the magnetic pump pulse excites magnetic dynamics, this leads to time-resolved imaging of the magnetic dynamics, where the magneto optical Kerr effect (MOKE) signal is recorded at each delay time. This is known as *stroboscopic imaging*. Achieving stroboscopic measurements is used with many other techniques for observing magnetic domains and will be explained in more detail in section 3.2.

High temporal resolution makes this technique useful for observing ultrafast magnetic dynamics [48, 50]. This is an advantage over synchrotron-based x-ray techniques since they can only obtain a temporal resolution of up to 70 ps. Initiating magnetisation dynamics within the sample can be achieved directly via the laser light where it induces thermal demagnetisation within the sample by raising its temperature above its Curie point [51], or by use of an external magnetic field that is synchronised with or triggered by a laser [52].

One of the main limitations of these techniques however is their relatively low spatial resolution. Since spatial resolution is equal to half of the wavelength of the probing light used, typically in the 400-800 nm range, a spatial resolution of up to 200 nm is achievable. Another limitation is the short penetration depth of the light used, on the order of 10 nm, which only allows observation of surface effects. Furthermore, since optical transitions within the valence bands are rather unspecified, these techniques have limited chemical and elemental sensitivities [53].

2.3.2 Magnetic Force Microscopy (MFM)

Magnetic force microscopy (MFM) measures sample topography (i.e. surface roughness) and the magnetic moment that arises from the stray field leaving the sample surface [54, 55]. The tip of an MFM is ferromagnetic and is mounted to a cantilever spring, thus it responds to the stray fields above a flat magnetic sample.

In order to obtain an MFM image of the samples magnetic state, the tip is used in tapping mode to profile sample topography, after which it is raised to $\sim$30 nm above the sample surface in order to measure the stray field by re-scanning the previously scanned region. This allows direct mapping of the magnetic field relative to the sample geometry. As the tip is scanned above the sample surface it becomes displaced by the stray field. This displacement is on the order of several nanometres and is detected by a transducer, of which the most prominent utilise optical light reflecting off of the cantilever and into a split photodiode detector to measure the displacement.

Image quality and spatial resolution are both highly dependent on the physical quality and the magnetic coating of the tip, however spatial resolutions on the order of 10 nm have been achieved [56]. The most significant limitation with this technique however is that imaging cannot be made with an external field applied to the sample since this would affect the magnetic MFM tip during measurement. The technique also cannot observe the magnetic state within the bulk of the sample or of in-plane magnetism within the sample geometry.

2.3.3 X-ray Microscopy Techniques

One of the most significant steps for techniques that observe magnetic domains was the move from using visible-spectrum laser light as the probe to using x-rays generated from synchrotron facilities. This is because the spatial resolution that a technique is able to achieve is directly related to the half-wavelength of the probing light used. Since the wavelength of x-rays, 0.01-10 nm, are much shorter than those for visible-spectrum light, 400-800 nm, the techniques that utilise x-rays as the probe are able to achieve much higher spatial resolutions.

Synchrotron light sources are capable of producing sufficiently bright x-ray pulses by circulating one or multiple bunches of electrons around a ”storage ring”. The electron bunches are perturbed using magnets which generate a pulse of x-ray light, the process of which takes $\sim$70 ps and is the determining factor for

the achievable temporal resolution for synchrotron-based x-ray techniques [57]. These perturbing magnets may be dipoles, wigglers or undulators. Since the experiments in this thesis were performed at synchrotron beamlines that used undulators to produce the x-ray pulses only this magnet will be discussed.

Undulators produce a very bright beam that can be polarised by shifting the relative positions of the alternating magnets that make up the undulator. The x-ray beam is further characterised by use of a monochromator in order to select the required energy, allowing element-specific imaging to be performed. The beam is focussed to a spot size of several tens to several hundred microns by use of movable slits which lie along the beamline leading towards the sample chamber. The slits improve x-ray beam coherency and are adjustable in order to allow compensation for any changes which may occur over time [2]. X-ray beam energy, coherency and polarisation each affect the final magnetic contrast, therefore optimisation of the positions of the monochromator, slits and undulator respectively are necessary to achieve the best possible contrast.

X-ray Magnetic Circular Dichroism (XMCD)

The XMCD effect is capable of achieving magnetic contrast of a sample by forming two images, each from opposite x-ray polarisations, then subtracting one from the other. Two pairs of x-ray polarities are able to be used; linear (left-right and up-down) and circular (left-circular and right-circular). Both polarisations are used for observing magnetic materials, however x-ray magnetic linear dichroism (XMLD) is noted for achieving the observation of anti-ferromagnetic materials with x-rays. For a more comprehensive description of XMCD and XMLD please refer to these publications [58, 59, 60].

Since the discovery of XMCD [58, 59, 61] it has seen widespread use in observing magnetic samples with elemental-specificity in synchrotron techniques, most notably XPEEM, TXM, STXM and FTH. XMCD has a high sensitivity to the orientation and size of the magnetic moments within the observed material.

In 2003 XMCD was experimentally realised as a contrast mechanism for FTH in which coherent scattering from magnetic domains was recorded in a Gabor in-line geometry [62]. In the following year, off-axis imaging with FTH was first achieved and has since been proven to be a robust technique for directly observing magnetic domains in thin-film magnetic elements and multi-layered materials, so long as the sample substrate is suitably transparent to x-rays [63, 64].

XMCD is a useful contrast mechanism for use with magnetic materials, especially for $L_{2\rightarrow 3}$ transition metal absorption edges due to its intense signal and strong dichroic effect. The spectroscopic effect of dichroism describes the polarisation dependent absorption of light, specifically of x-rays for XMCD. X-rays are circularly polarised ”left” or ”right” which each interact differently with ferromagnetic materials to provide a contrast mechanism which allows one to quantitatively map the magnetisation of a sample. The left and right ”handedness” of the x-rays are switched between by use of an undulator within the synchrotron storage ring [2].

The XMCD effect operates on the absorbtion of x-rays by $3d$ transition metals by excitation of a $2p$ orbital electron into the higher energy $3d$ orbital which lies above the Fermi level, as shown in fig. 2.5a. The spin-orbit interaction states that the $2p$ orbital electrons are degenerate and split into two energy levels: $2p_{1/2}$ (L_2) and $2p_{3/2}$ (L_3). X-ray absorption, assuming a one-electron system where valence states exhibit Stoner splitting, is determined by the occupied density of states in the $2p$ core levels and the unoccupied density of states in the $3d$ levels above the Fermi energy [2]. When considering these $2p \rightarrow 3d$ transitions that occur due to excitation from absorption of circularly polarised x-rays, these transitions will now exhibit polarisation dependence due to selection rules and result in an observable contrast based on sample magnetisation direction [65].

For each x-ray polarisation, more electrons of one spin direction will absorb the x-rays and become excited into unoccupied $3d$ energy states than the electrons of opposite spin direction. XMCD thus determines the density of unoccupied

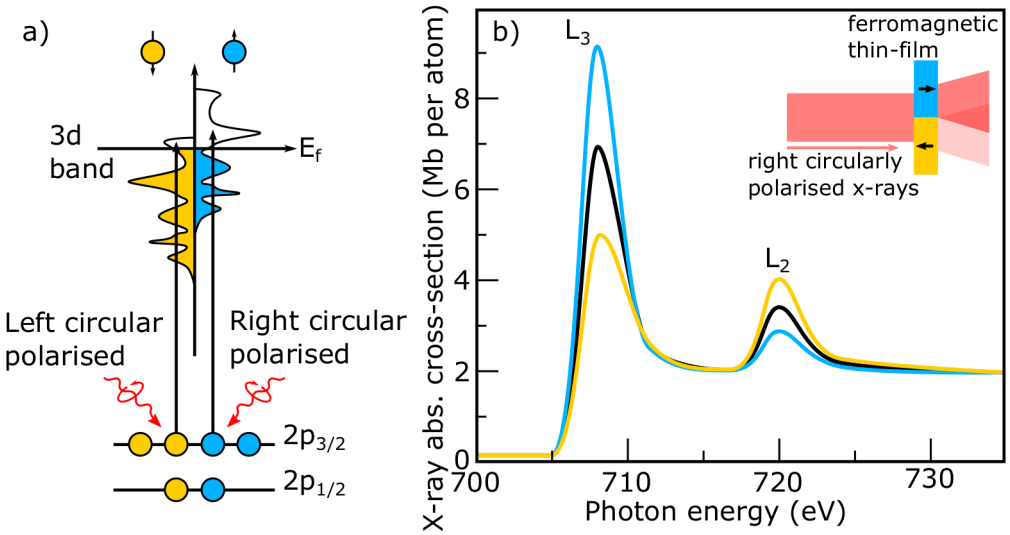

Figure 2.5: The XMCD effect illustrated for L-edge absorption, reproduced from [2]. a) $2p \rightarrow 3d$ transitions are spin dependent and thus the x-ray polarity determines which spin state is excited to beyond the Fermi energy level, E_f. X-ray absorption does not allow the spin to flip, therefore the measured resonant absorption intensity is directly proportional to the number of empty $3d$ states for a particular spin. b) Fe L-edge x-ray absorption spectrum, reproduced from [2]. Magnetic imaging with XMCD involves reversing the polarity of the x-rays whilst keeping the magnetisation within the sample fixed. We can also see the resonant absorption peaks at the L_2 and L_3 edges of Fe. Inset: visual depiction of the contrast mechanism that dichroism exhibits when used in magnetic imaging. X-rays of one polarisation have a stronger absorption in one magnetisation direction compared to others. Left circularly polarised light exhibits the same magnitude of effect however for magnetisation directions opposite to those of right polarised light. The difference between these leads to the measurement of the direction of magnetic domains.

$3d$ states for each spin polarisation. Ferromagnetic materials have a difference in the number of unoccupied $3d$ states for each spin polarisation, as shown in fig. 2.5a, therefore resulting in a distinct difference between absorption spectra for opposing x-ray circular polarities and allowing a direct quantification of spin magnetic moments within the material. A typical x-ray absorption spectra for Fe is shown in fig. 2.5b and illustrates the resonant absorptions at the L_2 and L_3 edges.

Element specificity can be achieved by adjusting the energy of the electrons to the L_3 x-ray absorption edge of the element that is to be observed. Particularly relevant examples are the Fe L_3 edge of $\sim$708 eV, Co of $\sim$782 eV and Ni of $\sim$860 eV.

2.3.4 Photoemission Electron Microscopy (PEEM)

A photoelectron emission microscopy (PEEM) instrument is closely related to an electron microscope in that they both rely upon focussing secondary electrons towards a CCD in order to form an image. The difference between them however is the method of secondary electron formation. Instead of secondary or backscattered electrons being generated from an incident beam of high-energy electrons like with an SEM, the secondary electrons are instead ejected by the material after having been excited to a higher energy state via photon absorption (i.e. optical excitation). Conventionally, PEEM uses UV-light as the source for generating these secondary electrons, however x-rays can be used instead in order to take advantage of the XMCD effect as its method of obtaining magnetic contrast, giving rise to the XPEEM technique.

PEEM and XPEEM extract and accelerate the electrons emitted from the sample surface into an objective lens by using an electric field. The photoemitted electrons are then focussed by a cathode lens, the resolution of which is limited by spherical and chromatic aberrations. The typical field-of-view ranges from $\sim$1 mm down to a few microns which is suitable for observing magnetic domains within micron and nano-scale magnetic elements. A schematic of an XPEEM is shown in fig. 2.6.

Time-resolved x-ray photoemission electron microscopy (TR-XPEEM) is a variation on regular XPEEM that can perform real-time observations of surface magnetisation dynamics within the picosecond regime by use of a stroboscopic pump-probe setup. This technique has been used to observe the nucleation and subsequent growth of reversed magnetic domains within a thin Py film at a spatial resolution of 20 nm [66]. Another experiment observed magnetic dynamics within Py rings down to a temporal resolution of 125 ps [67]. Temporal resolutions as low as 15 ps have been achieved when using TR-XPEEM to observe the magnetisation dynamics within rectangular Py structures [68].

Advantages of the XPEEM technique include its fast image acquisition time,

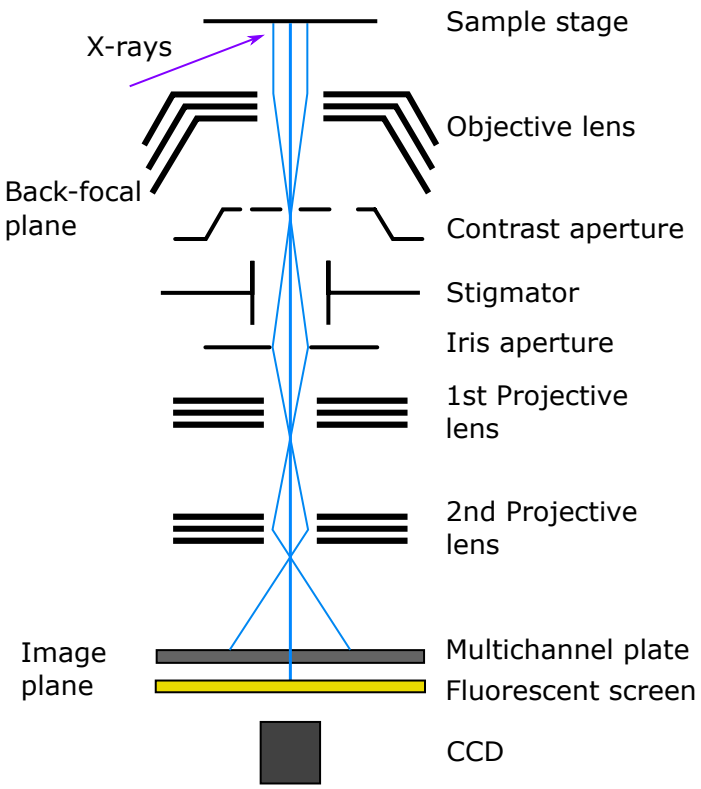

Figure 2.6: Schematic of XPEEM reproduced from [3]. Upon illumination with x-rays the sample emits secondary electrons which are drawn into the objective lens via the extractor. The electrons then pass through multiple lenses and stigmators before being projected onto a multichannel plate, a fluorescent screen and a CCD which captures the final image.

similar to that of an optical microscope, and its ability to image micron and nano-scale magnetic elements and domains with an average spatial resolution of 20 nm [53, 69]. XPEEM also does not require samples to be sufficiently thin in order to be transparent to x-rays since they only interact with the sample to a depth of $\sim$5 nm into the surface and are not transmitted through the sample.

One of the main drawbacks of this technique however is that external magnetic fields can not be applied near the sample as this will influence its domain structure. In order to overcome this problem an electrostatic lens is often used in place of an electromagnetic objective lens. Another limitation is the inability to probe the bulk of the sample since the image is formed by electrons that are emitted from only a few nm deep from the surface. Also the spatial resolution is limited by spherical and chromatic aberrations within the focussing lens.

2.3.5 Transmission X-ray Microscopy (TXM)

TXM techniques utilise Fresnel zone plates to focus the x-ray beam onto the sample where it then passes through the sample to a detector. Fresnel zone plates with opaque rings have been known about since 1871, however they were not a source of great interest to the scientific community at the time for multiple reasons, most notably the significant reduction in flux of the incident light through the plate [70]. However since the 1950's developments in transmission-based x-ray microscopy techniques utilising a Fresnel zone plate with transparent rings to diffract soft x-rays in order to observe microscopic structures began gaining traction [71, 72]. Today they are of great interest to the scientific community because they are able to form high resolution images which approach the diffraction limit of x-rays. These zone plates are typically fabricated by using electron beam lithography [73, 74]. The focussing properties of Fresnel zone plates are described in [71, 75].

There are two main types of zone plate-based microscopes that utilise x-rays: TXM and STXM, both of which are illustrated in fig. 2.7. In TXM the zone plate is used to focus the x-ray beam onto the sample where it then diffracts, the diffracted x-rays are the re-focussed by a second, smaller *micro zone plate* before being collected by a CCD which forms the final image. STXM utilises only a single zone plate which focusses the x-rays onto the sample where they diffract and are simply collected by an x-ray detector. The sample is raster scanned line-by-line through the focal point of the x-ray beam. Just like all x-ray based techniques TXM and STXM are able to obtain element specific measurements by tuning the energy of the x-rays to the necessary absorption edge. Conversely to XPEEM, both TXM and STXM are able to operate with an external magnetic field applied to the sample [76]. They can also be used in extreme temperature conditions and with biological samples [4, 77].

TXM is a useful tool for direct measurement of magnetic states in nanoscale magnetic elements, particularly in observing the vortex core and its dynamics

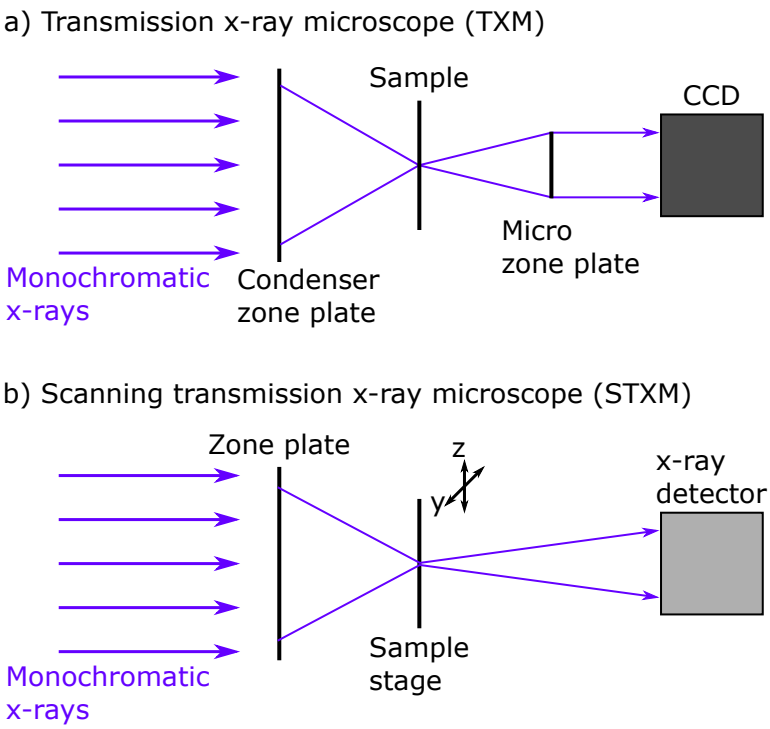

Figure 2.7: Schematic of two of the most popular x-ray transmission microscopy techniques which utilise Fresnel zone plates for focussing x-rays onto the sample, reproduced from [4]. a) shows the workings of a soft x-ray TXM. b) shows the configuration within an STXM where the sample is mounted on a movable scanning stage, allowing a line-by-line image to be produced.

due to the high spatial and temporal resolutions of the technique. In 2011 TXM was used to measure magnetic vortex core widths compared to the thickness of the elements they were in [78]. More recently, in 2018 the technique was used to further understand the processes behind magnetic bubble and skyrmion formation and elimination by application of electric current pulses [79].

STXM is illustrated in fig. 2.7b. The technique requires a spatially coherent soft x-ray source which is focussed onto the sample surface by a zone plate. Just like with TXM, the spatial resolution of STXM is related to the width of the outermost zones of the zone plate used to focus the x-rays. In order to form an image, the sample is scanned through the focal point of the focussed x-rays which are then transmitted through to a detector. Typical image acquisition times can be several minutes due to a large loss in x-ray photon flux intensity resulting from spatial filtering. This filtering is achieved by making the large central region of the zone plate opaque to x-rays by coating it with gold in order to provide a coherent x-ray beam. Fast scanning procedures can also result in a loss in spatial resolution due

to the slight nanometre inaccuracies of the sample position during scanning.

Since TXM uses x-rays from synchrotron sources, stroboscopic measurements can be carried out in order to obtain time-dependent imaging of dynamic magnetic processes. In 2004 time-resolved transmission x-ray microscopy (TR-TXM) was used for the first time to observe the magnetisation dynamics of vortex core precession within micron-sized square Py thin-film elements with a 32 nm and 100 ps spatial and temporal resolution respectively [80]. The technique has been used since then with increasing spatial and temporal resolutions [81, 82, 83].

The main advantage of TXM is its ability to achieve high spatial resolution images with short x-ray exposure times. Lateral resolution is determined by the outer fringe spacing of the micro zone plate and the wavelength of the light used to illuminate the sample, in acordance with the Rayleigh criterion as shown in [84]. Typically sub-10 nm resolutions are commonly achieved in magnetic imaging [53, 77]. Micro zone plates project a full-field image onto the CCD, with typical exposure times of one or a few seconds [74, 85] and field of view of $\sim$10-15 μm [86]. Spatial resolution is however limited by the quality of the Fresnel zone plate outer fringes.

2.3.6 Fourier Transform Holography (FTH)

FTH is a lensless imaging technique which relies on holography and has a number of advantages over the other techniques discussed so far. The principles behind holography obtaining real-space images will be discussed in greater detail below in section 2.4.

In 2004 x-ray FTH was first used to obtain magnetic images of Co/Pt multilayers in an in-line geometry by utilising the XMCD effect to obtain magnetic contrast [62, 87]. A spatial resolution of $\sim$50 nm was achieved, which at the time was comparable to STXM. The spatial resolution of FTH has since been improved upon by fabricating samples with smaller holographic reference points [15].

An image is formed by recording of a far-field diffraction pattern with a CCD. This diffraction pattern is formed by the constructive and destructive interference between x-rays which pass through the sample and through a near-by reference point. The imaging process is typical for an XMCD setup where the energy of x-rays used are tuned to the required L_3 edge of the magnetic material to be observed then recording two sets of diffraction patterns: one with left and one with right circularly polarised x-rays. The difference between these two diffraction patterns will recover the signal of the magnetic structure and is used to reconstruct the real-space image of the magnetic contrast within the sample. The reconstruction algorithm used to do this is a Fourier inversion, which can be applied directly since the phase information containing the magnetic contrast is encoded within the amplitude of this diffraction pattern.

FTH has been used to image many different magnetic samples, such as micron-scale magnetic elements [88], nanospheres [89] and multilayer structures that exhibit perpendicular magnetic anisotropy (PMA) [90, 91]. Imaging of in-plane magnetisation has also been achieved by milling a reference hole at an off-normal angle to the sample surface and imaging with the sample at this angle to the x-ray beam [88]. Attempts have also been made to increase the field-of-view, typically $<2\,\mu$m as dictated by the coherence length of the x-ray beam, by separating the object and reference point from the magnetic sample [90]. This allows moving of the object/reference relative to the magnetic sample, enabling the ability to take snapshots of the sample at different positions and combine the resulting images into a single, contiguous image.

Tabletop FTH has also been demonstrated and achieved a spatial resolution of 53 nm [92]. However, due to the lack of a tabletop method to polarise the x-rays this was not able to take advantage of the XMCD effect to obtain magnetic contrast and thus can not be used to great effect on magnetic samples.

Advantages of FTH include that its lensless nature is not subjected to lens aberrations affecting the achieved spatial resolution. It can take advantage of

using x-rays as the probe, theoretically resulting in high spatial resolutions on the order of several nm, imaging with element specificity, utilisation of stroboscopic measurements in order to obtain high temporal resolutions of up to 70 ps and the ability to observe in-plane or out-of-plane magnetism.

The limitations of the technique however include a lower spatial resolution than those achieved with TXM, STXM and PEEM since this resolution is related to the size of the holographic reference point, usually $\sim$50 nm. The field of view is also relatively small at only a few microns due to the necessity to block all x-rays with an absorbing mask, allowing x-rays to only pass through the object and reference, both of which are milled into the mask with FIB. This also makes sample preparation quite complex and time consuming.

HERALDO

HERALDO is an extension of the FTH technique that improves upon it by utilising extended geometries such as slits, instead of cylindrical points, as the holographic reference. Extended references have an advantage when imaging magnetic samples since they allow rotation of the sample with respect to the x-ray beam, providing a method for the imaging of in-plane as well as out-of-plane magnetisation. Additionally, because the extended reference allows a greater flux of x-rays through compared to a point reference, there is an effective decoupling of the spatial resolution from the reference signal strength by ensuring that the transmitted signal is above the noise level for the experiment. The increased x-ray flux also reduces image acquisition time which is particularly useful in single-shot imaging where there is a limited number of photons. The HERALDO technique also benefits from the relative ease of fabrication of high-quality extended references compared to the cylindrical references used in FTH. Extended references of as low as 10 nm wide are able to be made whilst reference holes tend to be no smaller than $\sim$50 nm.

A detailed overview of the HERALDO process will be given in section 3.2.

Property	MOKE	MFM	XPEEM	TXM	FTH
Spatial Resolution (nm)	200-400	∼10	∼50	∼5	∼20-50
Temporal Resolution	100 fs	n/a	70 ps	70 ps	70 ps
Sample Fabrication	Simple	Simple	Simple	Complex	Complex
Contrast	OOP	OOP	IP	IP/OOP	IP*/OOP
Pen. Depth	Surface	Surface	Surface	Bulk	Bulk
External Fields	√	×	×	√	√

Table 2.1: Comparison between all techniques discussed above. IP: in-plane, OOP: out-of-plane. *IP only for FTH with cylindrical references milled at an angle and HERALDO. Regarding sample fabrication, 'simple' refers to the sample not needing to be optically transparent as they do not rely on the transmission of a signal through the sample, whereas a 'complex' sample must be very thin (a few 100's nm) in order to allow transmission of an optical-based probe. Such thin samples require multiple processing steps, mostly on the top side but sometimes also on the underside, as well as them being exceedingly fragile and easily damaged.

2.3.7 Summary of Imaging Techniques

MFM Summary

The advantages of this technique are:

- High spatial resolutions on the order of 10 nm.
- Simple requirements for sample imaging (for example it does not need to be transparent to particular wavelengths of light).

However there are several key limitations:

- The inability to detect in-plane magnetic moments or those within the bulk of the sample.
- External magnetic fields cannot be applied to the sample without degrading the final image.
- Unable to obtain time-resolved measurements of dynamic processes due to the long scan time.

XPEEM Summary

Overall, XPEEM has many benefits compared to the previously discussed techniques, particularly:

- Fast image acquisition time.
- Wide range of zoom levels.
- Can achieve high spatial resolutions on the order of $\sim$20 nm, compared to optical techniques (100's nm).
- Can achieve very high temporal resolutions of $\sim$70 ps.
- Simple sample fabrication due to it not needing to be transparent to x-rays, unlike with x-ray transmission techniques.

However there are some limitations:

- Can not apply high magnetic fields near the sample.
- Limitations of the spatial resolution resulting from the inherent spherical and chromatic aberrations within the objective lens, though there are aims to reduce these aberrations.

TXM/STXM/TR-TXM Summary

Transmission x-ray microscopy techniques maintain some notable advantages over other techniques discussed thus far, such as:

- Relatively quick and simple compared to other techniques.
- Can apply external magnetic fields to the sample to observe field-dependent effects.
- High spatial resolutions (sub-10 nm) can be achieved.

- Element specificity by exploiting the XMCD effect with the x-rays.
- Layers buried within a multi-layer stack can be imaged.
- Measurements within extreme environments, such as low temperatures, and of biological samples can be made.
- Time-resolved imaging of up to 70 ps can be performed by utilising stroboscopic methods based on the synchrotron x-ray burst time profile.

However, the drawbacks are:

- Resolution is limited by diffraction optics, specifically the width of the outer edges of Fresnel zone plates.
- Samples and substrate must be transparent to soft x-rays to allow their transmission.

Holography Summary

Overall, holography has many advantages, such as:

- The spatial resolution is no longer limited by lens aberrations.
- High (sub-30 nm) spatial resolutions typically achieved.
- Element specific imaging with x-ray energy tuning.
- Can take advantage of the XMCD effect to obtain magnetic contrast.
- Buried layers within a multi-layer system can be imaged.
- Imaging can be performed with external magnetic fields applied to the sample
- Samples can be measured in extreme environments, such as low temperatures.

- Stroboscopic measurements can be performed to obtain time-resolution of dynamic processes.
- The reconstruction algorithm is a simple Fourier transform and is able to recover the real-space image from the diffraction pattern without any extra phase-retrieval steps necessary.

However the drawbacks are:

- Coherent source of illumination is required.
- Field of view is limited by the coherence of the illumination.
- Sample must be transparent to x-rays.
- Integrated object and reference regions must be fabricated for each sample.
- Spatial resolution is limited by the size of the holographic reference.

2.3.8 Comparison of Magnetic Imaging Techniques

This section will discuss the relative advantages and limitations of the techniques outlined above with the scope focussed specifically on observing magnetic domains. One of the most important factors to consider when imaging magnetic structures is whether or not a technique is capable of achieving a spatial resolution that is sufficiently high for measuring the structures or processes that are intended to be observed. Since magnetic structures are typically no smaller than the magnetic exchange length of $\sim$5 nm this sets a minimum required spatial resolution on the order of a few nanometres. Since all of the x-ray-based techniques listed above are, in theory, able to achieve this, it generally leaves the choice of technique up to other factors.

Another important consideration is the physical structure of the sample and substrate. For example, magnetic hard disk read heads are typically fabricated

on a thick silicon substrate which is not transparent to x-rays, therefore implying that non transmission-based imaging techniques, such as XPEEM and TRSKM [48], are suitable for observing these samples whilst TXM and other transmission-based techniques are not suitable. Conversely if the magnetic configuration within the bulk of a multi-layer thin-film system is to be measured then a transmission-based technique with element sensitivity is required in order to observe the buried layer within the multi-layer stack. Techniques such as TR-MOKE or XPEEM are only capable of observing the top surface layer of a sample since they measure either a reflected signal or surface photoemitted electrons respectively.

Whilst understanding magnetic domain structure is important, measuring the dynamic magnetic processes that occur within these structures is also crucial and has only received significant interest in the past decade due to advances in stroboscopic x-ray measurements. Techniques involving x-rays from synchrotron sources, such as XPEEM, TXM, STXM, FTH and HERALDO are able to achieve a theoretical temporal resolution down to $\sim$70 ps since this is the combined x-ray pulse width and electronic jitter commonly observed at such facilities. This is often more than suitable for observing most dynamic magnetic processes, however it is not sufficient for ultra-fast processes that occur within the GHz-regime, such as the mechanisms that govern the electron, spin and lattice subsystems involved in domain reorientation [51, 93]. Techniques that utilise pulsed lasers however, such as TR-MOKE and TRSKM, are able to achieve higher temporal resolutions on the order of 100's fs and are often used to observe ultra-fast magnetisation dynamics [48, 49, 50].

The ability to apply an external magnetic field to a sample whilst imaging allows field-dependent measurements to be made. An example of this is with nano-contact spin-torque oscillator (NC-STO)'s that require a magnetic field to be applied to the sample in order to nucleate a magnetic droplet at the position of a nanocontact that applies a spin-polarised current to the sample [94]. These devices are of particular interest for their potential use as microwave oscillator devices. Therefore in order to study NC-STO's the imaging technique must be

able to obtain images with magnetic contrast whilst an external magnetic field is applied, such as TXM, STXM, FTH and HERALDO.

Out of all of the techniques discussed so far MFM is arguably the most limited in its capabilities. Although it is able to obtain images with a high spatial resolution that can clearly define a magnetic vortex core, it is incapable of time-resolved measurements due to the long time required to scan the sample and obtain an image. This makes observations of dynamic processes with MFM impossible. In-plane magnetic moments are also unable to be detected thus making measurements of more complex samples limited in what information can be discerned about the internal structure. Additionally because the tip used to detect the stray magnetic field of the sample surface is in itself magnetic, external magnetic fields cannot be applied to the sample as this will directly affect the tip and thus the final image will become distorted.

X-ray FTH has several advantages over TXM techniques that utilise Fresnel zone plates. Since FTH, and by extension HERALDO, do not require x-ray optics in order to retrieve the all important phase information from the diffracted x-ray beam, these techniques do not suffer from the aberrations that affect optical lenses which ultimately reduce the spatial resolution of the final image. Instead the spatial resolution is limited by the size and quality of the reference.

Holographic imaging requires additional sample preparation compared with regular TXM techniques however. A holographic mask is required to be deposited onto the underside of the sample in order to absorb x-rays and limit x-ray transmission only to the object and reference holes. The process is relatively straight forward however and can be automated in order to batch process multiple samples [95].

A second advantage of TXM techniques compared to FTH is that the XMCD signal used for magnetic contrast can be applied at off-normal angles to the sample surface. FTH on the other hand can only gain magnetic contrast by having the reference hole lie parallel along the propagation path of the x-ray beam in or-

der to allow x-rays to pass through it and interfere with the signal from the object to form the diffraction pattern. This is because the XMCD signal used for magnetic contrast scales with the dot product of the of the incident x-ray wave vector with the magnetisation vector. HERALDO however is able to bypass this limitation of FTH since samples with an extended reference can be rotated such that x-rays are still capable of passing through the reference, however there is now some parallel component of the in-plane magnetisation vectors with the x-ray wave vector, allowing measurement of the samples in-plane magnetic contrast. FTH samples may have the reference hole milled at the required angle however these are somewhat difficult to mill with a small enough size to reach spatial resolutions comparable to TXM techniques and also can only be used to image at that specific angle.

2.4 Principles of Holography

Since holography is a lensless technique that relies upon the interference of an object wave with a reference wave, the technique is highly dependent upon the coherence of the initial wave that diffracts through the sample. If the illumination source created an incoherent wave then the phase between the object and reference waves may not be consistent with each other, thus making it impossible to differentiate the original phase from the recorded phase. This would result in the inability of the technique to retrieve the phase information.

In the following section we will discuss the properties that affect the coherence of a wave along with a brief explanation of the Fourier transform steps required to convert a reciprocal-space diffraction pattern into a real-space image containing magnetic contrast [96]. This will then be discussed in relation to the HERALDO technique.

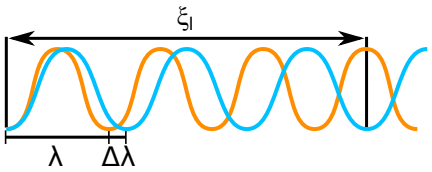

Figure 2.8: Longitudinal coherence of a wave.

2.4.1 Coherence

When defining the coherence of a wave there are two types to consider: temporal (longitudinal) coherence and spatial (transverse) coherence. The temporal coherence defines the time for which a wave will propagate with longitudinal coherence. For holographic experiments, this must be at least equal to the total difference in path length between the interfering beams. Spatial coherence describes the relationship between the phase of two points that lie along a single wavefront. Non-laser sources generally have very poor spatial coherence, therefore measures need to taken in order to filter the beam to improve this coherence.

Longitudinal Coherence

Longitudinal coherence, ξ_l, is defined as the distance over which two waves with the same initial source point with slightly different wavelengths become out-of-phase by π. This is shown in fig. 2.8. This value is related entirely to the monochromaticity of the wave, typically defined in terms of wavelength, frequency or photon energy.

$$\xi_l = \frac{\lambda^2}{2\Delta\lambda} = \lambda\frac{\upsilon}{\Delta\upsilon} = \lambda\frac{E}{\Delta E}. \tag{2.21}$$

Transverse Coherence

Transverse coherence, ξ_t, is defined as the lateral distance along a single wavefront over which there is a complete dephasing by π of two waves of the same wavelength which originated from two separate source points in space. Fig-

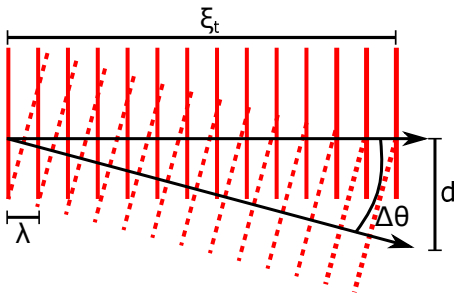

Figure 2.9: Transverse coherence of a wave. Solid and dotted red lines represent wavelength maxima nodes along each of the two waves which have the same wavelength and travel at an angle, θ, to each other. Note how the transverse coherence is measured from a point where the two waves appear to originate from the same source and is measured to where the two waves are π rads $(180°)$ out of phase.

ure 2.9 shows a visual representation of this, including the definitions of where the parameters θ, λ and ξ_t originate from for the equation:

$$\xi_t = d \cdot \theta = \frac{\lambda}{2\pi}. \tag{2.22}$$

2.4.2 Fourier Analysis

Fourier transforms are very powerful and are commonly applied to functions that are periodic in time, such as with a swinging pendulum exhibiting simple harmonic motion. In this section however we will focus on the Fourier transform applied in the spatial and time domain. A seemingly complicated spatial periodicity seen in diffraction patterns can in fact be simplified and described by a set of discrete spatial frequencies. The one-dimensional Fourier transform is defined as,

$$\mathcal{F}[f(x)] = F(u) = \int_{-\infty}^{\infty} f(x) exp^{-i2\pi ux} dx, \tag{2.23}$$

where $f(x)$ is a real-space complex function, such as that from a signal, and $F(u)$ is its Fourier transform, used to give the spectral response of this signal [97]. Here u represents the reciprocal-space coordinate and $\mathcal{F}$ represents the Fourier transform operator. The terms $f(x)$ and $F(u)$ are known as reciprocal

pairs and by introducing a second spatial dimension to their relationship makes them relevant for image processing and thus forms the basis behind FTH and HERALDO.

We can find the *spectrum power density*, also known as the *intensity distribution*, by taking the square modulus of the Fourier transform, $\mathcal{F}|f(x)|^2$. If a Fourier transform is taken of this power spectrum we can find the autocorrelation of $f(x)$ (i.e. $\mathcal{F}\{|f(u)|^2\} = (f * f)(x)$, as shown from the convolution theorem. This is analogous to coherent light being transmitted through an aperture which we experienced with the samples used throughout the experimental work presented in this thesis.

Shift Theorem

The shift theorem relates to the Dirac delta function and states that the Fourier transform of a delta-function is unity, $\delta(x) \leftrightarrow 1$. The Fourier transform of a Gaussian of unit area that becomes narrower and higher is another Gaussian that becomes broader until the limit where it becomes a straight line at unit height above the axis. Whilst the delta function has infinite height it is often encountered as being multiplied by a constant, $a\delta(x)$ where a represents the height of the delta function. This has the following properties of:

$$\delta(x-a) = 0 \quad unless\ x = a, \tag{2.24}$$

and the "shift theorem":

$$\int_{-\infty}^{\infty} \delta(x-a)f(x)dx = f(a), \tag{2.25}$$

where $\delta(x-a)$ is a delta function located at $x = a$. The product under the integral is zero except at the point $x = a$ where the integration of the delta function has an amplitude of $f(a)$ [97]. This can be expressed in two dimensions like so:

$$\int\int \delta(x-a, y-b) f(x,y) dxdy = f(a,b), \tag{2.26}$$

where $\delta(x-a, y-b)$ is the delta function at position a and b. This is a core property of convolution which is used extensively in digital image processing.

Returning to a one dimensional system, if $f(x)$ has the Fourier transform of $F(u)$, then the function $f(x-a)$ has the Fourier transform of $exp^{-i2\pi au}$. The significance is that if a given function becomes shifted by a positive amount in a then no change in the amplitude of the Fourier component will occur, instead there will be a change in the phase of the Fourier transform. We can write this as,

$$\mathcal{F}\{\delta(x-a)\} = exp^{-i2\pi au}, \tag{2.27}$$

and therefore the Fourier transform of a delta function that is shifted is given by a phase shift, $exp^{-i2\pi au}$.

Convolution Theorem

An important concept in Fourier theory is the convolution theorem. Convolution is essentially the integral over infinite space of one function at position u multiplied by a second function at position $x-u$. If we take the two functions, $f(x)$ and $g(x)$, as arbitrary Fourier transforms like so,

$$f(x) = \mathcal{F}[F(u)] = \int_{-\infty}^{\infty} F(u) e^{-2\pi iux} du, \tag{2.28}$$

$$g(x) = \mathcal{F}[G(u)] = \int_{-\infty}^{\infty} G(u) e^{-2\pi iux} du, \tag{2.29}$$

then the convolution theorem states that between these two functions, $f(x)$ and $g(x)$, their convolution is defined as a new function, $h(u)$, where,

$$h(u) = f(x) * g(x) = \int_{-\infty}^{\infty} f(u)g(x-u)du. \tag{2.30}$$

This operation can be considered as the area of the overlap between function $f(x)$ and a spatially inverted version of function $g(x)$. The convolution theorem relates the convolution between the real space domain to the Fourier domain via a multiplication which, like with the Fourier transform, can be extended to two dimensions like so:

$$h(x,y) = f(x,y) * g(x,y) = \int\int f(a,b)g(x-a,y-b)dadb, \tag{2.31}$$

of which the result in the Fourier domain is:

$$H(u,v) = F(u,v)G(u,v). \tag{2.32}$$

Ultimately, the most important implication of the convolution theory is that a multiplication in real space results in a convolution in Fourier space and vice versa.

Derivative of a Convolution

The derivative of the convolution of two functions, $h(x,y)$ and $g(x,y)$ is equal to the convolution of either function with the derivative of the other,

$$[h \otimes g(x,y)]' = h \otimes g'(x,y) = h' \otimes g(x,y). \tag{2.33}$$

The significance of this is that during HERALDO imaging, if we modify the resultant hologram such that the resulting cross-correlation of the object forms with a derivative of the reference, an extended slit, it will behave as two Dirac delta functions instead, one at each end of the extended slit.

Cross-Correlation

The cross-correlation of two functions $f(x)$ and $g(x)$ is equivalent to the convolution of $f^*(-x)$ and $g(x)$, where $f^*(-x)$ is the complex conjugate of $f(x)$. We can therefore define the cross-correlation between two functions, f and g, as:

$$c(x) = (f * g)(x) = \int_{-\infty}^{\infty} f(s)g^*(s-x)ds, \tag{2.34}$$

where g^* is the complex conjugate of the function $g(x)$. This is similar to a convolution except the second function is not spatially reversed and the shift direction is changed. If we consider $f(x)$ to be the signal and $g(x)$ to be the reference, correlation between the two gives a peak where the signal "matches" the reference. In two dimensions the cross-correlation can be expressed like so:

$$c(x,y) = (f * g)(x,y) = \int\int f(s,t)g^*(s-x,t-y)dsdt. \tag{2.35}$$

This is used in digital imaging to measure the "similarity" between two functions.

Fourier Transforms and Holography

By following the principles outlined above we are able to obtain an expression for the derivative of a cross-correlation between a holographic reference, $r(x)$, and an object, $o(x,y)$,

$$[r(x) \otimes o^*(x,y)]' = r \otimes o'^*(x,y) = r' \otimes o^*(x,y). \tag{2.36}$$

The Fourier transform of eq. (2.36) will result in:

$$2\pi iu[R(u)O^*(u,v) = -R(u)[2\pi iuR(u)]O^*(u,v), \tag{2.37}$$

where $R(u)$ and $O(u,v)$ are the respective Fourier transforms of $r(x)$ and $o(x,y)$ respectively.

2.4.3 HERALDO

Here we will discuss how the above concepts apply to the HERALDO imaging technique. The convolution theory is important since we have two functions: one from the object, $o(x,y)$, and one from the reference, $r(x,y)$, which interfere with each other to form a third function, $h(x,y)$. The third function is a convolution of the original two functions and forms the diffraction pattern (hologram) captured by the CCD. The shift theorem dictates that, by having the reference physically offset by some distance from the object origin, there is a phase shift between the two functions present in the third function. However, since a CCD cannot record negative values and consequently is not able to record a phase shift, instead what results is in fact a recording of the power spectral density, i.e. the squared modulus, of the autocorrelation of the two functions as the captured hologram. According to the Wiener-Khinchin theorem this autocorrelation is mathematically equal to a the Fourier transform of the power spectral density of the original functions.

Therefore the aforementioned phase shift can be recovered by deconvoluting the two original functions in our hologram, resulting in the retrieval of the magnetic information. This deconvolution can only be performed if one of the two functions is known by applying its directional derivative to the hologram. Since the reference function is known (HERALDO utilises a slit-shaped reference which creates a top-hat function) the directional derivative can be applied along the reference function of the hologram in order to transform the reference into a delta function, or in the case of a reference slit, a pair of delta functions. A Fourier transform can then be applied to the hologram which translates the data from Fourier space into real space, revealing the magnetic information of the sample at the position in the hologram where the reference and object functions cross-correlated. This

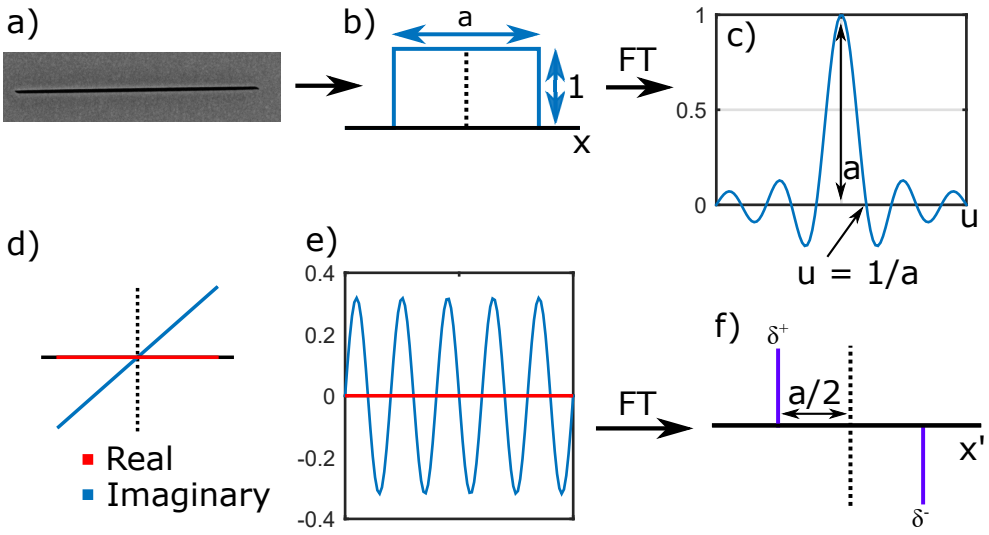

Figure 2.10: a) SEM image of an extended reference slit. b) Numerical simulation of an intensity profile of coherent light passing through the slit. c) Fourier transform of the intensity profile in b), displaying the sinc function. d) a complex-valued ramp function generated from $i2\pi uR(u)$ that is multiplied to b). e) the Fourier space mulriplication of b) and d), displaying the real space derivative of the slit. f) Fourier transform of e), representing the Dirac delta functions formed after the directional derivative of the slit is calculated. The delta functions are of opposite polarity to each other based on the derivative of the step function.

position is offset from the origin by a distance relative to the physical offset of the reference from the object.

FTH utilises a cylindrical reference which naturally produces a Dirac delta function, which in reality is a Gaussian with width relative to the cylinder diameter. Because of this FTH does not require a directional derivative. Conversely HERALDO uses an extended reference which produces a top-hat function, see fig. 2.10b. If we apply a directional derivative across this function, fig. 2.10d, two Dirac delta points of opposite polarity are formed, fig. 2.10f. These delta functions are also, in reality, Gaussian with width relative to the width of the extended reference.

This is a key step for the HERALDO technique since this allows the hologram to benefit from the increased x-ray flux of the extended slit and allow sample rotation to image in-plane magnetism whilst retaining the ability to cross-correlate a delta function with the object wave. Additionally since the extended reference acts like two individual cylindrical references, two images of the object and refer-

ence cross-correlation are formed within the reconstruction: one from each end of the slit.

If we assume that for a chosen reference, $r(x, y)$, there exists a linear differential operator, $\mathcal{L}^n\cdot$. When the operator is applied onto the reference we receive a Dirac delta function located at (x_0, y_0) plus an additional arbitrary function, $g(x, y)$ [96]. We can express this like so:

$$\mathcal{L}^n\{r(x,y)\} = \sum_j = A_j\delta(x - x_0, y - y_0) + g(x, y), \tag{2.38}$$

where A_j is an arbitrary complex-valued constant. The additional function $g(x, y)$ is simply the second Dirac delta function separated from (x_0, y_0) by a distance equal to the length of the extended reference. If we apply the linear differential operator to the field autocorrelation, we obtain:

$$\mathcal{L}^n\{f \otimes f\} = \mathcal{L}^n\{o \otimes o\} + \mathcal{L}^n\{r \otimes r\} + (-1)^n[o \otimes \mathcal{L}^n\{r\}] + [\mathcal{L}^n\{r\} \otimes o]. \tag{2.39}$$

Using the shifting property of the Dirac delta we get:

$$\begin{aligned}\mathcal{L}^n\{f \otimes f\} = \mathcal{L}^n\{o \otimes o\} + \mathcal{L}^n\{r \otimes r\} + (-1)^n o \otimes r + r \otimes o \\ + (-1)^n A^* o(x + x_0, y + y_0) + Ao^*(x_0 - x, y_0 - y).\end{aligned} \tag{2.40}$$

The last two terms are what enable the direct recovery of the original object field, so long as the reconstruction does not overlap with the cross-correlation terms. As with conventional FTH that utilises cylindrical references, the reconstruction produces a translated image of the object, $o(x + x_0, y + y_0)$, as well as its complex conjugate, $o^*(x_0 - x, y_0 - y)$, which is inverted through the origin.

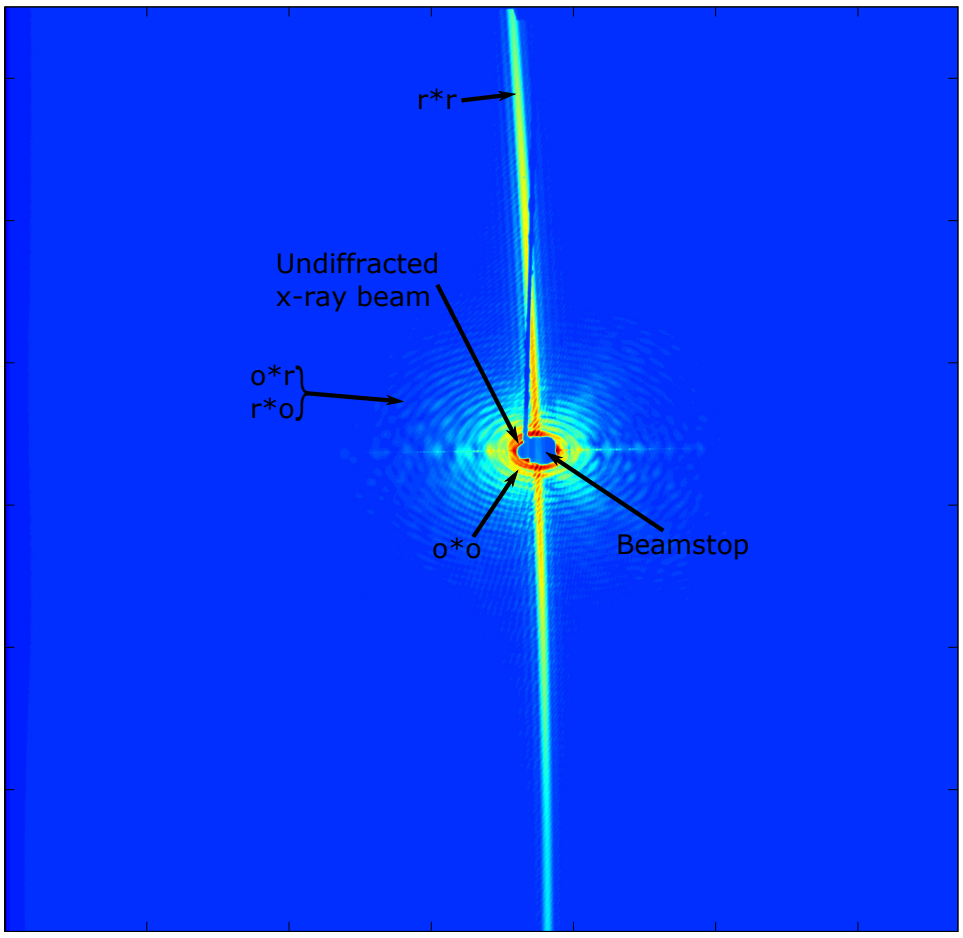

Figure 2.11: Diffraction pattern captured by the CCD with the HERALDO technique. The bright vertical line and concentric rings in the centre are created by the autocorrelation of the reference slit (r*r) and the aperture (o*o) respectfully. The rest of the pattern contains the data formed by the cross-correlation of the reference and the aperture. The beamstop blocks the central undiffracted x-ray beam, creating a low-intensity (blue) region. Without the beamstop the CCD would be damaged by the undiffracted beam.

An example of a diffraction pattern obtained with HERALDO is displayed in fig. 2.11 which shows the autocorrelation of the object (aperture), $o * o$, autocorrelation of the extended reference, $r * r$, and the cross-correlated data, $o * r$ and $r * o$, in the region surrounding the origin. The autocorrelations extend from the origin of the hologram, where the reference autocorrelation determines the position for application of the directional derivative filter. Once this filter is applied correctly, we can apply an inverse Fourier transform to the hologram in order to switch from the time domain to the spatial domain, reconstructing the structural (sum) and magnetic (difference) data of the observed sample. An example of a reconstructed HERALDO image is shown in fig. 2.12.

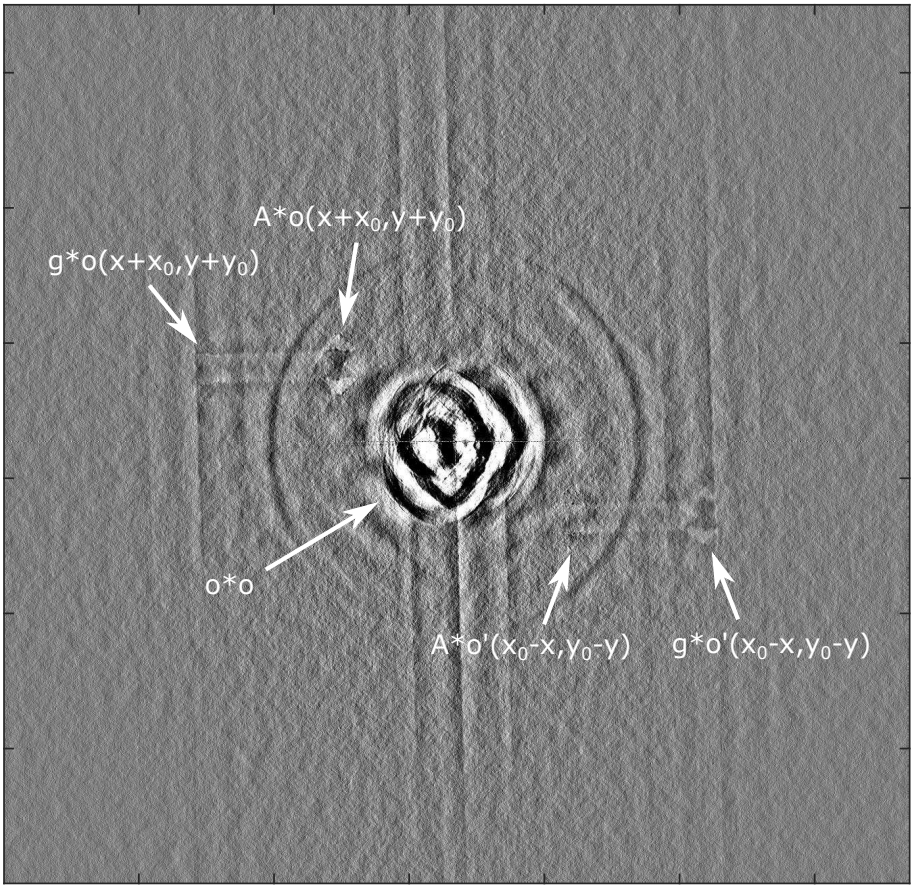

Figure 2.12: Example of a reconstructed image. Object autocorrelation, $o * o$, is visible at the origin, whilst the cross-correlation between the object and reference, $A * o$, and its complex conjugate, $A' * o$, are visible at positions relative to the displacement of the reference slit from the object.

2.5 Summary

The background theory for relevant ferromagnetic concepts have now been covered along with a critical review of popular imaging techniques used today for observing magnetic dynamics on the nanoscale and also a brief explanation of the principles behind holographic imaging with FTH and HERALDO. We concluded that whilst FTH does not suffer from lens aberrations, it still suffers from other drawbacks which limit its flexibility and versatility for magnetic imaging. However HERALDO and its extended references which allow imaging of in-plane magnetic moments is able to overcome many of these limitations. Additionally the increased x-ray photon flux through the reference results in reduced image acquisition times and improves spatial resolution due to the sharper features of extended references compared to reference holes.

Chapter 3

Experimental Methodology

The focus for this chapter will be on the various practical aspects for each experiment, such as the fabrication processes for the different samples used in the experiments conducted at the four synchrotron beamlines, the noting of any differences in experimental procedure between the beamlines themselves and also the practicality of the HERALDO process itself and comparing it to other available techniques.

For clarity within this thesis the term *"chip"* refers to the entire square silicon substrate that contains four square silicon nitride membranes. The chip is 5 mm x 5 mm x 500 μm in size. The term *"sample"* refers to a specific silicon nitride membrane within the silicon chip substrate along with its integrated CPW. Each sample's CPW may have different dimensions compared to others on the same chip whilst some chips contain samples with the same CPW's but which support different element configurations. The term *"element"* refers to a single Py structure (square or otherwise) that is either in a large array or a strip of such elements that run along the length of the central CPW signal line. The term *"device"* refers to a single element which has had a reference slit and aperture milled via FIB such that it can be observed experimentally. A single sample may contain anywhere from three to nine devices along its entire CPW length but always has many more elements than this which are not able to be observed due to them lacking

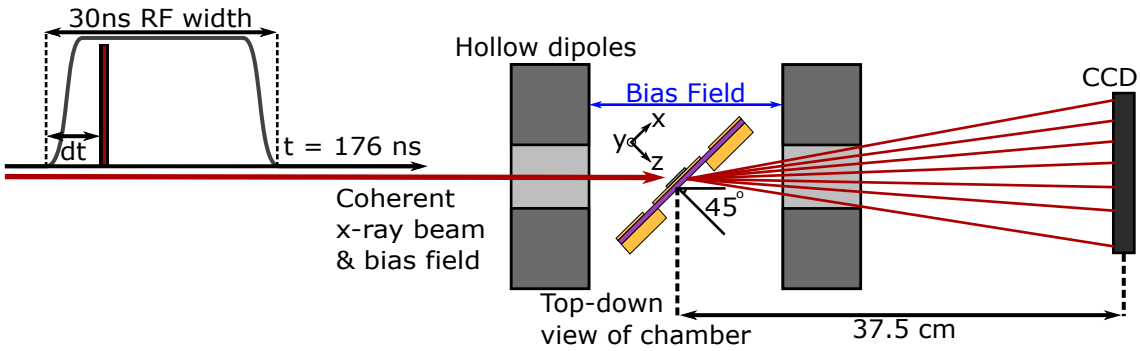

Figure 3.1: Typical setup of the sample chamber for experiments carried out at the ID32 beamline at the ESRF. This setup is the same for all experiments, the only significant alteration is the magnet system. A time-profile is displayed on the left for performing stroboscopic pump-probe measurements in order to obtain time-resolved imaging of magnetic dynamics.

apertures and references. The devices are separated by the average x-ray beam diameter of 50 μm to prevent the x-ray beam from illuminating multiple samples during an experiment.

3.1 Synchrotron Beamlines

The experiments outlined in this thesis were carried out by utilising the HERALDO technique and performed at one of four synchrotron beamlines: I06 and I10 at Diamond Light Source (DLS), Oxfordshire, United Kingdom, ID32 at the ESRF, Grenoble, France and SEXTANTS at SOLEIL synchrotron, Saint-Aubin, France. Figure 3.1 depicts a typical setup for performing stroboscopic pump-probe measurements of magnetic dynamics with time-resolution. The magnet system varied based on synchrotron beamline, as did the time between successive x-ray probe pulses.

The ID32 beamline at the ESRF had a pair of electromagnetic coils situated along the path of the x-ray beam, however their placement was fixed thus allowing application of the magnetic field parallel to the path of the x-ray beam. Therefore if the sample surface normal was at a 45° angle to the x-ray beam for equal imaging of in-plane and out-of-plane magnetic moments then the bias field would be applied at this angle. Whilst this reduced the flexibility of bias field application

angles during imaging, we were able to overcome this limitation by carrying out the field-dependent processes before imaging and removing the bias field before taking measurements at the desired angle.

The SEXTANTS beamline at SOLEIL was upgraded with a quadrupole permanent magnet system mounted to a movable stage which allowed application of a bias field in a 360° angle around the sample. The magnetic field could not be removed entirely however which affected the measurements of some results, mainly those outlined in chapter 5, though the system was not in place for results presented in chapter 4 which is why there is no mention of the issue for those measurements.

I06 and I10 at DLS utilised the portable octopole magnet system (POMS) electromagnet system owned by Prof. G. Van der Laan. This was an octopole system that was mounted around the sample chamber. The maximum field that could be achieved was 0.7 T and could be applied in any direction by changing the theta and azimuthal polar angles.

When collecting data on a beamline there were several aspects that had to be optimised in order to ensure high-quality data was collected in a time-efficient manner yet still working within safe limits of the CCD to prevent the x-rays from saturating and damaging the pixels. First was ensuring the beamstop blocked the intense, undiffracted portion of the x-ray beam to prevent damage to the CCD. In most cases the CCD and beamstop were already correctly positioned however in some cases it was necessary to fine-tune its position.

Next, an x-ray intensity scan was performed to find the correct device on the chip. This was performed either by using a series of x and y line scans, as shown in fig. 3.2a or by forming a coloured two-dimensional intensity map that of a defined rectangular region, shown in fig. 3.2b. The first method was faster whilst the second method was useful for more complex samples where the devices were more difficult to locate.

Once the correct device was positioned within the x-ray beam the next step

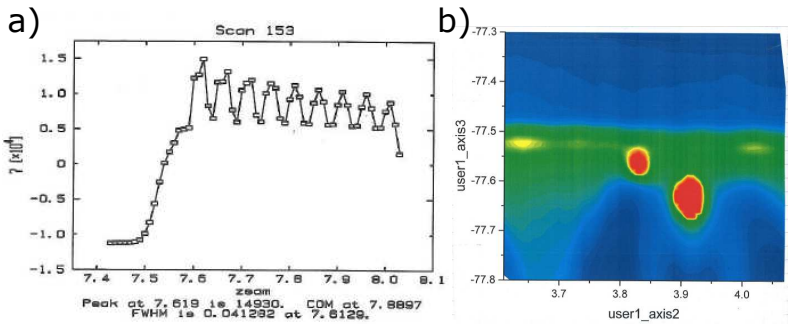

Figure 3.2: Examples of a) a line scan and b) a 2-dimensional intensity map scan that were used to identify the positions of devices within a sample during an experiment. In a) the x-axis represents the position of the motor whilst the y-axis represents x-ray beam intensity. This data was taken at the ESRF and shows a vertical scan along the length of the CPW of a sample containing nine devices, shown by the peaks. b) is an intensity map with the x and y axes representing motor positions whilst the colour at each coordinate represents the relative x-ray intensity on the diode with blue being low photon counts and red being high counts. The sample is clearly visible with the larger red region between the blue forks representing the aperture and reference slit whilst the smaller red region amidst the green space is a 1 μm diameter hole that was used for locating devices during FIB milling.

was to set the monochromator to the required x-ray energy. The majority of experiments presented in this thesis were performed at the Fe L_3 edge of $\sim$707 eV since the magnetic material investigated, Py, consisted of $Ni_{0.8}Fe_{0.2}$ [98]. This can be seen in fig. 3.3. Initially this energy was chosen for imaging in order to test the limitations of the HERALDO technique since there is a reduced signal originating from the Fe atoms compared to Ni, however we found this energy more than suitable for further experiments.

The next step was reducing the beam diameter to $\sim$50 μm by altering the upstream exit slit positions in order to improve the x-ray beam coherency, increasing domain contrast. We did not go below a 50 μm diameter in order to reduce the sensitivity of image quality to x-ray beam drift. A smaller diameter will lead to a quicker reduction in image quality if the beam would drift away from the device.

The penultimate stage involved taking some initial images of the sample and identifying potential areas that can be further optimised. For example stray light entering from outside the chamber negatively impacted on the diffraction pattern quality, thus all areas of potential light ingress must be covered with aluminium

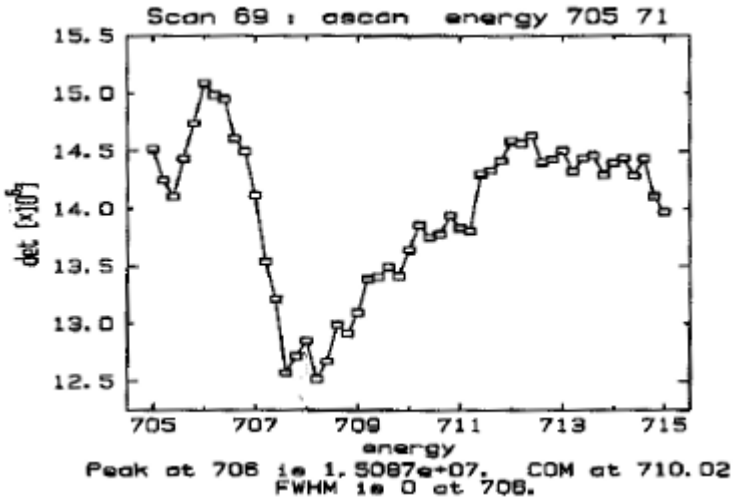

Figure 3.3: Example of an XMCD energy scan showing a dip around 708 eV. This corresponds to the Fe L_3 x-ray absorption edge of 707 eV. The difference between these values is likely due to miscalibration.

foil in order to minimise this. In some instances there was also stray x-ray beam diffraction originating from the sample itself due to the mounting of the chip leaving gaps for x-rays to pass through. These gaps had to be covered with thin strips of aluminium in order to block the x-rays from causing unwanted noise on the CCD. Once all of these steps were completed the sample was ready for measurement. Figure 3.4 shows the typical process used to obtain images of the magnetic structure within a sample for all beamlines used.

3.2 Delay synchronisation of magnetic pulse with x-ray pulse

All measurements taken and presented throughout this thesis were produced by *pulsed pump-probe stroboscopic* methods in order to obtain time-resolution of magnetisation dynamics. The term stroboscopic refers to the method of synchronising a *pump pulse* with a *probe pulse* by ensuring that the probe pulse images the sample at the same point within the excitation cycle created by the pump pulse for every cycle. The pump pulse was an electronic signal sent from an *Agilent 81150A + 81112A signal generator* to the sample CPW which produced a

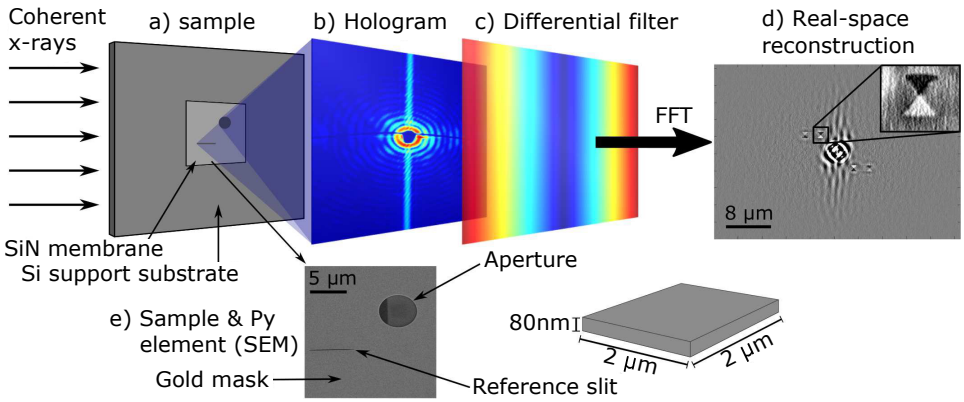

Figure 3.4: Schematic of the HERALDO process and sample structure. a) The sample on a SiN membrane. The incident polarised coherent x-rays diffract at the aperture hole and the reference slit to create an interference pattern b) between these two beams which yields a hologram that is recorded on a CCD camera. c) The intensity map of the differential filter, applied along the directional derivative of the x-rays from the reference slit. d) The reconstructed image after FFT and polarisation analysis. Inset shows a close-up of the aperture with the magnetic contrast of the Py element. e) (SEM) image from the back side of the sample showing the aperture in the 600 nm gold layer together with the reference slit. The CPW with the square Py element can be seen in the aperture through the 200 nm SiN membrane on the front of the sample. Dimensions of the Py element are shown.

magnetic field in order to excite magnetic dynamics (vortex precession) within the sample. The probe was the x-ray pulses produced by the electron bunches within the synchrotron storage ring. A pulsed stroboscopic regime was used for its simplicity over the continuous regime for samples where the resonant frequency is not known or complex. The drawback to the pulsed regime is that some time is needed at the start of an experiment in order to find the point in time where the pump and probe pulses are simultaneously incident upon the sample, called t_0 throughout this thesis.

The first step of obtaining stroboscopic time-resolved imaging was to find t_0. A series of initial measurements of the sample were obtained starting with a magnetic pump pulse width equal to half the time period between successive x-ray probe pulses. If the vortex core was observed to be displaced from its rest position then the x-ray pulse was determined to be within this region of the master clock trigger signal. This process was repeated and the magnetic pulse width was reduced by half each time the vortex was observed to be displaced in order

to narrow down exactly where t_0 lay.

Different beamlines had different master clock times since this value is affected by the size of the storage ring as well as the electron filling pattern the facility was running in. Most experiments were performed with a 16-bunch filling pattern (16 electron bunches in the storage rings to produce x-rays), leading to a master clock time of 160-176 ns, however some experiments was performed in single-bunch mode with a 1178 ns period between successive x-ray pulses. Fortunately the disparity between these times did not greatly affect image acquisition time since the CCD data transfer rate was the limiting factor. Whilst data was typically collected by the CCD in under 1 second, the CCD required 4-6 seconds to transfer the data to the PC.

Whilst a synchrotron is capable of achieving time-resolution of down to 25 ps (depending on electron bunch filling pattern), we did not go beyond 250 ps due to the lengthy data collection time ($\sim$40-60 minutes). However 250 ps was a more than suitable precision since the dynamics we were investigating did not progress further than the spatial-resolution of the HERALDO technique ($\sim$20-40 nm) within this time-frame.

We were able to combine images of the experimental data into animations of the observed gyration dynamics by obtaining images for the different phases of vortex core gyration. The magnetic pulses from the generator were delayed by intervals of fixed length corresponding to different time instances from the moment of initial rise of the pulse to the time of fully damped gyration. Given the limited available beamtime and the substantial acquisition time a particular focus was given to the initial stage of vortex actuation and the first two cycles of gyration where possible since these were the largest in amplitude.

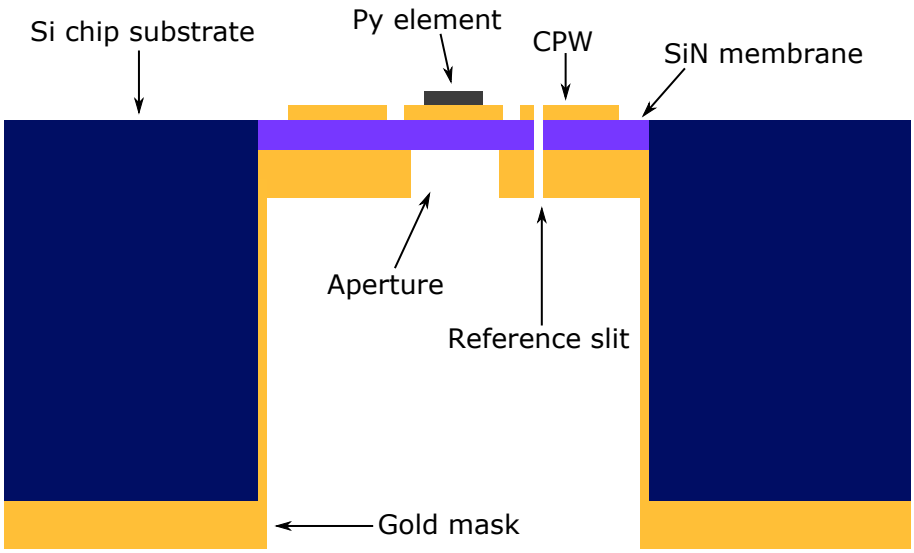

Figure 3.5: Cross-section schematic of the sample layout. The silicon chip substrate is 500 μm thick and served to support the 200 nm thick silicon nitride (SiN) membranes. The gold mask was 600 nm thick and deposited on the underside of the chip in order to absorb x-rays. Four 70 nm thick CPW's were deposited on the top-side of the sample, one per SiN membrane, each of which supported a single row of 80 nm thick Py magnetic elements. Apertures was milled through only the gold mask using FIB above where the Py element of interest was situated whilst the reference slit was milled through the entire sample structure in the right-hand-side ground strip of the CPW.

3.3 Sample Preparation

3.3.1 CPW and Py element fabrication

The substrate for all samples was a 5 mm x 5 mm x 200 μm silicon chip which supported four silicon nitride membranes in a 2 x 2 arrangement. The silicon nitride, Si_3N_4, membranes themselves were 500 μm x 500 μm x 200 nm and were used for their relative transparency to x-rays, allowing transmission measurements to be performed. Figure 3.5 shows a schematic of

A 600 nm thick gold (Au) mask was thermally evaporated onto the underside of these chips in a 6-layer structure of 5 nm Cr and 100 nm Au. This was required to absorb the x-rays and allow milling of aperture and reference structures in order to define regions that will be transparent to the x-rays.

By using standard electron-beam lithography (EBL) patterning, developing,

thermal evaporation of Au and lift-off techniques, four shorted integrated CPW's were fabricated on the top of the chip, one for each of the silicon nitride membranes. Markers at the corners of the chip were also patterned in this step and were used to align and focus the Py pattern along the central signal line of each of the four CPW's. The CPW was designed to match the 50 Ω impedance of the SMA connection to the Agilent 81150A pulse generator. Matching this 50 Ω impedance was necessary in order to allow optimal transference of the electrical signal from the pulse generator to the CPW which allowed for stroboscopic measurements to be performed.

Parameters affecting CPW impedance include the CPW length, thickness, core width, ground widths and the distance between the core and ground. Different core widths of 3 μm and 5 μm were tested, the theory being that a smaller diameter core width should produce a larger magnetic field due to the increased current density of the pulse from the signal generator. However the smaller width core led to impedance values of 85-120 Ω which reduced the transmission of the signal to the CPW. A 5 μm width CPW led to impedances of 45-80 Ω which was much more acceptable and closer to the output impedance of the pulse generator.

The free-standing Py elements were fabricated next by using standard EBL patterning, developing, Py magnetron sputtering and lift-off processes. The dimensions of an individual Py element was generally 2 μm x 2 μm x 80 nm with an edge-to-edge inter-element spacing of 2 μm, however some samples used elements of different sizes which will be mentioned in their relevant chapters.

The CPW had three wide lanes that ran to near the edge of the supporting silicon chip, ending in large gold pads which allowed connection via gold wire bonds to a larger chip-mounting CPW. Figure 3.6 shows the physical layout of a chip containing four samples that was wire bonded to the external sample-mounting CPW. The sample was then connected to the Agilent 81150A signal generator via a 50 Ω SMA cable. The mounting CPW contained a large hole beneath where the chip was mounted in order to allow x-ray transmission, including at off-normal

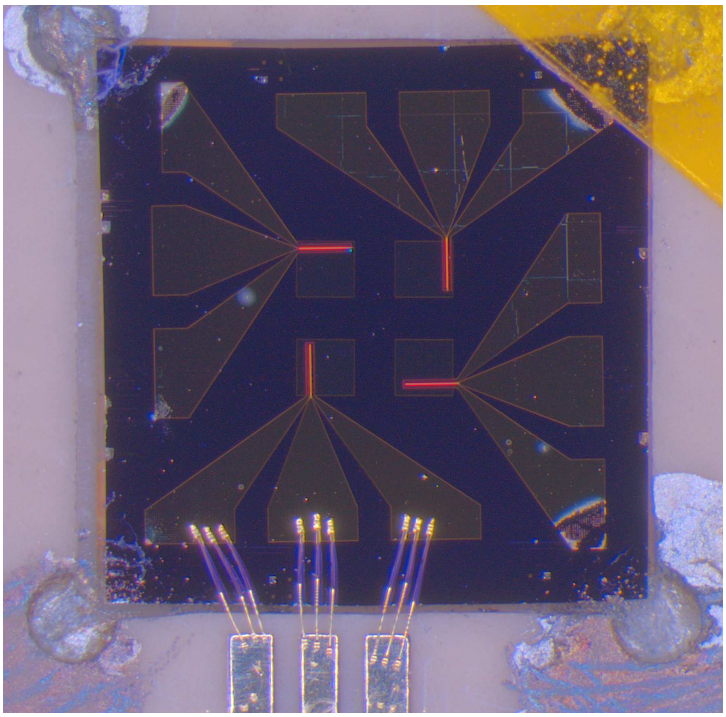

Figure 3.6: Optical microscope image of a silicon chip mounted to a sample-mounting CPW used to connect a sample to a signal generator via SMA connection and allow mounting in a vacuum chamber during an experiment. The four silicon nitride membranes are visible as the gold/brown squares near the centre of the large purple/blue silicon chip. Each of the membranes have an associated gold CPW with large tracks leading to the edges of the chip to allow gold wire bonding, as seen in the bottom sample. 3 gold wire bonds were used for each pad to ensure good contact for electrical conductivity and to add redundancy in the event that some of the wire bonds detached during transport to a synchrotron.

angles.

3.3.2 Reference slit and aperture milling

After the CPW and Py structures were fabricated, but before wire bonding to the chip-mounting hardware, FIB milling of the apertures and reference slits was performed using an *FEI Nova NanoLab D0071 dualbeam system* to create the devices used for imaging. A single sample contained 3 to 9 devices along the length of its CPW, based on Py element and CPW positioning on the membrane. The reference slit was made first by milling a 6 μm wide line in the right-hand-side ground strip (sample oriented with wire bonding pads towards the bottom). The centre of the slit was positioned 3 μm down and 7 μm to the right of the centre of

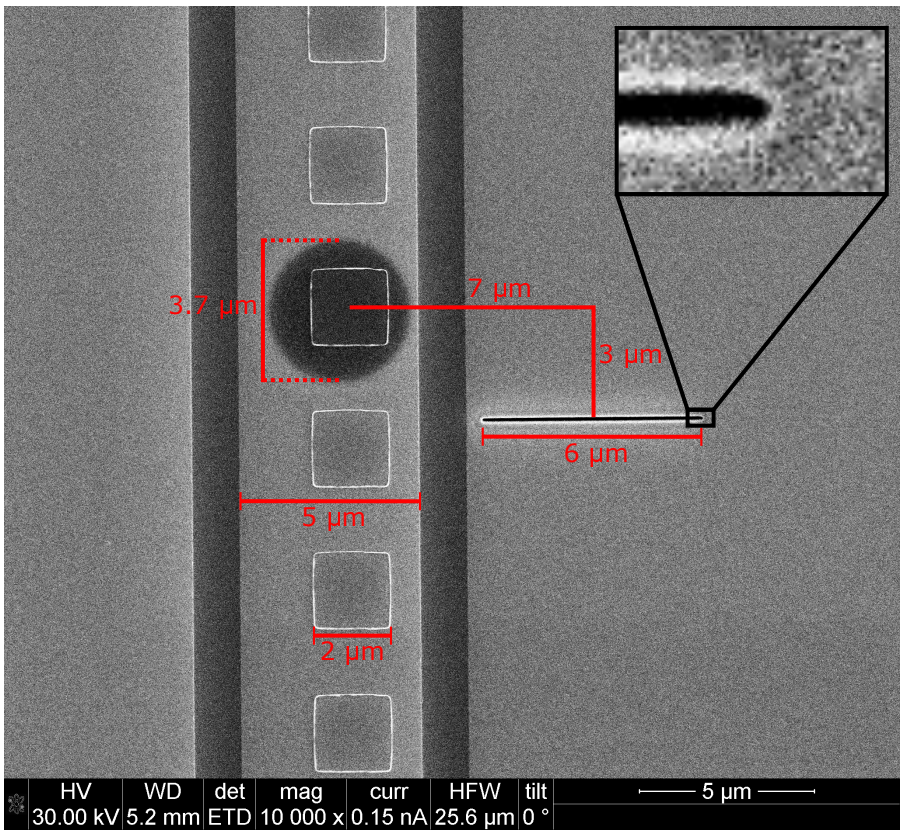

Figure 3.7: SEM image of a device, displaying the positioning of the aperture (dark circle) and reference slit (black horizontal line) relative to a Py element, which all together create a device. The image was taken using a 30 kV and 0.15 nA beam where the electron penetration depth was enough to observe the aperture present on the opposite side of the element, CPW and membrane. CPW orientation is such that the tracks leading to wire bonding pads are beyond the lower edge of the image, thus the pads are referred to as the ”bottom” of the sample. Information on all important aspects of the milling process are detailed in red. Insert: close-up of the edge of the reference slit to show its quality and shape. The top-side of the milling is wider and more rounded than the exit-side.

the Py element, as shown in fig. 3.7.

The position of the reference slit relative to the Py element was specifically chosen in order to keep the slit close enough to the aperture to produce a high quality interference pattern without creating an overlap between the aperture auto-correlation with the aperture and reference diffracted beam cross-correlation. Additionally it was important to mill the slit exactly perpendicular to the length of the CPW in order to prevent mis-alignment when tilting the sample in the chamber. A small deviation from this may result in the walls of the slit through the chip and mask blocking the x-ray beam from going through the slit, resulting in zero x-ray flux through the reference. An aperture was milled through the Au mask on

the rear side of the sample. This was placed opposite to the Py element, as seen in fig. 3.7 by the dark circle. The aperture defined the object region where the x-rays passed through in order to interfere with the x-rays that passed through the reference slit, creating a hologram that contained the magnetic information of the Py element.

It was important to ensure the aperture remained confined to within the CPW signal line. If it were to extend into the gap region between the signal and ground strips then the diffraction pattern obtained will have reduced contrast. This results from the lack of gold in this region leading to a high-intensity of x-rays passing through, saturating the CCD with light that contains no magnetic information. This reduced the overall contrast of the magnetic domains as shown in fig. 3.8. Taking this into account by ensuring the aperture was no larger than the CPW core width, this made it possible that the aperture was slightly too small for the Py element when the sample was tilted to the x-ray beam. This resulted in the aperture covering up some of the corners of the element when imaging at an angle. This was an acceptable trade-off however since the majority of vortex dynamics that were investigated in this thesis occurred within the centre of the element and not necessarily within the corners. Additionally at least two of the corners were always visible.

3.3.3 Data Comparison

Whilst a comparison can be made between the data presented throughout this thesis and that published in [99] and [100], it is difficult to quantitatively define what resulted in objectively clearer data. There is a broad range of aspects which affect reconstruction quality, from sample fabrication (reference slit size, shape and overall quality and accurate placement of the aperture over the CPW signal line), how well optimised the synchrotron beamline was (beam coherence and energy, distance between the sample and CCD and the difference in intensity between the two x-ray polarisations) and the accuracy of the MatLab reconstruction

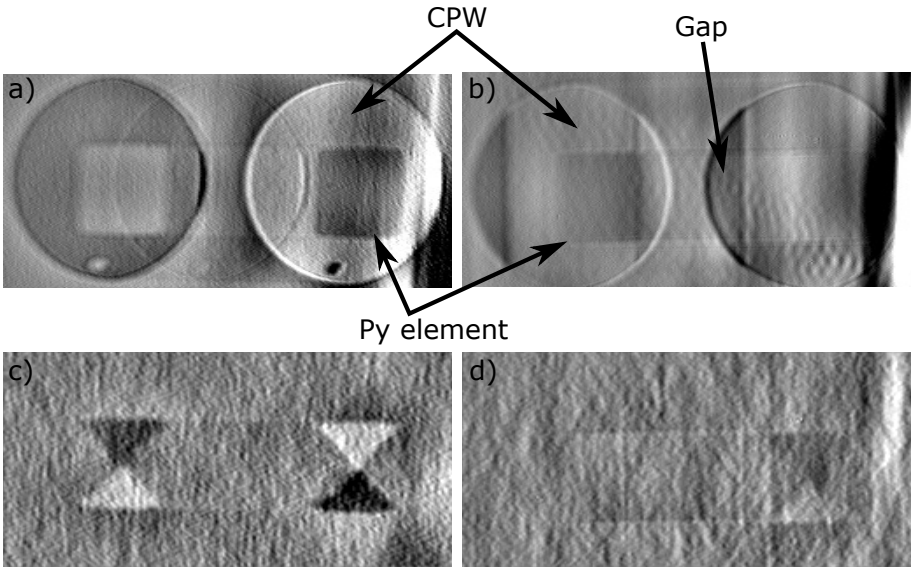

Figure 3.8: Reconstructed images of the charge, a) and b), and magnetic, c) and d), structure of an 80 nm thick Py square element with edge lengths of 2 μm x 2 μm. The devices in a) and b) had the same 5 μm diameter aperture however the CPW core width in a) was 5 μm whereas in b) it was 3 μm wide. This gave rise to the gap region, labelled in b). The quality of the reconstructed image of the magnetic state in c) is far superior to that seen in d) with a noticeably more well-defined contrast within the Landau pattern. This is also despite the fact that the data acquired for the reconstruction shown in b) and d) had a slightly higher photon count on the CCD of $3.4e^{11}$ vs $2.86e^{11}$.

(accurate positioning of the directional derivative filter and using the right normalisation factor to correct for any difference in x-ray polarity intensity). Magnetic contrast, data normalisation and spatial resolution can be improved by optimising these factors and is shown in table 3.1.

As mentioned previously in this thesis, the quality of the reference slit is one of the factors which affects spatial resolution along with the distance between the sample and CCD. Unfortunately it was difficult to quantify the effect of slit quality since the measurements ideally had to be performed during the same experiment at the same synchrotron beamline in order to remove the variation between different synchrotron facilities and prevent future recalibrations from affecting the obtained data. Since the time during an experiment was limited we were unable to justify taking the time to investigate this, especially as all samples tended to result in similar values of $\sim$35 nm per pixel. In fact the best resolution we managed to obtain was $\sim$20 nm per pixel which was achieved by moving the sample within

Property	Affects	Degree
Reference slit quality	Spatial resolution	Moderate
Aperture placement	Magnetic contrast	Large*
X-ray energy & beam coherence	Magnetic contrast	Large
Sample-CCD distance	Spatial resolution	Large
X-ray polarisation intensity	Normalisation	Large
MatLab filter placement	Overall reconstruction quality	Moderate
MatLab normalisation factor	Normalisation	Small**

Table 3.1: A list of controllable parameters, what aspect of image reconstruction they affect and to what degree the optimisation of the parameter can affect this aspect. *Aperture placement can only negatively affect magnetic contrast if placed such that it exposes the gap region between the CPW ground and signal lines. **If the x-ray beam polarities are not of similar intensities this can be somewhat corrected for by use of a normalisation factor within the MatLab script. This factor multiplies one of the polarisation data sets to make it roughly equal in intensity to its corresponding opposite polarity.

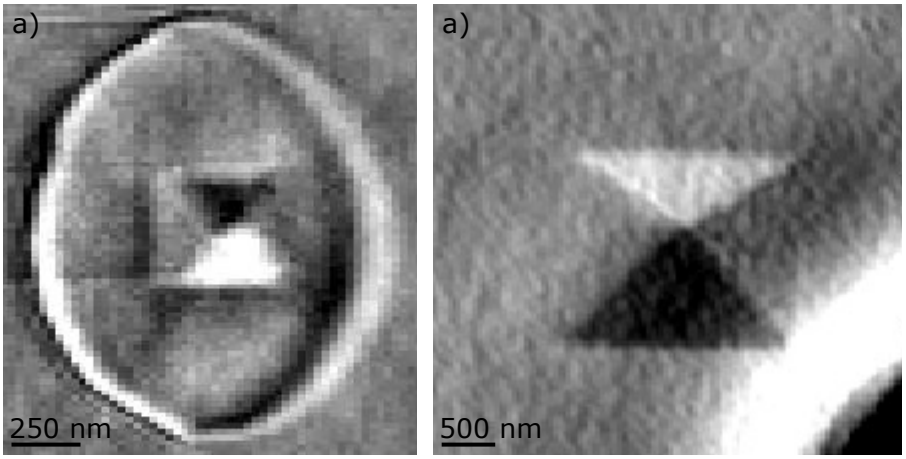

Figure 3.9: Experimental images collected in a) 2013 and b) 2017. Whilst spatial resolution between the two images is comparable (both $\sim$35 nm per pixel horizontally), the contrast in b) is more well defined and sharp with regards to the domain walls. Additionally the correct normalisation of the data in b) results in the removal of the aperture from the reconstructed image.

the chamber closer to the CCD from 35 cm to 18 cm. Perhaps then there is a link between a better quality, smaller reference slit allowing for better pixel resolutions as long as it is accompanied by moving the sample closer to the CCD.

Data normalisation is affected by the difference in x-ray beam polarity intensities. When the difference is large then the contrast is skewed such that one appears more intense than the other, however a normalising factor can help correct for this by multiplying the less intense data to become equal to the other. Similarly if the x-ray beam drifts across the sample, this will result in a difference

between the polarity intensities. A small deviation can be corrected for with this normalisation factor, however large drifts will make non-magnetic information be mixed in with the magnetic data, as shown in fig. 3.9. This cannot be corrected for with the normalisation factor due to the difference in frame of reference between the data sets, making the differential filter no longer apply to both data sets. If beam drift is occurring, usually due to the synchrotron beam optics heating/cooling after recent maintenance, the sample must be incrementally moved during measurement in the direction the beam is drifting to ensure the beam illuminates the same part of the sample when collecting data. The more frequent and minute the correcting movement is the better image quality is retained.

Chapter 4

Time-Resolved HERALDO and 3D Landau Domain Structure

This chapter will present the results of the samples discussed in section 3.3. The text will be adapted from the paper published in *Scientific Reports* which can be found with the DOI:10.1038/srep36307 in reference [101]. Supplementary material can be found there online which includes animations of experimental data which are not able to be included in this thesis. Mr. Conor McKeever produced the simulations presented in this chapter.

4.1 Introduction

In recent years, vortex closure domains in magnetic thin-film elements have become the focus of great attention due to their intriguing dynamic properties. As well as being fascinating model objects – in many aspects the vortices behave like classical harmonic oscillators – they are considered as promising new magneto-electronic components, which could provide a wide range of functions, stretching from static non-volatile high-density data storage [102] to dynamic skyrmion excitations [15, 16, 103] and magnetic vortex generators [7, 8, 9]. The latter have particularly attracted much interest after it was demonstrated that, similar to an

spin-torque oscillator (STO), a magnetic vortex can be driven by either AC or DC currents and perform as a microwave oscillator [9, 12, 23, 104, 105, 106, 107, 108, 109]. In comparison to an STO device, a magnetic vortex is a natural and more coherent resonating system, which is less affected by imperfections in the geometry of the material and its intrinsic parameters. However, the understanding of vortex dynamics remains complex, especially in matters regarding nonlinear effects. In case of thin film patterned magnetic elements, such as microscopic Py squares or dots, the focus of research has been covering a number of topics including the understanding of the eigen-modes of gyration in single elements [23, 80, 81, 102, 104, 109], coupled oscillations in assemblies or patterns of elements [82, 110, 111, 112, 113, 114, 115], non-linear effects [41, 110, 116, 117], manipulation of core dynamics [12, 23, 104, 109] and their practical application [9, 12, 23, 105].

In many cases the investigations have been based on time-resolved imaging using optical [118, 119, 120, 121] or x-ray techniques [80, 122, 123, 124, 125]. The spatial resolution in the best case is limited to the wavelength of the optical probe convoluted with the specifics of the particular techniques and their limitations. For example, in the case of soft x-ray imaging the typical values are in the region of 20–50 nm. This is insufficient to clearly resolve the vortex core or domain walls with dimensions $\sim$10–15 nm. In the majority of investigations these limitations were compensated by simulation studies using micromagnetic numerical tools, such as MuMax [38], from which one can further assess the effects that may not be clearly resolved in spatial imaging. This also facilitated study of the finer structure of the vortex closures and its dynamics [27, 104, 126, 127] and to investigate non-linear effects and spin-wave phenomena associated with both the excitation and the steady states of the vortex gyration. The latter are of particular importance in technological applications, where vortex core manipulation underpins their operation (e.g. polarisation switching). Numerical work is also invaluable to understand the 3D structures of the domain closures, as these are normally 'hidden' for the experimental probes (e.g. in x-ray transmission experi-

ments), because of averaging or insensitivity to in-depth magnetisation.

Here we report the first demonstration of time-resolved imaging of vortex gyration using HERALDO. This relatively new technique [96] has recently been adopted for imaging of magnetic materials [94, 99, 100, 128]. Similar to most synchrotron-based magnetic techniques, it uses XMCD [59, 129] to probe the magnetisation with element-specificity, for which magnetic contrast is observed for magnetic moments aligned parallel or anti-parallel to the x-ray wave vector. Based on the principles of holography, HERALDO uses the interference between the reference beam and the scattered light from the sample to reconstruct the real-space magnetic contrast [96]. Compared to standard FTH [63, 130, 131], in HERALDO the reference beam is produced by a slit rather than a hole (see fig. 3.4). One of the advantages of this modification is the ability to image both out-of-plane and in-plane magnetic components by performing measurements at normal ($90°$) and acute (e.g. $45°$) angles of x-ray incidence with respect to the sample surface.

Here we employ HERALDO for time-resolved imaging of the magnetic vortex gyration in thin-film magnetic Py squares. Similar to circular elements, in these structures the vortex is formed as a result of minimisation of the magnetostatic energy, forcing the magnetic moments to stay preferably in-plane of the element. However, due to the influence of the straight edges, as well as creating the vortex core, the square elements tend to form $90°$ domain walls, breaking the sample into four equi-sized triangular domains, forming a so-called Landau flux-closure pattern [10, 18, 119]. The dynamics of the core in this case are also affected by the mobility of the domain walls and the associated magnetostatic energy. Furthermore, it was shown that the structure of the core itself and its dynamics can be greatly affected by the film thickness of the elements [132]. Here we present a study on relatively thick (80 nm) Py elements since investigations involving thin elements (typically $<$50 nm) has already been studied quite extensively. As well as the gyration of the core studied by x-ray imaging and micromagnetic simulations, we also examine the overall 3D structure of the magnetic configuration and

its dynamics during the first cycles of excitation. In particular we focus on the associated spin wave phenomena and investigate the wave propagations localised within the domain walls of the element.

4.2 Methods

4.2.1 HERALDO Measurements

Samples were fabricated via the methods described in section 3.3. The initial tests and optimisation of x-ray holographic measurements were carried out on the beamlines ID32 (ESRF) and SEXTANTS (SOLEIL) using 16 bunch ($\sim$70 mA) and 8 bunch ($\sim$80 mA) filling modes. The final results presented here were taken at SEXTANTS, using a single bunch mode with an average current of 17 mA. In order to produce the pulsed magnetic field we used a shorted CPW antenna, which was formed from an 80 nm thick Au film deposited onto a SiN membrane using standard photo-lithographic processes outlined in section 3.3.1. The width (5 μm) and separation (1 μm) of the CPW were chosen to maintain the characteristic impedance of the microwave electronics (50 Ω) in order to enhance the current density within the antenna and the resulting magnetic field strength.

The pumping was achieved with electric pulses, which were generated by a 330 MHz 3.8 V pulse pattern generator (Agilent HP 81110A + 81112A). The pulse length was 20 ns. The two pulse amplitudes (7.7 mT and 10 mT) were produced with the generator output of 3.0 V and 3.7 V respectively. To allow for a sufficient period of gyration, the rise-time of the pulses were set to the minimum possible setting of the generator ($\sim$800 ps) to provide the necessary bandwidth excitation in the MHz/GHz region [81, 104, 133]. The individual x-ray pulses in single bunch mode were separated by 1181 ns and had an average width of 25–30 ps. The transmitted x-rays were recorded on a CCD camera positioned on the optical axis behind a beam stop for the direct, undiffracted beam. The distance from the

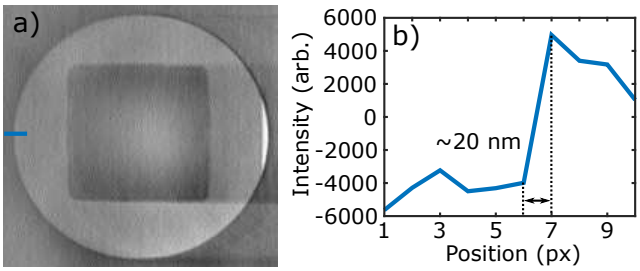

Figure 4.1: a) Reconstructed charge (structure) image of a 2 μm Py square element. Blue line shows where the line scan in b) is measured through. b) Line scan shows the intensity of the pixel positions, showing a 1 pixel shift from maximum negative to maximum positive values of intensity.

camera to the sample was set to 25 cm, resulting in a minimum spatial resolution of $\sim$20 nm, shown in fig. 4.1.

To obtain holographic images the sample had a reference slit that was isolated from the object area by a distance corresponding to at least twice the aperture diameter and within the x-ray coherence length ($\sim$25 μm). The interference pattern of the direct and diffracted x-rays was recorded on the CCD for left and right-circularly polarised x-rays, which were subtracted and then operated on by the directional derivatives and Fourier transformed to obtain the real-space image. The magnetic images were taken at a photon energy of 707 eV coinciding with the Fe L_3 absorption edge.

4.2.2 Micromagnetic Simulations

Micromagnetic simulations of 2 μm Py squares with thickness 83 nm were performed using the MuMax micromagnetic solver [123]. Standard parameters for Py (saturation magnetisation, $M_s = 8 \times 10^5 Am^{-1}$, exchange constant, $A_{ex} = 1.3 \times 10^{-11} Jm^{-3}$ and Gilbert damping, $\alpha = 0.008$) were chosen, [134], with cell-size $x = 2000 \div 512 = 3.90625\,nm$, $y = 2000 \div 512 = 3090625\,nm$, $z = 83 \div 16 = 5.1875\,nm$ and negligible magnetocrystalline anisotropy. Vortex precession was induced by a step pulse with maximum amplitudes of 7.7 mT and 10 mT and rise-time of 1 ns. The field profile decays as $1/(r_0 + r)$ through the thickness of the square element with $r_0 = 40\,nm$ representing the half thickness of the antenna.

The lateral variation of the field (close to the edges of the central CPW conductor) was neglected. The dot product of the vector magnetisation was calculated with respect to a 135° (see fig. 4.5b) and perpendicular (see fig. 4.6 and fig. 4.7) orientation to the x-ray beam and the magnetisation was averaged across the thickness at the corresponding angle.

4.3 Results

The experiments were carried out in the stroboscopic regime [23, 80, 81]. The overall schematic of the pump-probe measurements using HERALDO is illustrated in fig. 4.2a, and described in detail in section 4.2. Synchronisation between the magnetic pump and x-ray probe pulses was achieved by using the master oscillator clock of the synchrotron, which served as the trigger signal for the pulse generator, the process of which is described in detail in section 3.2. Overall, we imaged 29 points starting from t_0 and ending at $t_0 + 10\,ns$, with a typical step size of 250 ps and an average spatial resolution of 30 nm (40 nm) in vertical (horizontal) direction.

For imaging in perpendicular orientation (see fig. 4.3a) an enhanced spatial resolution of 20 nm in both vertical and horizontal directions was achieved by moving the CCD camera closer to the sample. The reconstruction of the magnetic contrast was performed in the same way as previously reported [99, 100]. The difference between the diffraction patterns for the two polarisations of opposite circularly polarised light was multiplied by the intensity matrix representing the differential filter. The resulting image was then Fourier transformed to obtain the real-space magnetic contrast (see fig. 3.4). Figure 4.3 shows the results of the reconstructions from the data obtained at different delay times between t_0 and the x-ray probe pulse. Imaging was carried out at two different x-ray angles of incidence (90° and 45°) with respect to the sample surface, and for two different pulse amplitudes (7.7 mT and 10 mT), respectively. Figure 4.3a and b depict

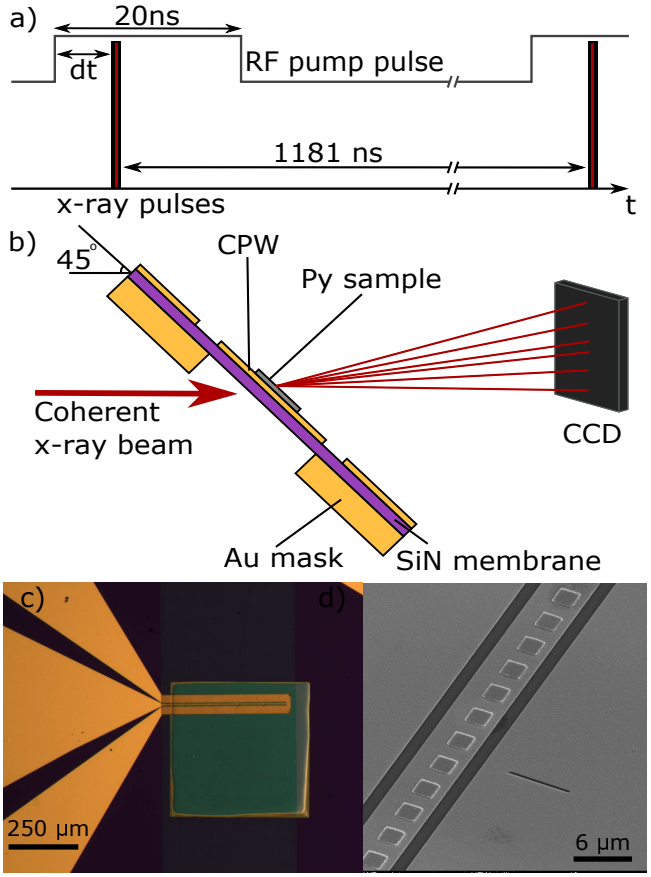

Figure 4.2: Experimental set-up and time structure of the experiments. a) Pump-probe time structure used for pulsed stroboscopic imaging. b) Sample geometry with respect to the x-ray beam for $45°$ imaging (for perpendicular imaging the sample surface plane was at $90°$ to the x-ray beam). c) Optical microscope image of the sample showing the gold CPW on the Si substrate and SiN window. d) SEM image showing the Py squares, CPW structure and reference slit from the front side of the sample. The aperture was on the rear side of the sample in the integrated gold x-ray mask. Each CPW contained multiple apertures and reference slits separated by 100 μm.

typical images of the magnetic contrast in the area of the vortex core acquired at $90°$ and $45°$ respectively. The overlaid lines trace the positions of the core at different delay times. Figure 4.3c shows the vertical displacement of the vortex core as a function of delay time for each magnetic pulse strength, as well as the results of micromagnetic simulations. Figure 4.3d shows the spatial positions of the core extracted from all frames imaged at perpendicular $(90°)$ orientation of the x-rays with respect to the sample. Supplementary movies S1, S2, and S3 show the combined time-resolved images for both sample orientations and can be found online in [101].

Figure 4.3c shows that, as time progressed from t_0, the vortex core was first

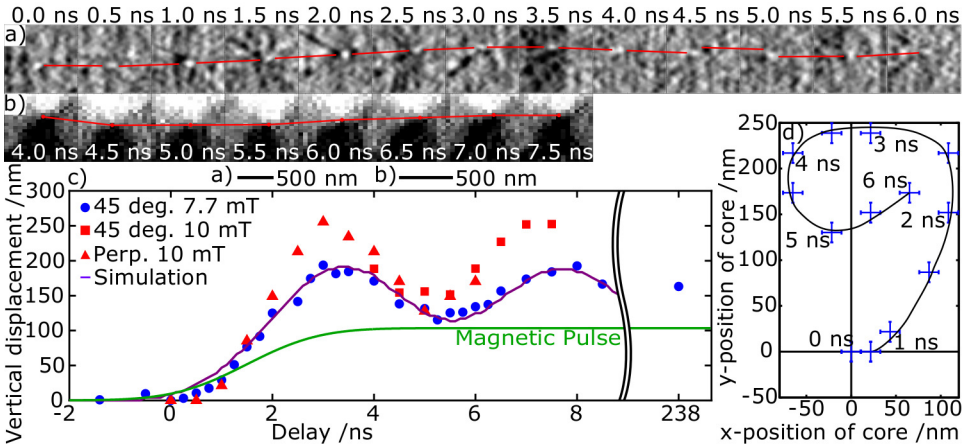

Figure 4.3: Vortex gyration. Close-up of the reconstructed magnetic contrast around the core taken at different values of the delay time, dt, for a) $90°$ and b) for $45°$ (3.7 V pulse) angle-of-incidence. The red lines trace the vortex core position. c) The vertical displacement of the vortex core at different delay times and magnetic pulse strengths. The purple line shows the vertical displacement extracted from micromagnetic simulations. The simulated magnetic pulse profile is shown by the green line. The point at 238 ns delay gives the vertical position of the core after being fully damped, the pulse length of which was increased to 500 ns to allow verifying the vertical position of the core in this case. d) The position of the vortex core in the xy plane at various delay times imaged in perpendicular orientation.

displaced vertically (along the CPW) after which it follows a continuous precession around a new equilibrium position. This new position was determined by the amplitude of the magnetic pulse and, once the gyration was fully damped (after ∼30 ns), has the same vertical displacement as would have been induced by a constant applied field with the same magnitude as that of the pulsed field. As in experiments on circular elements (e.g. [115, 117]), sufficient bandwidth ($\Delta f \approx 1/\Delta t$) for excitation of eigen-modes of the vortex gyration was provided by a pulse with a rise time of $\Delta t \approx 1$ ns. To match the amplitude of gyration with that produced in the simulation we used a Gaussian smoothing of the pulse, shown by the green line in fig. 4.3c, which leads to a further reduction of the dynamic bandwidth, but more realistically describes the experimental capabilities of the generator and the transmission lines. In the simulation, we also assumed a non-uniform structure of the field, which was inversely proportional to the distance, r, from the antenna according to the relation $B = B_0 r_0/(r_0 + r)$, where $B_0 = 7.7$ mT is the field at the surface of the antenna, and $r_0 = 40$ nm is the half-thickness of the antenna. As explained below, this non-uniform nature of the field plays

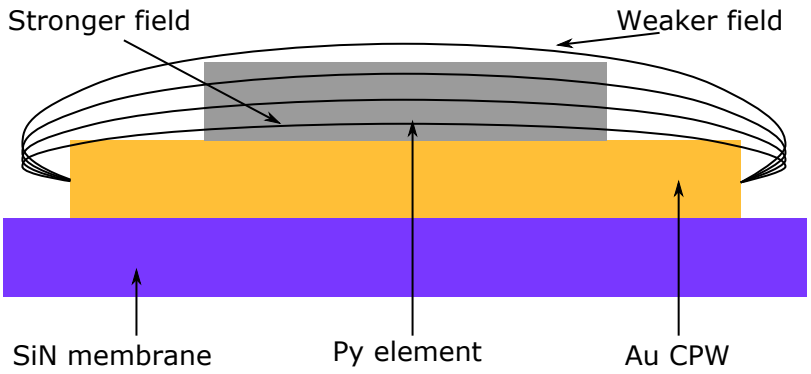

Figure 4.4: Schematic depicting the weakening of the bias field from the CPW through the Py element. This weakening was implemented within simulations in order to more accurately depict magnetic dynamics. The bottom layer of the Py element, which is in contact with the CPW, experiences a stronger bias field compared to the top of the element, with a linear field strength reduction for each subsequent layer upwards.

an important role in the dynamics of the domain walls. A schematic of the field weakening is shown in fig. 4.4.

Based on previous studies, the gyration frequency is primarily determined by the geometric parameters of the element and is proportional to the thickness-to-length aspect ratio of the square [132, 133]. In our measurements on a square of 2 μm long and 80 nm thick, the period of the first cycle of gyration was found to be $\sim$4.5 ns. This value is in good agreement with that obtained by the micromagnetic simulations. The reduction in the amplitude of gyration was also in agreement with the simulation, in which the damping coefficient of Py is set to its standard value of $\alpha = 0.008$ [118].

4.3.1 Core Structure

As mentioned above, to obtain the in-plane magnetisation contrast imaging was performed at 45°, providing the required non-zero in-plane projection of the x-ray wave vector. However, regions with out-of-plane components will also result in a non-zero magnetic contrast, thereby providing more information about the overall domain structure. In particular this was important for thicker elements in which the increased aspect ratio leads to non-linear regions with large variations of the

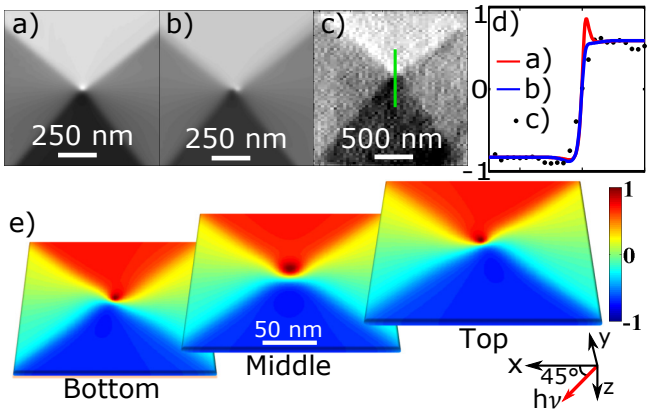

Figure 4.5: Vortex core structure. Simulated normalised magnetic contrast with averaging of the thickness in a) a perpendicular orientation and b) over a $45°$ orientation. c) Reconstructed experimental image obtained for the same delay time. d) Vertical intensity profiles through the centre of the core for all three images a), b) and c) as shown by the vertical green line in c). Positive values correspond to magnetisation vector parallel to the x-ray wave vector (white). e) Simulated images of the magnetic contrast for different layers within the structure. From left to right, the images represent the bottom 1st, middle 8th and top 16th layer of a 16-cell thick simulation grid (cell size was 3.9 x 3.9 x 5 nm^3). Colour coding: Positive (Red) and negative (Blue) normalised magnetic contrast in the x-dimension.

magnetisation vector. Figure 4.5 shows the magnetic contrast in the vicinity of the vortex core obtained experimentally, c), and extracted from micromagnetic simulation, a) and b). Two particular aspects arising from off-normal imaging are related to the angle of observation. Firstly, the maximum (zero) magnetic intensity is found for moments forming $45°$ ($135°$) with the sample surface (fig. 4.5a. These are the moments that are at opposite sides of the core centre and either parallel (black/white) or at $90°$ (grey) to the x-ray beam. Theoretically, the extension between the maximum intensity and its zero can be taken as the average dimension of the core.

Secondly, imaging at $45°$ results in averaging of the magnetic contrast along the lines inclined at this angle. For thicker elements this meant that a projection of the vertical structure will also be present in the image. Figure 4.5b shows the simulation result of the experimental data in fig. 4.5c, in which the averaging was taken at $45°$. The area of the core shows a certain structure arising from the horizontal non-uniformity of the M_x component. A further examination of the simulation results for different layers of the element (fig. 4.5e) reveals that the structure

of the core is asymmetric towards the top and bottom layers, which are respectively mapped at their inclined projection. However, this structure was difficult to resolve, and experimentally it was exhibited only in the horizontal broadening of the core area as shown by the black dots in (fig. 4.5 d). Examining different phases of gyration shows a similar structure, indicating that this structure was the result of the static magnetic configuration. From previous numerical studies on thick elements [135], it is known that the structure of the core can be non-uniform, and this is generally related to the minimisation of the magnetostatic (dipole-dipole) energy across the thickness of the sample. Although this effect is relatively small, we speculate that it may play a role in the asymmetric dynamic effects of the domain walls described below.

4.3.2 Domain Wall Dynamics

Figure 4.6 displays the experimental and simulated images obtained for the perpendicular orientation of the x-ray beam. The contrast clearly indicates a point at the core, which was used to trace the gyration trajectory. This was particularly useful to identify the horizontal displacement, which cannot be easily extracted from the "in-plane" imaging at 45°. The images are also of sufficient quality to resolve the magnetisation structure of the domain walls. Analysing the contrast of the domain walls compared to those produced in the simulations, one can see the following dynamic effects. Before the magnetic pulse was triggered, all four domain walls showed a small out-of-plane magnetisation component, which has the same polarisation as the core (white). Once the magnetic field began to rise after t_0, two of the walls reversed to the opposite polarisation (black). This occurred through the formation of a 'bullet-like' excitation which propagated from the core towards the corners of the element and switched the positive component entirely or left a small domain close to the corners (not shown here).

The exact scenario depends on the magnitude and form of the applied magnetic pulse. A reasonably low pulse ($B_0 \approx 4\,mT$) can switch the polarisation of

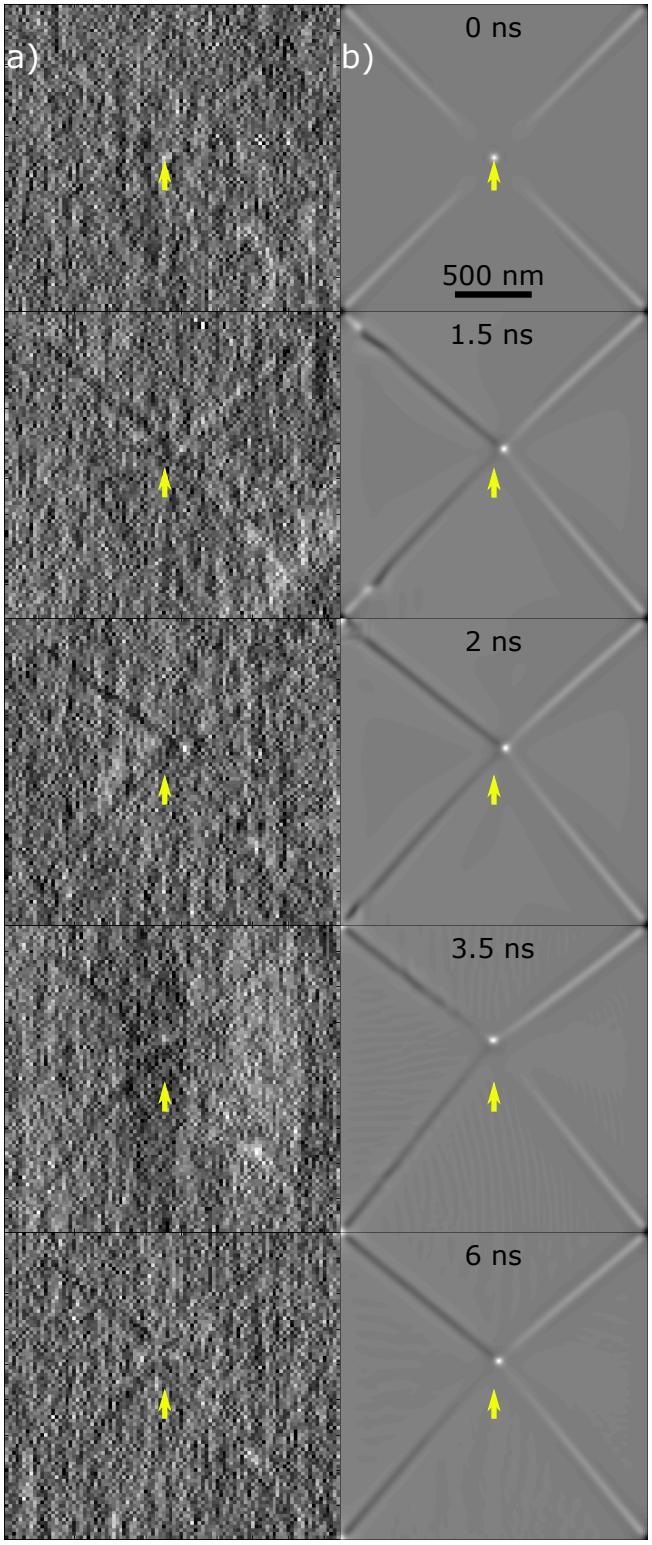

Figure 4.6: Domain wall dynamics. a) Experimental and b) simulated magnetic contrast of the domain structure imaged in perpendicular orientation at different delay times (from top to bottom): 0.0, 1.5, 2.0, 3.5 and 6.0 ns. The frames represent different stages of the pulse rise and gyration. The domain walls at the left-hand side in each image are predominantly 'black' (magnetised downwards), whereas those at the right-hand side are always 'white' (magnetised upwards). Yellow arrows have been inserted to point to the equilibrium position of the core.

both domains walls together with their corresponding corner singularities (see fig. 4.6 and fig. 4.7). A smaller pulse amplitude can lead to switching of only one corner singularity or none at all. In the latter case all four corner singularities maintained the same polarisation, but the domain walls partially changed theirs. Once the magnetic pulse reached its maximum, the core continued along its gyration trajectory. Once the core had passed its maximum displacement, the polarisation of the domain walls typically remained the same. Generally, if the magnetic field was non-uniform, all domain walls maintained their polarisation (two up and two down) and continued to oscillate with the core. However if the field was uniform, the bullets were still formed, but they could not switch polarisation in the corners and after some period of sporadic motion the polarisation of all domain walls returned to their initial states (see supplementary videos S4 and S5 in [101]).

It should be noted that in our simulation study the corners of the elements were ”ideal”, so the effect of singularities was significantly pronounced. In the experiment however, due to lithographic imperfections these singularities became broadened and therefore less intense than the vortex core. This was also a likely reason why the polarisation of the corners could be switched by the onset of the pulsed magnetic field, thus leaving the combination of two black domain walls and two white domain walls that were unchanged during the core gyration (fig. 4.6a). Based on the simulation results we also note that, similar to the vortex core, the 3D structure of the domain walls was also non-uniform. Figure 4.7d shows how the domain wall structure changed across the thickness of the square. The larger contrast corresponds to the middle layers of the structure, whereas at the surfaces the effect was mostly suppressed. It was found that the formation of the bullets and their propagation strongly depended on the field gradient. If the amplitude of the field was larger at the bottom layers of the element (as was the case in our experiment), the bullets were formed in the left-hand domain walls. However, if the sign of the gradient was reversed, the bullets would be formed in the right-hand domain walls and a similar dynamic scenario is obtained, but only

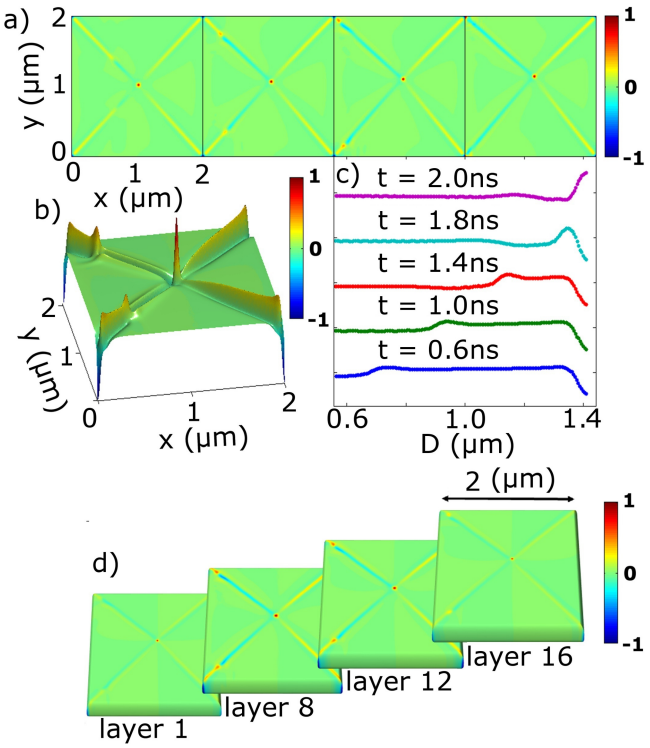

Figure 4.7: Simulated images of the domain wall structure. a) Perpendicular component of the magnetisation at different delay times of t_0 + : 0.3, 1.3, 1.8 and 2.3 ns. b) 3D depiction of the out-of-plane magnetic component, m_z, at 1.4 ns delay. A localised wave "bullet" is formed at the edge of the positively polarised part of the domain wall and propagates within the wall towards the corner. c) Intensity scans within the domain wall for different delay times demonstrating the profile of the "bullet" as it approaches the singularity at the corner and how it switches from negative to positive. d) The simulated structure of the domain walls for different layers throughout the thickness of the element. The simulation was 16 layers in total. The wave "bullet" structure is more pronounced in the middle layers.

with opposite polarisations of the left-hand and right-hand domain walls and their singularities in the corners.

We speculate that other factors would also likely affect the demonstrated dynamics, including the initial polarisation of the core and the singularities in the corners, the vertical structure of the core, the chirality of the vortex and the temporal structure of the magnetic field pulse. Here we simulated a particular case that provided good agreement with the experimental observations. However, further combined studies of experiments and micromagnetic simulation are required to understand the phenomenon in more detail.

4.4 Conclusions

In summary, we have demonstrated time-resolved imaging of magnetic vortex gyration using a novel technique based on x-ray HERALDO. Using micromagnetic simulations we have confirmed the eigen-frequency of the principal mode of gyration and explored the dynamics of the Landau closure domains at the onset of excitation and during the precession of the vortex core. We showed that the 3D structure and the dynamics of the core have a direct effect on the domain walls, which can change their out-of-plane polarisation and follow the gyration of the core depending on the state of the singularities in the corners of the Landau pattern. Additionally we showed that the change in polarisation was accomplished by the formation of ”bullet-like” excitations, which propagate within the domain walls and can also lead to switching the singularities at the corners. The latter are energetically related to the polarisation of the core and can reduce the energy required for switching its state. These effects are important for further understanding these systems because the manipulation of the vortex core and its dynamics are key factors in the prospective technology utilising vortex gyration.

4.5 Discussion

The information presented above was the culmination of several of the first sets of experiments that were related to this thesis. The experimental process was refined for successive experiments but essentially remained the same.

From the results we decided that CPW dimensions were to be revised in an attempt to improve the current density of the electrical pulse from the signal generator, leading to a stronger magnetic pulse as well as correctly matching the impedances. This would produce a larger displacement for vortex core gyration, making tracking of its position more accurate. Ultimately however, a 5 μm CPW core diameter was to be kept due to issues with impedance matching of smaller

CPW core diameters with the 50 Ω output of the signal generator. The smaller core diameter CPW's also tended to become critically damaged by the voltages required to supply the necessary current to produce a large vortex gyration. Additionally for the samples that were made of two overlapping Py square elements, detailed in chapter 6, a smaller CPW core diameter would not have been suitable due to the limitations this imposes upon usable aperture diameters before they begin to expose regions of the gap between the CPW core and ground lines. This was known to negatively impact the reconstructed image contrast.

Chapter 5

Polarity Switching via Topological Structures in Sample Surface

This section will discuss the simulations and experimental results investigating the effect a topological structure (physical defect) has upon the dynamics within the magnetic Landau closure domain structure. Unlike the results presented in chapter 4 where numerical simulations were performed after the experiment, here simulations preceded sample fabrication and experimental observations. The results of these simulations will be presented first, followed by the experimental results.

5.1 Simulations

5.1.1 Background

The initial concept to be explored was using a square Py element with multiple hole-shaped defects milled through it at equally spaced positions around its centre. These defects would be used to trap the vortex core within one then move it between the others by using an external magnetic field. This would allow switching between different magnetic states within the sample that can be maintained

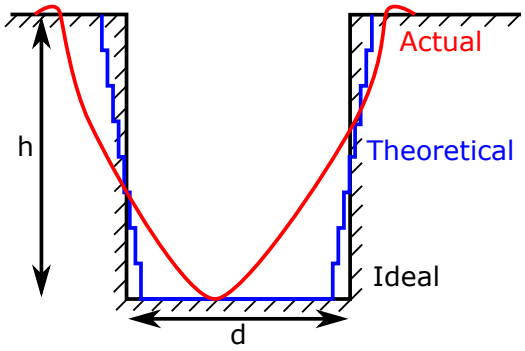

Figure 5.1: Sketch depicting the profiles of a defect of diameter, d, and depth, h. The black line is the ideal case scenario where the hole walls are completely vertical. In reality the defect ends up more like the red ”actual” line since the FIB has a Gaussian beam profile milled material re-depositits towards the top of and preferentially to one side of the hole, effects of beam dwell time, scan direction and others mentioned above [5]. The blue ”theoretical” line was used in simulations since it was impossible to quantitatively measure and recreate the real profile of the defect after FIB milling and this was the simplest way to recreate the effect.

indefinitely after the external field is removed. The defect was a region of the sample that was removed from the top layer downwards to a specified depth.

To test the ability of the defect to pin the vortex, its depth through the structure was varied in order to find the optimal depth needed to achieve vortex pinning. The defect was composed of multiple vertically-stacked cylinders of increasing diameter that occupied different numbers of z-layers (vertical) to vary the depth. The bottom-most cylinder had the intended diameter of the defect which then linearly increased in size as the cylinders approached the top layer of the element. This was in order to more accurately simulate the outcome of using a FIB to create the defects since the Gallium (Ga) ion beam has a Gaussian profile and so does not mill structures with perfectly vertical walls, instead the walls would be slanted. The outcome of defect milling with FIB is shown in fig. 5.1 and its comparison with the ideal and theoretical cases.

Simulations with a single hole of varying depths showed that in order to trap the vortex core within the defect it would have to be milled through the entirety of the Py square element (80 nm). Any less allowed the vortex to release from the defect and settle to its usual rest position once the applied field was removed. However a secondary result of the simulations was observed. A defect that went

through at least half of the element thickness but not all the way made the polarity of the vortex switch consistently from one polarity to the other across multiple magnetic pulses.

The ability to switch the vortex polarity would allow an extra level of control of the Landau vortex closure state that could have useful technological applications. An example of such an application is the potential to use the vortex polarity within the Py element to store information as a bit where one polarity corresponds to a binary 0 and the opposite polarity to a binary 1 state, as explained in section 2.2. The state could then be switched by application of a relatively weak bias field of 7.5 mT to 13 mT, depending on the parameters of the defect. It should be noted however that vortex polarity switching has previously been achieved by other methods, with both simulated and experimental results published [23, 26, 104]. However these differ in that they rely on the use of either an alternating magnetic field, a pulsed magnetic field or the use of spin-polarised currents, which tend to require higher field strengths compared to those used in the simulations discussed here.

The diameter of the cylinders used to form the defect increased based on the angle the walls of the defect would make. This would normally have been $\sim 15°$, as seen when cross-sectioning a structure milled deeper than a few 100 nm. However since the Py elements were no thicker than 80 nm the defect wall angle was larger, resulting in a more shallow-walled profile. An angle of $40°$ was therefore used as an estimate due to difficulties in quantitatively measuring the actual angle with SEM. The bottom cylinder had the diameter that the defect was intended to be and each cylinder above this was larger by a constant amount. Each cylinder within the simulations was made to fill an entire cell's vertical height of 5 nm.

5.1.2 Results

From investigations into the optimal defect position offset from the centre of the element, defect depth through the element and diameter, it was observed that

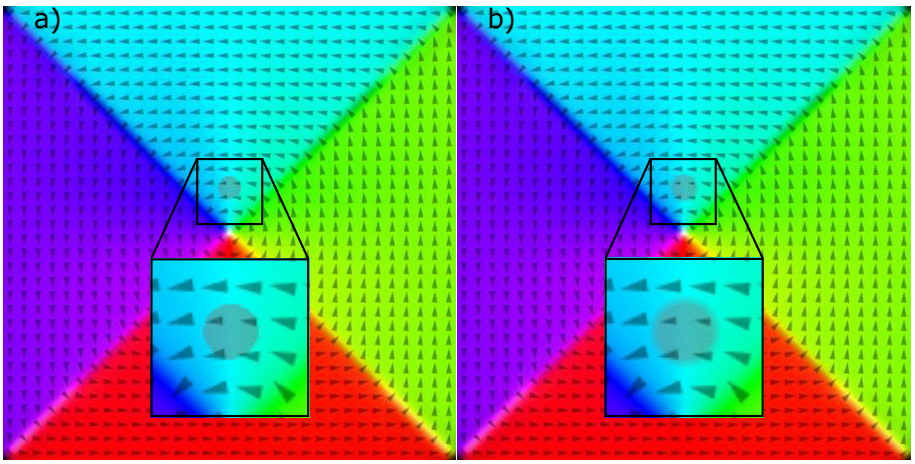

Figure 5.2: Images of initial state of a simulated Py square element with a) vertical and b) 40° walls of the hole. The circle is much more well defined in a) whereas in b) the edge is blurred. The sample represented by b) is closer to what will be reproduced experimentally due to the limitations of gallium FIB milling.

the offset from the centre of the Py element must be within a specific range; too far and the vortex was either unable to reach the hole without a suitably high field pulse or the defect did not capture the domain walls in the necessary way to induce the polarity switch. Too close however and the domain walls closest to the defect immediately become pinned, causing the vortex to simply gyrate around the edge of the defect but not switch polarity. The same is true for a defect that has too large a diameter relative to its offset from the centre of the element; too large a diameter but not far enough from the centre would result in the domain walls pinning immediately and no switch occurring.

Figure 5.3 shows the simulated process of defect-induced vortex core polarity switching. The switching process appears to be caused by domain walls being trapped by the defect which stops the lateral vortex motion as the vortex moves upwards in an anti-clockwise direction, shown in b). However due to the magnetic pulse still being present, the core attempts to continue moving vertically in its usual gyration path, inducing a strain in the magnetic moments between the vortex core and the defect. This strain forms a region of opposite polarity in the space between the defect where the domain walls are trapped and the vortex core itself, seen in c), which grows until the original vortex core becomes annihilated by this region, d). The new vortex then gyrates around the edge of the defect until

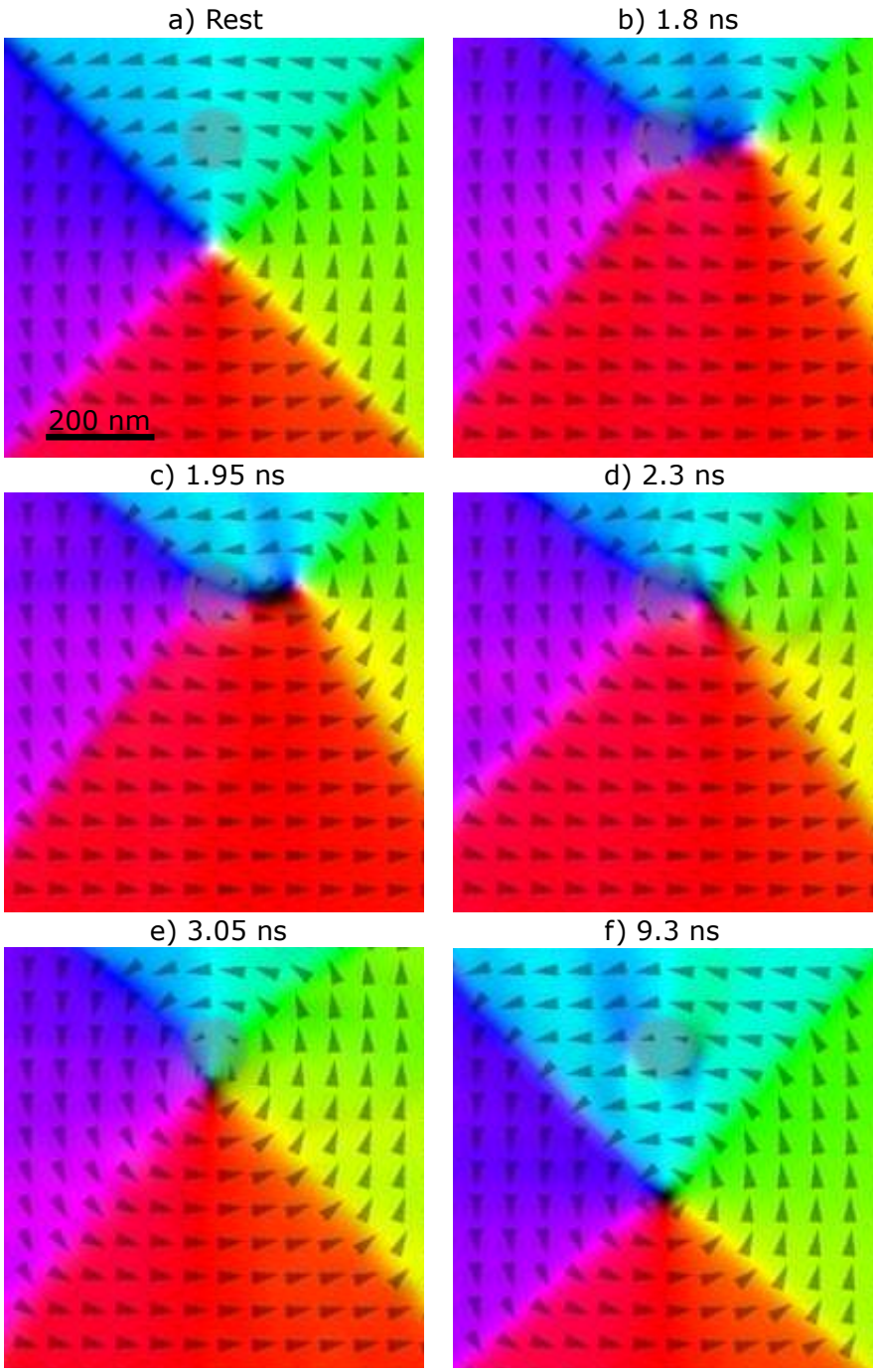

Figure 5.3: Simulated images of the vortex polarity switching process. The defect was 100 nm in diameter, had a 40° wall profile, was offset 200 nm vertically from the centre of the Py element and went down through 40 nm of the 80 nm element. The indicated times in ns represent the amount of time that had passed since vortex core gyration was initiated by a magnetic pulse.

it eventually comes to rest there, e). Once the bias field is removed the vortex is released from the defect and falls back to its original rest position at the centre of the element, f).

When testing multiple magnetic pulses in a single simulation, the second field

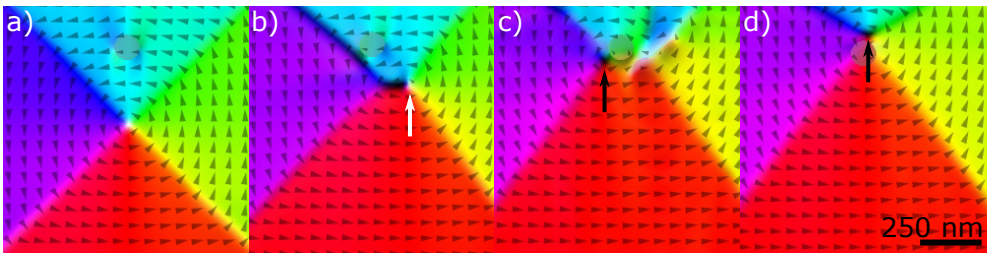

Figure 5.4: Simulation with a 100 nm diameter topological defect with vertical walls, positioned 300 nm up from the centre of the simulation. A 10 mT magnetic pulse initiates vortex gyration with a rise time of 0.8 ns. Times after gyration are a) 0 ns (before the pulse begins to rise), b) 2 ns, c) 3 ns and d) 6 ns. Arrows show the position and polarity of the vortex core.

pulse reproduced the exact same effect except that the core began gyrating in the opposite direction. This trend continued with any number of field pulses, up to 5 were triggered within a single simulation. This proved that the process is capable of reliably switching vortex core polarity from one value to the other with consecutive pulses.

However some simulations displayed a random switching of polarity that occurred before the domain walls were trapped by the defect. This was most prominent when the defect offset from the centre was large ($>$200 nm) thus requiring a stronger magnetic pulse to move the vortex core far enough to reach the defect. This random switching occurred due to the magnetic pulse increasing in strength quicker since the rise time remained the same as with the weaker fields due to matching the capabilities of the pulse generators used in experiments. Magnetic fields with a quick rise time of 200 ps also caused random polarity switching in the same manner. An example of this is shown in fig. 5.4. Note how the vortex polarity switched before any domain walls became trapped by the defect, seen most notably in frames fig. 5.4b and fig. 5.4c.

From the simulations there was no noticeable difference in the resulting outcome of polarity switching with regards to the angle of the defect walls. This was promising as it implied that the FIB milling profile should not affect the outcome of the ability of the defect to switch the vortex polarity during an experiment. Instead the switching was more dependent upon the defect depth through the Py element,

defect size, defect offset from the centre of the element and the magnetic pulse rise time. So long as the defect was at least half way through the Py element but not entirely through the structure then switching occurred.

One factor that did significantly affect results was the introduction of the 1/r reduction of magnetic field strength through the vertical dimension of the magnetic element. As explained in section 4.3 this was to more accurately simulate the experimental circumstances of vortex core gyration initiation via Oersted field generation using a CPW. Without 1/r field weakening, a magnetic pulse strength of $\geq$4.4 mT was capable of switching vortex polarity, however with 1/r weakening and all other parameters being the same, a field strength of $\geq$13 mT was necessary to achieve vortex polarity switching. As field strength increased, random switching of the vortex polarity would occur which could be negated by increasing the rise time of the magnetic pulse.

The optimal parameters for the defect used for polarity switching were found to be using a 100 nm diameter hole which was positioned 200 nm up from the centre of a 2 μm^2 element. With a smaller offset of 125 nm the defect was too close to the magnetic rest state, causing the nearby domain walls to immediately become trapped within the defect. A 300 nm offset however was too far for the vortex to reach with realistic magnetic pulse strengths and rise times. However, using a smaller defect diameter of 70 nm with vertical walls positioned at 200 nm upwards from the centre did not cause polarity switching due to it being too small to pin both domain walls simultaneously during the first gyration cycle. By the time the lower domain wall was close enough to become pinned, the upper domain wall that was already trapped had unpinned from the defect and thus no switching occurred. Interestingly though, when making the defect walls increase in size at a 40° angle, likened to what would be expected in a real-world sample, polarity switching then occurred since part of the defect was now large enough to pin both domain walls simultaneously. A pulse strength of 13 mT was able to achieve this, however 8 mT was not enough.

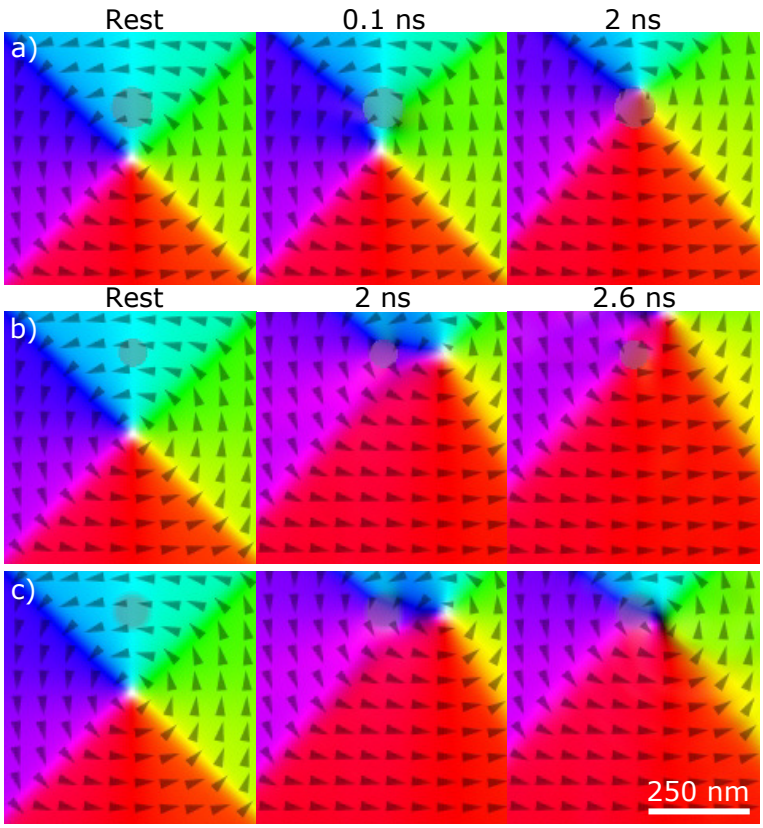

Figure 5.5: Simulated images showing the enlarged central region of various parameters of topological defect within a 2 μm magnetic square element. Defect diameters are a) 100 nm and b)-c) 70 nm, offset positions are a) 125 nm and b)-c) 200 nm, wall profiles are a)-b) vertical and c) 40°. Rest states are of the first frame before the simulation relaxes fully, hence why 0.1 ns in a) shows a different true rest state.

Figure 5.5 shows some key frames of simulations of various defect parameters. Figure 5.5a is of a 100 nm diameter defect with vertical walls positioned 125 nm away from the centre of the element and shows the trapping of the top domain walls before gyration is initiated where no polarity switch was observed. Figure 5.5b shows a 70 nm diameter defect with vertical walls positioned 200 nm up from the centre of the element. During the gyration cycle the domain walls are not trapped for long enough to switch vortex polarity, the top wall exits the defect at approximately the same time as the bottom wall becomes pinned. Conversely fig. 5.5c is of the same defect but with a 40° wall profile. Here the defect is large enough to trap both domain walls for long enough to switch vortex polarity.

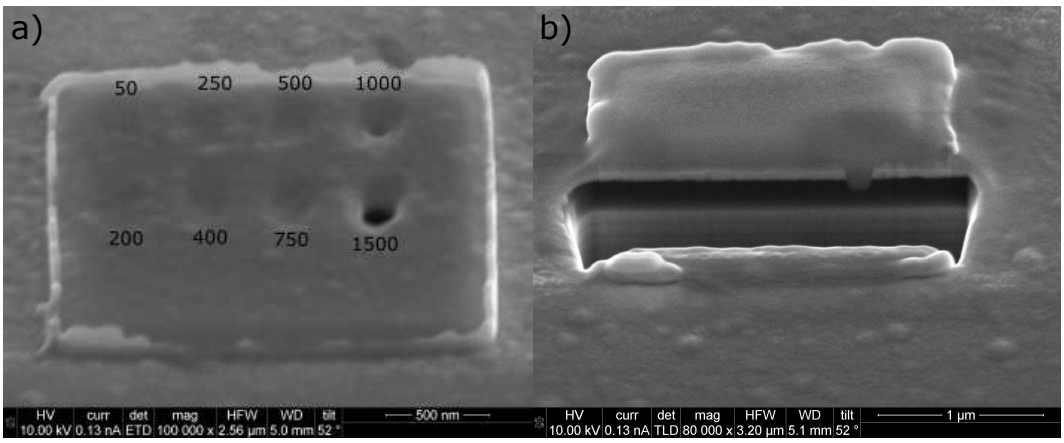

Figure 5.6: a) SEM image after defect calibrations were milled with the number of passes marked next to its respective region. 1500 passes milled through the entire thickness of the Py element, the Au CPW and some of the silicon nitride membrane whilst 1000 passes went through the Py element and somewhat through the Au CPW. b) SEM image of the cross-section of the lower row of calibrations (200, 400, 750 and 1500 passes). Pt deposition has filled the defects in order to protect the calibrations from cross-sectioning.

5.2 Methods

Samples were initially prepared via the same lithographic processes as other samples throughout this thesis, outlined in section 3.3. The additional step of defect milling will be outlined here.

Topological defects were milled using FIB by altering the number of passes made by the Ga beam for a specific voltage and current, beam pitch, beam overlap, magnification and defect diameter. The full list of FIB parameters that were used are given in appendix B.1. Calibration of hole depth was carried out using 100, 200, 250, 400, 500, 750, 1000 and 1500 passes, results of which are shown in fig. 5.6. 1500 passes milled entirely through the Py element and CPW and somewhat into the silicon nitride membrane whereas 1000 passed through the Py element and into the gold CPW but did not reach the membrane, therefore fewer than 1000 passes were required.

In order to measure defect depth a layer of platinum (Pt) was deposited across the top of the element in order to increase SEM contrast and protect the calibrations from cross-sectioning, as shown in fig. 5.6b. However the resolution of the

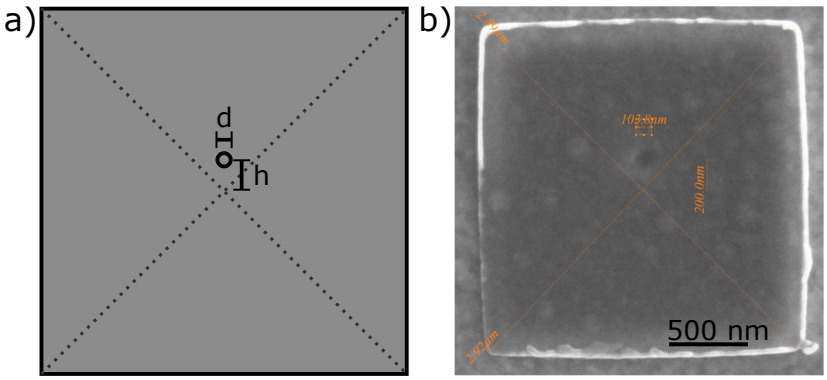

Figure 5.7: a) schematic of the position of the physical defect in relation to the centre of the Py element. Vertical displacement, h, from the centre was 200 nm whilst the diameter, d, was 100 nm. b) SEM image of an element after FIB milling of the hole. Orange dotted lines indicate the centre of the element and measurements are made to conform defect size and offset are as expected.

SEM was not sufficient to measure the depths. Figure 5.6a shows the Py element that was used to calibrate the defect milling, b) shows the cross-sectioning. 1500 passes milled through the Py element, gold CPW and into the silicon nitride membrane and 1000 passes had milled into the CPW, however it was difficult to determine which number of passes went through precisely half of the element. Due to this realisation it was decided that 500 passes should be sufficient to mill through at least half of the structure based on the results of the 1000 passes calibration.

Figure 5.7a depicts a 2 μm x 2 μm x 80 nm square Py element with a physical defect 100 nm in diameter, d, and 40 nm in depth displaced at a height of 200 nm, h, from the centre of the square. A 40 nm deep defect will induce polarity switching according to simulations.

See fig. 3.1 for a schematic of the experimental setup. The facility ran in 16-bunch mode resulting in a master clock, and thus the time between successive x-ray probe pulses, of 146 ns and a magnetic pump pulse width of 10 ns and rise time of 1 ns was used to obtain time resolution via stroboscopic pump-pulse measurements. A quadrupole permanent magnet system was present in the chamber instead of the hollow electromagnets as seen in the ESRF chamber. This led to a constant $\sim$70 Gauss bias field being applied across the sample at all times. Sample orientation within the chamber was at 45° to the x-ray beam, as with previous

experiments.

5.3 Experimental Results

We expected to observe a reversal in polarity of the magnetic vortex core when the sample was excited with a magnetic pulse however this was not observed, the possible reasons for which will be discussed in section 5.5. There was however an observation to be made on the core dynamics and size when pinned within the defect.

The quadrupole permanent magnet system was initially used to set up the magnetic ground state within the sample. It was not possible to remove this field entirely however, leaving a $\sim$70 G bias field applied across the sample. This resulted in the vortex of the ground state to be offset either upwards towards the defect of downwards away from the defect by roughly 90 nm, based on magnet orientation within the chamber. This made it difficult for the vortex to reach the defect when offset downwards or caused it to pin within the defect at rest when displaced upwards. This was likely the main reason why we did not observe vortex switching, however other causes may have been involved such as diversions of the defect parameters from those within the simulations.

Figure 5.8 shows reconstructed experimental images of the sample at rest and at specific points after gyration initiation. The top row of images, a)-c) show the vortex displaced downwards at rest and upwards for the bottom images, d)-f). There is a $\sim$50-65% enlargement of the vortex core when displaced upwards and pinned by the defect compared to being displaced downwards away from the defect. When the upwards-displaced state is pumped with a magnetic pulse the vortex gyrates around the edge of the defect and does not leave this region. A stronger pulse would be needed to force the vortex out, however this is unlikely to cause polarity switching since the process requires two unpinned domain walls to become pinned by the deformity, as shown in fig. 5.3. Conversely when the

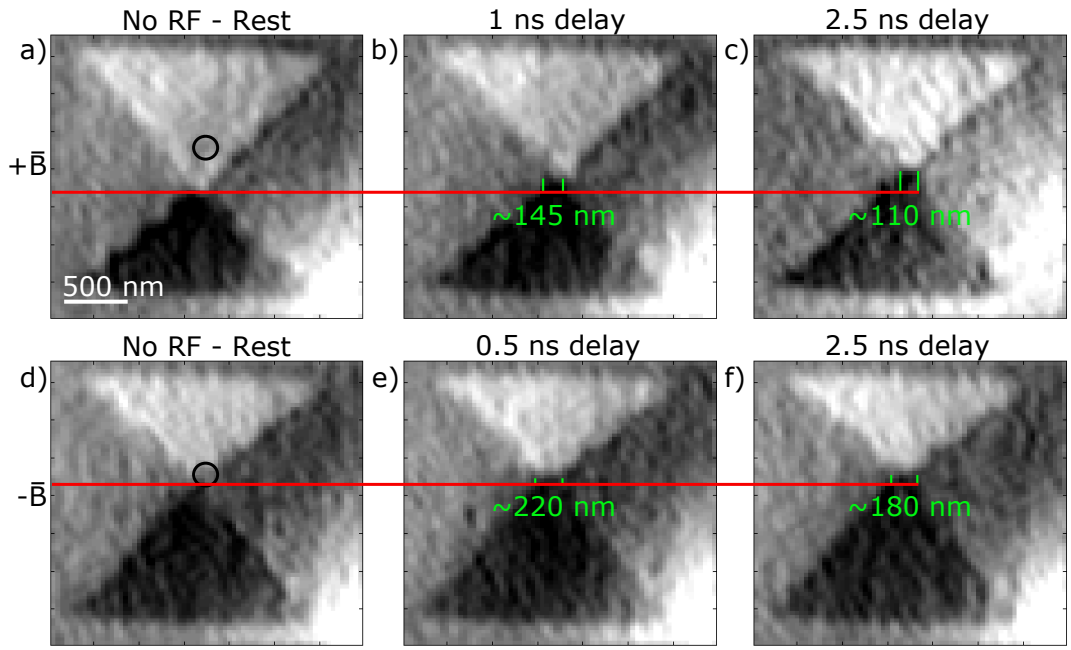

Figure 5.8: Experimental images of the magnetic state under a)-c) a positive bias field and d)-f) a negative bias field along the x-axis. The black circle marks the position of the defect whilst the red line indicates the position of the vortex at rest relative to its displacement after gyration is initiated. The widths of the vortex are indicated by the green lines. d)-f) the vortex lies within the defect when subjected to the negative bias field.

vortex was displaced away from the defect, the magnetic pulse strength used to excite vortex gyration was not large enough to let the vortex reach the defect.

5.4 Conclusion

Achieving vortex core polarity switching via the use of a topological defect would introduce a great level of control for creating a non-volatile data storage device that uses the vortex polarity as the binary state storage of bit information. It allows the potential for switching of individual vortices in an array of elements, unlike when using an alternating bias field which affects all elements of an array simultaneously, whilst also having a lower power draw than with switching via spin-polarised currents. Whilst we did not observe this effect experimentally, the simulations are consistent and imply this is still possible with Py and perhaps the observation would have been made had the 70 G bias field not been present. A topological defect does have other effects on the vortex core however, such as

the enlargement of the vortex core size when pinned within the defect.

5.5 Discussion

Although vortex core polarity switching was not observed within the experimental results there are several potential explanations for this. First and most likely is simply due to the 70 G bias field which either caused the vortex core to be offset down and away from the defect such that it could not reach the defect when gyration was initiated, or offset upwards towards the defect such that it was already pinned within it at rest before the magnetic pulse initiated gyration. Since the switching effect relies upon the defect pinning two initially unpinned domain walls during the start of the gyration cycle, it could be expected that the effect would not occur if the vortex was already pinned within the defect or could not move far enough for the domain walls to be pinned by it. This would therefore not allow the opposite polarity region to be formed and grow in order to annihilate the original vortex and form the new core with opposite polarity.

Another possible explanation is that the defect profile and geometry had diverted significantly from those of the simulated defect. It was shown in section 5.1.2 that the switching effect would occur so long as the defect depth was greater than half-way through the entire Py element thickness but less than all the way through, therefore if the defect was not deep enough through the element then this effect may not have been able to occur. Unfortunately this was very difficult to measure quantitatively due to limitations with the SEM resolution.

Additionally, since the defect was made using the Ga beam of a FIB, gallium poisoning of the magnetic material may have occurred. This would have rendered some of the remaining material under the defect to be essentially non-magnetic, however it was difficult to measure exactly how much of the material was affected and to what extent, so it may have been a negligible or significant factor. However, the fact that the vortex left the defect and fell to rest indicated that there was some

amount of magnetic material that was unaffected, since simulations with a defect that went through the entire structure (i.e. no magnetic material at all within the defect region) permanently trapped the vortex core.

Chapter 6

Coupled Vortex Dynamics

The time-resolved HERALDO results of an investigation into the coupled gyration dynamics of a pair of vortices within two physically joined Py square elements will be presented and discussed. The two square elements were fabricated at the same time, ensuring the structure was uniform thickness throughout.

6.1 Introduction

The motive behind investigating these samples was to determine whether forming a continuous magnetic film from multiple elements, each containing a discrete Landau vortex pattern, would be possible. If so then this could potentially be exploited to create a high-density array of magnetic elements for non-volatile data storage as well as investigate whether we can synchronise magnetic vortex core gyration within multiple elements and propagate a signal through the array. These are only potential applications however since such devices do not currently exist, though allusions to such a device being a possibility have been made [39].

In addition to an increase in storage density, another advantage of such an array of physically linked elements is the potential to exploit the generation of spin waves which could potentially be used to propagate a signal. Such ideas have already been explored whereby spin-waves were generated by an oscillating

magnetic vortex within a multi-layered magnetic structure [43, 136]. By creating a physically linked array of elements, the possibility for directing emitted spin-waves created by vortex oscillations throughout the array is potentially viable.

6.2 Simulations

6.2.1 Background

Numerical simulations were performed on two device geometries, from which multiple junction (overlap) sizes were investigated for their effects on ground states and gyration dynamics. Both device geometries involved forming a structure using either two 1 μm x 1 μm x 80 nm (1 μm^2) or two 2 μm x 2 μm x 80 nm (1 μm^2) square elements. The Py square elements were positioned with a corner of each overlapping the other.

Material parameters of the simulations were the same as previous samples throughout this thesis. The grid for simulating the 2 μm^2 structures was larger to accommodate the increased element sizes, though the cell size was kept the same in order to maintain consistency throughout the simulations presented in this thesis.

6.2.2 Results

Initial results obtained on 1 μm^2 elements show the ground state containing a Landau vortex closure domain within each element linked by a domain wall containing an anti-vortex (AV) at the midpoint between the vortices, as shown in fig. 6.1. A schematic comparing a magnetic vortex to an anti-vortex is shown in fig. 6.3. Upon forming the initial state vortex polarities were random though the chirality was consistent between different simulations. The primary variable between simulations was the size of the junction which was altered by moving the

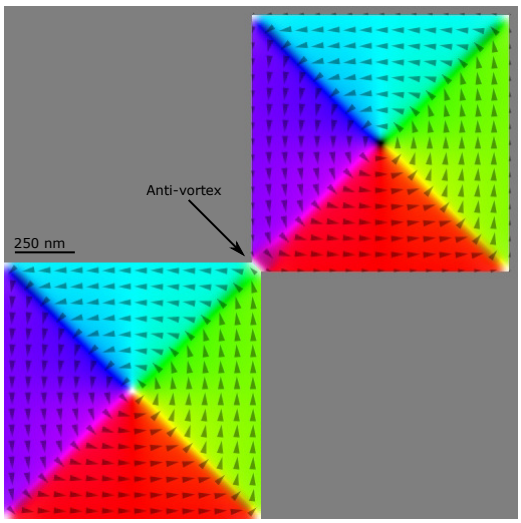

Figure 6.1: Rest state after minimisation for a pair of 1 μm Py squares with a 50 nm junction. A white AV can be seen between the corners of the junction, indicating a large positive out-of-plane magnetic component. When excited by a magnetic pulse the normal vortex cores within each element gyrate whilst the anti-vortex core is pushed into one of the corners of the junction, determined by the direction of the magnetic pulse.

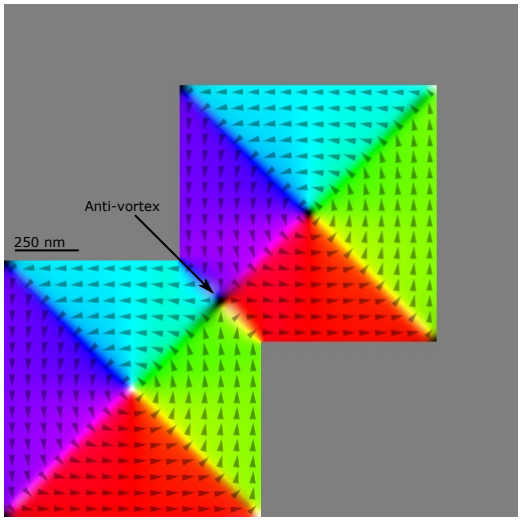

Figure 6.2: Rest state after minimisation for a pair of overlapping 1 μm Py squares with a 450 nm junction. An AV is again located between the corners of the junction but with a negative (black) out-of-plane magnetic moment. When excited by a magnetic pulse the vortices within each element began to gyrate normally along with the AV, however there exists some destructive cross-talk between the AV and regular vortices. This resulted in their gyration trajectory and frequencies being altered to the point where the vortices were not moving for up to 3 ns.

second element (top-right) closer to the first element (bottom-left). Junction sizes ranged from 50 nm to 600 nm in 50 nm steps. For clarity, a junction of 1414 nm would result in the two 1 μm square elements overlapping completely.

The interference between the vortices and the AV had a negative effect on vor-

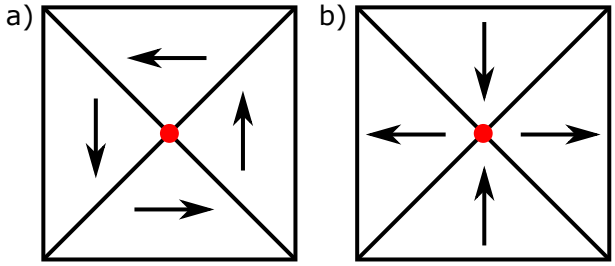

Figure 6.3: Schematic comparing the a) magnetic vortex state against the b) magnetic anti-vortex state within a square geometry. Diagonal lines represent $90°$ domain walls between adjacent domains. Red dots indicate the position of the vortex core.

tex gyration within each element, resulting in an erratic gyration path that reduced their frequency. We also confirmed experimentally that this was the rest state of the sample which naturally forms during the Py sputtering process and requires a further step to remove the AV. Upon setting the polarities of the vortices to a particular configuration by using a large out-of-plane bias field and rotating the sample such that the field was applied in plane then slowly removed, samples that had a large enough junction would lose the AV in favour of an in-plane magnetised region that spanned between the junction corners and vortices, shown in fig. 6.4. The magnetic vectors of this region were parallel to the bias field and pointed towards one of the two corners of the junction in order to conform with the chirality within the two elements. This resulted in the two elements having opposite chiralities that coalesced into a ”continuous” region which remained stable after the bias field was removed and even when a magnetic pulse was applied to initiate vortex core gyration. The gyration of the two vortex cores within this configuration was no longer disturbed by the AV, resulting in cleaner gyration cycles for the vortices.

To test the stability of this structure and gyration dynamics of the vortices a magnetic pulse was applied either parallel or anti-parallel to the magnetisation direction of this continuous, in-plane region (i.e. $135°$ or $315°$ within the simulation). The state remained stable regardless of the direction of the magnetic pulse application. With a strong enough magnetic pulse the vortices switched their polarity, the same was seen with a quick pulse rise time though this effect was seen in

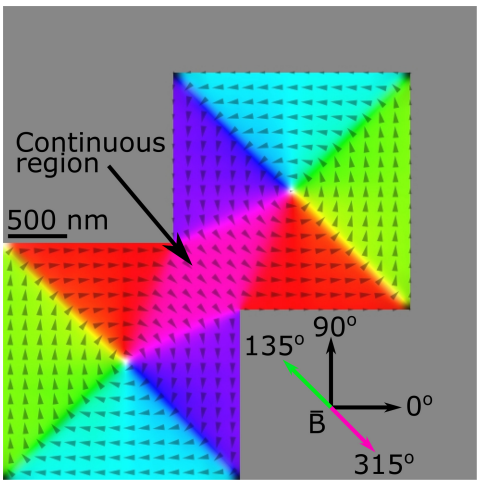

Figure 6.4: Rest state of a pair of overlapping elements with a junction width of 400 nm. The sample had been subjected to a large 600 mT bias field at $90°$ to the surface normal (out-of-plane) followed by a gradual rotation of this field to be mostly in-plane ($10°$) then slowly removed. The AV between the vortices was no longer present, instead replaced by a "continuous" in-plane magnetised region (purple) which merged the chirality of the two elements which were now in opposite directions to each other. This state was used to explore the effects of applying a magnetic pulse at $135°$ (anti-parallel) or $315°$ (parallel) to the continuous region magnetisation direction, shown in the bottom-right.

simulations of other structures too so this was expected. The $315°$ pulse resulted in a much larger and smoother gyration of both vortices which is likely attributed to the continuous region not compressing which may have lead to a higher internal magnetic energy. Figure 6.5 shows a comparison between the pulse directions and their effect on gyration amplitude.

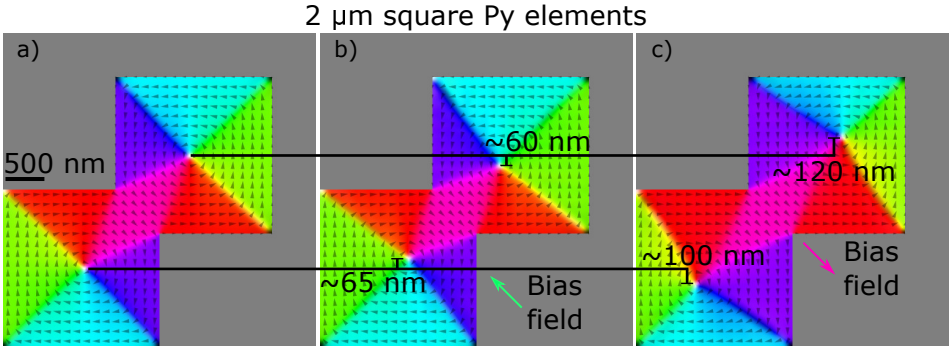

Figure 6.5: Comparison between a) the rest state and the maximum vortex core displacement from magnetic pulses in either b) $135°$ or c) $315°$. In both cases the magnitude of the pulse was 20 mT with a 200 ps rise time. Individual square elements have an edge length of 2 μm.

The emphasis on a smooth gyration was important as it indicated the presence of destructive interference and vortex polarity switching if the gyration was

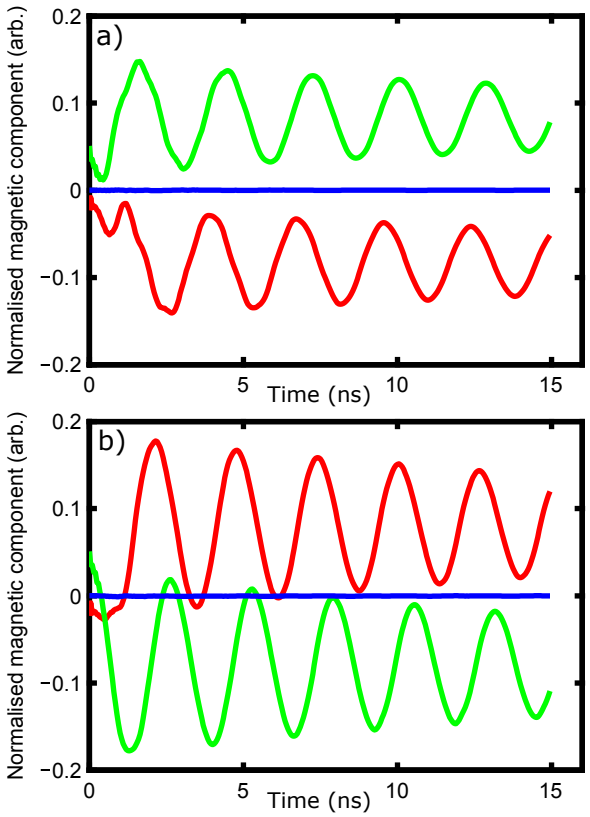

Figure 6.6: Plots of magnetic components m_x (red), m_y (green) and m_z (blue) against time for a a) $135°$ and b) $315°$ magnetic pulse. Components are normalised by MuMax such that a value of 1 or -1 represents saturation in the positive or negative direction for that dimension. In a) we observe an initial disturbance to the gyration in m_x (red) however this was not observed in b), suggesting that the there is a difference between gyration dynamics when the pulse is applied parallel or anti-parallel to the central region of the structure.

not smooth. Figure 6.6 shows a plot of the x, y and z components of overall magnetisation within the sample once a magnetic pulse had been applied (a) anti-parallel ($135°$) or (b) parallel ($315°$) to the continuous region. In the case of the anti-parallel pulse there was a noticeable disturbance in the start of gyration, particularly in the x-component (red) which was attributed to one of the vortex polarities switching. This disturbance was not seen when applying the magnetic pulse parallel at $315°$.

6.2.3 Conclusion

Simulations showed that physically linking multiple square magnetic elements by overlapping their corners could produce two magnetic ground states; the initially

formed AV state and the continuous state, with each element containing a vortex core in their centre. The AV state was the initially formed ground state whilst the continuous state only formed within samples that contained a junction size larger than 200 nm and only after the application of an external magnetic field. The next step was to fabricate a sample and observe the states experimentally.

6.3 Methods

Sample fabrication was carried out as detailed in section 3.3. Junction size was altered by changing the relative position of the two elements along the CPW to each other, see fig. 6.7. After patterning of the square elements, the sample was developed and Py sputtered such that both elements were formed simultaneously. This was done to ensure a uniform thickness of the overall structure, however it also prevented the potential formation of an oxide layer between two separately sputtered elements, which has been shown to occur passively in air within one to two weeks [137].

A total of nine junction size groups were fabricated on each CPW, ranging from 50 nm to 450 nm in 50 nm steps. However, the junction sizes turned out larger than expected, likely due to the developing time after EBL patterning being too long. Actual junction sizes ranged from 150 nm to 580 nm. This was still acceptable since the intention was to investigate the larger junctions due to these forming the more interesting continuous magnetic state instead of the less desirable AV state, based on the results of the simulations.

Structures of elements with the same junction size were made in groups of four, each spaced evenly apart along the CPW by an edge-to-edge distance equal to the total length of the long-axis of the structures in order to minimise cross-talk between the vortices during measurement. This edge-to-edge distance therefore varied based on the junction size. A group of four structures for each junction size were fabricated in order to ensure that at least one structure would be suitable

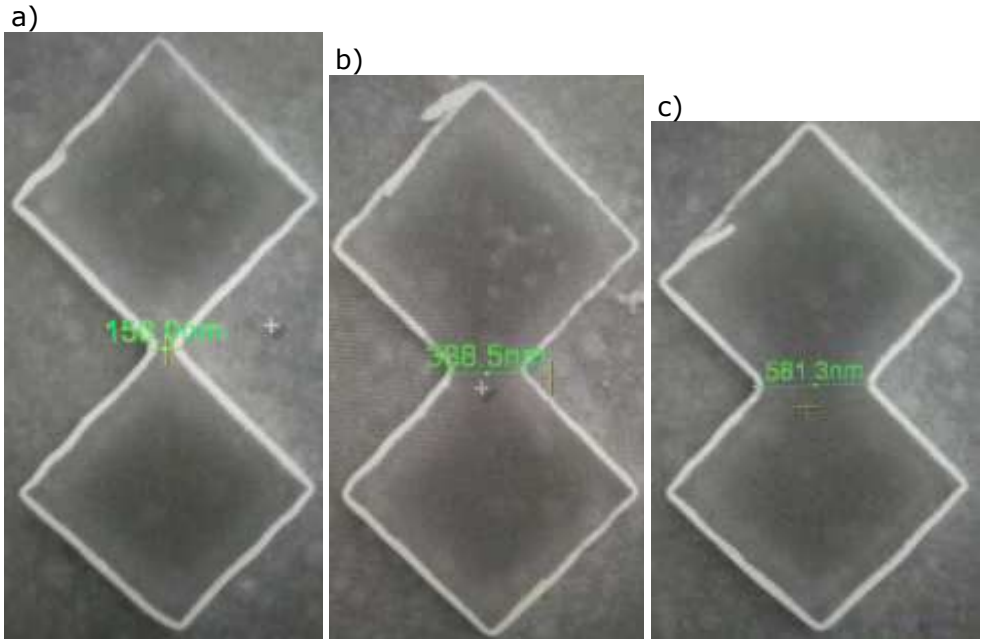

Figure 6.7: SEM images of three of the nine junction sizes fabricated using square elements of edge length 2 μm. The overlap sizes displayed are a) 150 nm, b) 390 nm and c) 580 nm, to the nearest 5 nm. Junction sizes ranged from 150 nm (smallest) to 580 nm (largest), increasing in 55 nm to 80 nm steps. Note that the individual square elements are closer together when forming a larger junction but that there is no physical overlap of the two elements since they were sputtered simultaneously.

for use since the lift-off process can often leave undesirable rough edges. The groups of different junction sizes were spaced $\sim$50 μm apart from the end of one group to the start of the next in order to ensure that the x-ray beam would not illuminate more than one device during measurement since the x-ray beam had a diameter of $\sim$50 μm.

As with previous samples, devices were made by milling apertures and reference slits with FIB as outlined in section 3.3.2. Reference slits were 60 nm wide on average. Devices were spaced $\sim$30-80 nm apart from one another based on which of the four structures was chosen from each junction size group.

6.4 Results

This section will be split into two subsections. The first will report on the experimental results obtained from two 1 μm square Py element structures performed

at the ESRF synchrotron. The second will similarly report on the results obtained from two 2 μm square Py element structures performed at the Source optimisée de lumière d'énergie intermédiaire du LURE (SOLEIL) synchrotron. Both experiments were identical in terms of data acquisition and analysis, as with previous experiments at the same facilities. The achieved spatial resolutions at both facilities were identical to previous experiments at their respective facilities due to the x-ray energy remaining at the L_3 edge for Fe (708 eV) and the distance between the sample and CCD remaining constant throughout.

6.4.1 1 μm square element structures

The first sample measured was the structure formed of two 1 μm square elements at the ID32 beamline of the ESRF, Grenoble. The facility ran in 16 bunch mode which resulted in a 176 ns delay between successive x-ray pulses. As with previous experiments the magnetic pulses used to excite vortex core gyration were triggered by the synchrotron master clock, resulting in magnetic pulses being spaced 176 ns apart from one another. This was sufficient time to allow damping of vortex precession such that subsequent excitations were not affected by previous excitation pulses. The magnetic pulse was delayed relative to the x-ray pulse in order to obtain time-resolved imaging of magnetic dynamics.

1 μm square Py element structures were the first to be fabricated due to their simpler fabrication process and allowing the use of a smaller diameter aperture hole in the mask, resulting in an improved contrast for the HERALDO holographic technique. The improved contrast results from the reduction in the number of undiffracted x-rays that do not pass through the magnetic elements that simply lead to saturation of the CCD pixels with no useful magnetic information. Figure 3.1 shows the experimental setup and the time-profile used for stroboscopic measurements on these samples. The information shown in this figure was for the first set of experiments performed on samples formed from two 1 μm square elements at the ID32 beamline at the ESRF synchrotron, however the only signif-

icant differences in sample setup compared to the SOLEIL experiment on 2 μm square elements were the presence of a dipole electromagnet (ESRF) instead of a quadrupole permanent magnet (SOLEIL) as well as a decreased time period between successive pump-probe pulses (176 ns at ESRF instead of 146 ns at SOLEIL). Samples were imaged at 45° as with previous experiments.

Experimental images of 1 μm element structures are shown in fig. 6.8 alongside preliminary simulations of the same or very similar observed state. Structures containing a junction size of 200 nm or greater were capable of containing both the AV and continuous magnetic states whereas smaller junction sizes, below 200 nm, were only capable of sustaining AV states. The continuous state was reliably able to be formed in samples with a junction larger than 200 nm after the application of a saturating in-plane magnetic field that was slowly removed. In both cases the AV state was the initial ground configuration that formed after magnetron sputtering of the permalloy. Polarities of the vortex cores were able to be controlled by introducing an out-of-plane component to the bias field by rotating the sample inside the magnetic field, forming vortices of the same polarity.

Figure 6.9 shows experimental images obtained from a structure with a 220 nm junction width. We observed that at 2 ns after sample excitation via a magnetic pulse, both vortices within the elements moved upwards to their maximum displacement position. The out-of-plane component of the vortex core is shown clearly in the imaginary part of the data, c) and d), where the orientation of out-of-plane magnetic moments are more prominent. The AV within the sample junction displaces vertically in the opposite direction due to the pattern of growth/reduction of the black/white domains respectively. The displacement of both vortices and the AV however is very small at 1-2 pixels, corresponding to a distance of $\sim$40-80 nm (based on a $\sim$40 nm/pixel vertical spatial resolution) and was not able to be accurately measured by taking a line scan through the core like in previous experiments. Therefore core tracking was not able to be reliably performed using mathematical means, however animations of the time-resolved data do show a clear oscillation. This is explained in further detail below in section 6.6.

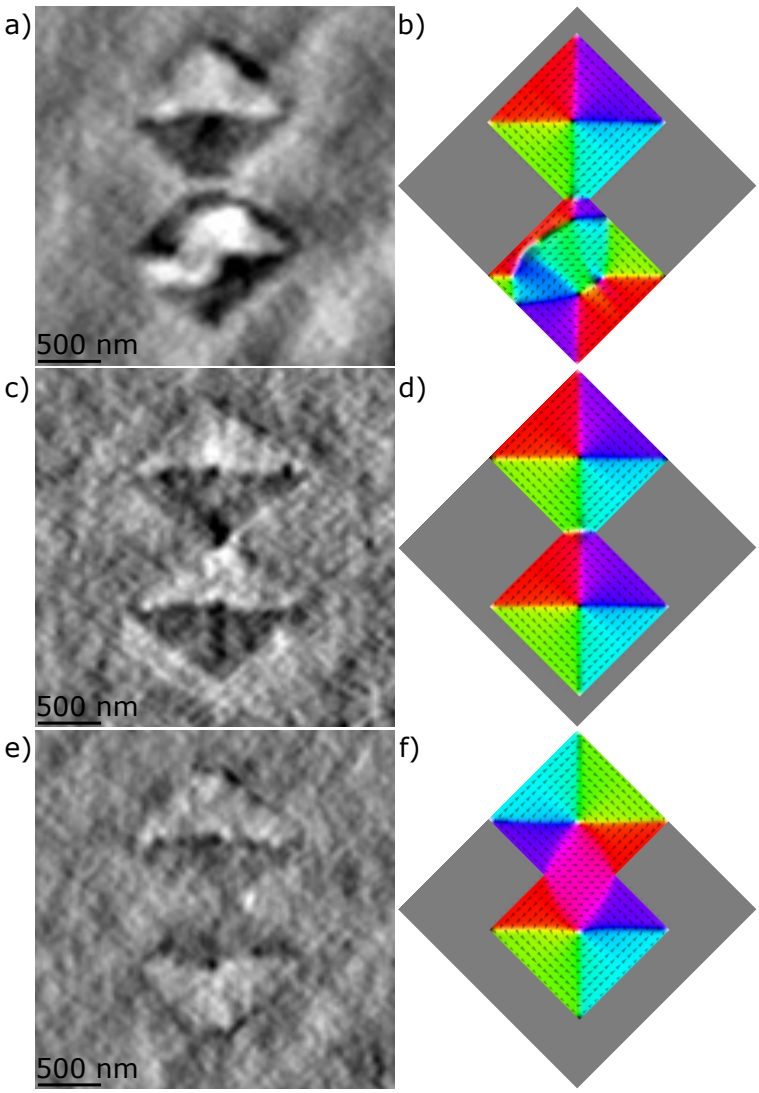

Figure 6.8: Experimental (left) and simulated (right) images of the ground states observed within overlapping structures formed from 1 μm x 1 μm x 80 nm square elements. The junction size in a) and b) is 200 nm, c) and d) is 250 nm and e) and f) is 550 nm. Examples of the AV state are shown in c) and d) whilst the continuous state can be observed in e) and f). The state observed in a) and b) is similar to the AV state however one of the two Py elements contains a complex magnetic ground state that interestingly was seen both in simulations and experimentally. Whilst the two images are not identical, the similarities are close enough and we can ultimately conclude that these samples are capable of forming stable non-Landau states involving more than 4 in-plane domains and multiple vortices in the domain walls between them in at least one of the two elements.

Images of a structure containing a junction width of 540 nm after formation of the continuous magnetic state are shown in fig. 6.10. The vortex core gyration radius is slightly larger than that of the sample with a 240 nm junction in fig. 6.9. The gyration is still very small however at 2-3 pixels, corresponding to a displacement of $\sim$80-120 nm.

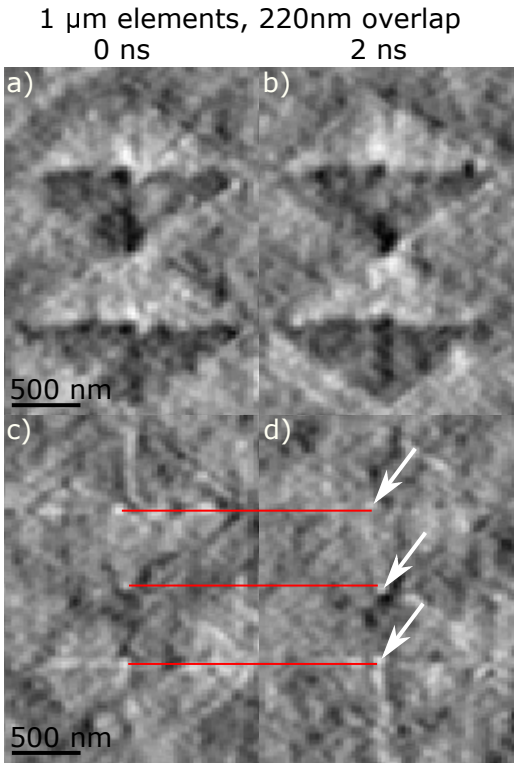

Figure 6.9: Experimental images of a 1 μm square element structure with a 220 nm junction. Top images a) and b) show the real component of the magnetic contrast after image reconstruction with MatLab for time delays of 0 ns (no magnetic pulse) and 2 ns after vortex gyration is initiated by a magnetic pulse. c) and d) show the imaginary component of these same time delays respectively. The magnetic contrast in the imaginary component more clearly shows out-of-plane magnetic moments such as the Bloch domain walls between the triangular domains and the magnetic vortex cores (white). Red lines originate from the centre of the vortices before gyration initiation (left) and serve to highlight the vertical displacement of the vortices observed at maximum displacement (right). White arrows point to the centre of the vortices after displacement by a magnetic pulse. Note the AV moved down whilst the vortices moved upwards.

6.4.2 2 μm square element structures

The second sample that was investigated contained structures formed from two 2 μm square elements and was performed at the SEXTANTS beamline of the SOLEIL synchrotron. These samples had some improvements and drawbacks compared to the previous sample. The most significant drawbacks were that the aperture had to be larger in order to accommodate for the larger magnetic structure, however the aperture diameter could not be larger than the width of the CPW core (5 μm) else the gap region between the CPW core and ground strips would be exposed to the x-ray beam. Unfortunately a 5 μm diameter aperture

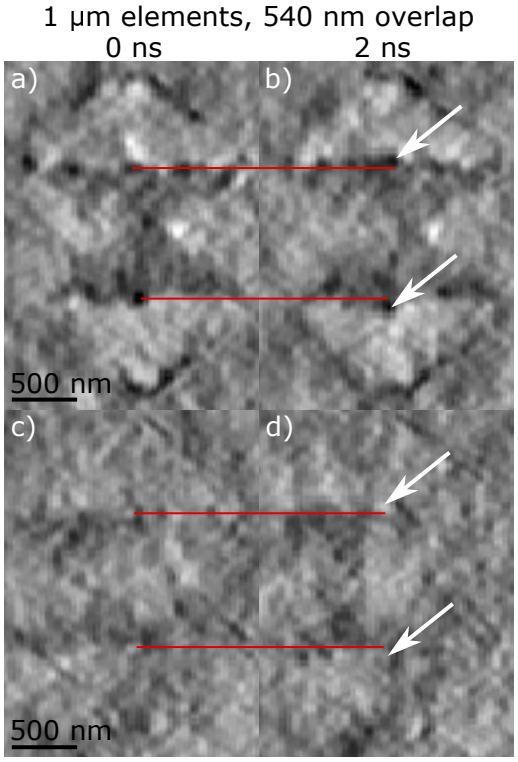

Figure 6.10: Images comparing vortex positions within a 1 μm square element structure containing a 540 nm wide junction. Red lines indicate the rest position of the vortex core at rest relative to the peak offset position after excitation, highlighted by the white arrows. Top images a) and b) are of the real magnetic component of the reconstruction whilst the bottom images c) and d) are of the imaginary magnetic component.

was not large enough to contain the entire structure, resulting in some parts of the corners of the magnetic structure being unable to be observed. Fortunately this information was not critical since the vortices in the centre of each element were where the important dynamic effects we wished to observe occurred. Conversely the most significant benefit to using larger square elements was an overall larger vortex gyration radius resulting in a much more clearly visible gyration since the HERALDO technique has a spatial resolution limit of $\sim$20-40 nm.

Figure 6.11 shows reconstructed experimental images of the 2 μm square element structures. The contrast is slightly different to those shown for the previous sample in fig. 6.8 due to the data being collected from two different beamlines, each of which have different x-ray beam characteristics and CCD's. The measured structure had a 615 nm wide junction, other sizes were available for observation however time constraints prevented us from measuring these devices. We

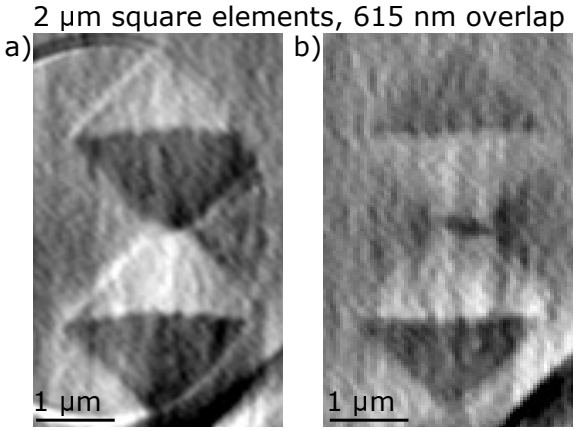

Figure 6.11: Experimental images of a two 2 μm square element structure with a 615 nm junction width. The AV state is observed in a) whilst the continuous state is observed in b). The state on the left was able to be simulated and was the initial ground state, however the state on the right could not be simulated exactly; note the black region of opposing chirality within the junction.

were able to confirm that the structure with a larger junction was still able to form the continuous magnetic state.

The core gyration paths of the 2 μm square element structures with a junction width of 615 nm are displayed in fig. 6.12 and fig. 6.13 for the AV and continuous state respectively. The gyration radii in both the AV and continuous state for these 2 μm square element structures was much larger than in the 1 μm square element structures; 300-500 nm compared to 80-120 nm. This was expected since a larger magnetic square element permits a larger range of motion due to the relatively smaller magnetostatic energy cost of the core moving towards an edge of a larger element.

From the observations in fig. 6.12 and fig. 6.13 we see that the continuous state leads to a smoother vortex gyration, of which the vortices move in opposite directions due to the opposite chiralities surrounding each vortex. Both vortices moved in a clockwise direction, implying that they had the same polarity which supports our claim that introducing a small out-of-plane component to the external magnetic field leads to the formation of vortices with the same polarity. Gyration radii of the vortices in fig. 6.12 are much larger than those observed in fig. 6.13, however the path is more erratic in the AV state.

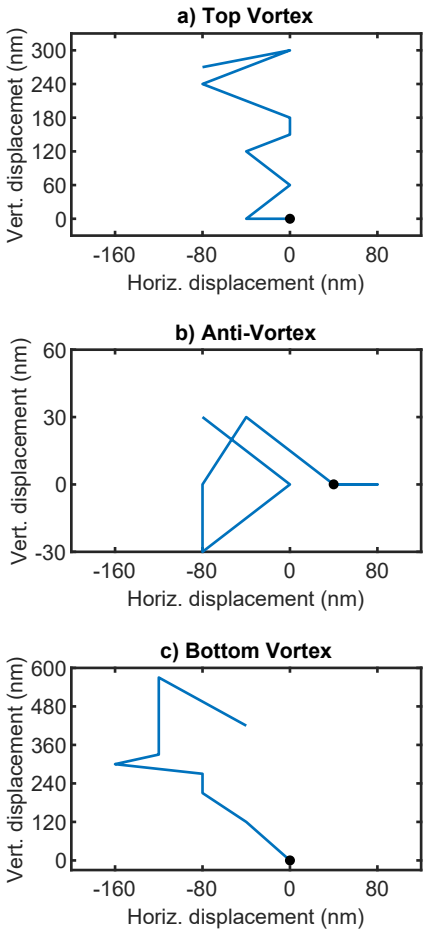

Figure 6.12: Plots of vortex core position for the a) top vortex, b) AV and c) bottom vortex for the AV state within a 2 μm square element structure containing a 615 nm junction. Axes plot the horizontal (x) and vertical (y) displacements in nm based on the most intense pixel within the imaginary component of the magnetic reconstructed data. Black dots highlight the starting point of the vortex before gyration was initiated with a magnetic pulse. All image axes have the same relative ”zero” point for the horizontal displacement, note that the AV is at rest to the right of the vortices and moves right then left after excitement.

It was not possible to draw a definitive conclusion as to why the AV state lead to a larger gyration since the quality of the reconstructed data in the AV state degraded progressively over time during measuring.

There was also an anomaly within the continuously magnetised state of the structure. The region between the points of the junction contained a magnetic domain that had an opposite chirality to that of the two individual elements. This region is clearly visible in fig. 6.11b as the dark region in the centre of the junction between the elements. This state was not able to be reconstructed in simulations so the exact effect this had upon the vortex core gyration dynamics is not yet

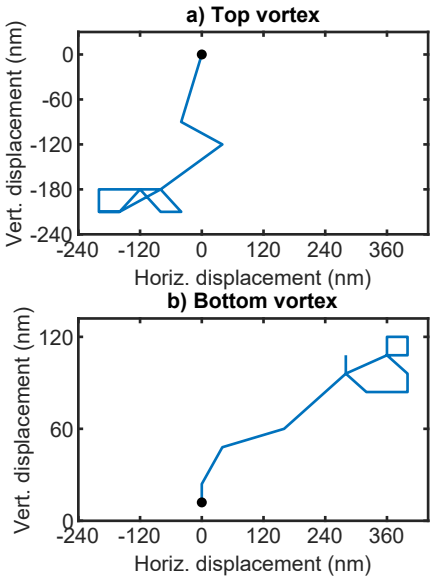

Figure 6.13: Plots of vortex core position for the a) top vortex and b) bottom vortex for the continuous state within a 2 μm square element structure containing a 615 nm junction. Axes represent the horizontal (x) and vertical (y) displacements in nm based on the most intense pixel within the imaginary magnetic reconstructed data. Black dots highlight the starting point of the vortex before gyration was initiated with a magnetic pulse. Both image axes have the same relative "zero" point for the horizontal displacement.

fully known, however the state could have been stabilised by the $\sim$70 G bias field that was present across the sample from the quadrupole magnet system in the SOLEIL sample chamber.

6.5 Conclusion

We observed a good agreement between the experimental results shown in section 6.4 and the simulations discussed in section 6.2. Vortex core gyration within the AV state of a 1 μm square element structure was disturbed, with the gyration radius being smaller than in the continuous state. Conversely the continuous state exhibited a normal gyration of each of the vortices with gyration radii comparable to those seen in previous experiments on a single Py element.

The opposite was observed in 2 μm square element structures, where the vortices within the AV state had a larger gyration radius than those in the continuous state. The smoothness of gyration of the continuous state was better than the

AV state however, similarly to that seen in 1 μm square element structures. This could be caused by the region of opposite polarity that was present between the junction points in the 2 μm square element structures, however this must be examined further.

The continuous state seemed to be very stable in samples with a junction width greater than 200 nm since it remained as the ground state even after excitation with a magnetic pulse by the CPW. This is ideal since the continuous state results in smoother vortex core gyrations and allows for elements to be closer together, creating a more dense array of magnetic square elements. However an anomaly exists between the experimental results for the 615 nm wide junction and the simulations of this state in 2 μm square element structures. The formation of the opposite chirality domain between the points of the junction was not able to be formed and remain stable after minimisation of the energy in simulations, instead it would always collapse back to the continuous state.

6.6 Discussion

Whilst the majority of the data agrees with the simulations, the experimental data of large junctions for 2 μm square element structures containing a continuous magnetic state with the opposite chirality domain in the junction were not able to be recreated in simulations. This could possibly be due to the constant 70 G bias field present within the chamber at the SOLEIL synchrotron since the permanent magnet system could not be removed entirely from affecting the sample. This bias field could have assisted in stabilising such a domain and preventing the magnetic structure from collapsing entirely into the regular continuous state observed within other samples. Further investigation must be performed in order to draw a definitive conclusion to this anomaly.

Core position tracking of the experimental data was difficult to perform mathematically using MatLab, especially in the smaller 1 μm square element structures.

This was because the most intense pixel is chosen for the position of the core, however since the core is roughly a 2x2 region within the data, slight variations often only ± 5 between values of 1000-1500 can cause the vortex to appear to move in a different direction to what is expected. This is likely a combination of random chance (since the variation is so small) and too low a pixel density within the CCD. This could be improved upon by using a better CCD with a more dense pixel array. Animations of the time-resolved data did clearly show an expected gyration pattern however.

Chapter 7

Double Landau and Distorted Vortex Under Bias Field

Results regarding observations on the field-dependent production of the double-Landau magnetic ground state within square Py elements and the distortion of a regular Landau vortex core when subjected to an external bias field will be presented and discussed here.

7.1 Introduction

The initial motivation behind the experiment was to determine whether vortex gyration would behave differently when offset to a non-equilibrium rest position by use of an external bias field. Additionally we observed the formation of a double-Landau domain pattern which is rarely seen in square magnetic structures since it is less stable than the regular Landau domain pattern. The vortex core was also observed distorting into an extended structure when subjected to an in-plane magnetic bias field which has been attributed to the relatively large thickness of the magnetic element (80 nm). We also observed time-resolved gyration dynamics of this distorted state which displayed an unexpected asynchronous gyration between the two ends of the distorted region.

The double-Landau state has been studied extensively within nanoscale rectangular elements [138, 139, 140] but less so in square elements due to the difficulty with its formation and metastability within such a geometry. Vortices in double-Landau states of rectangular magnetic elements reportedly form a vortex-antivortex-vortex state for both vortices when excited by a quick (1 ns) magnetic pulse [140]. It has also been shown that within rectangular elements it is possible to switch from the double-Landau to the regular Landau state by application of a switching bias field [138]. According to a paper by Lau et. Al. this state can be produced somewhat reliably in a square element so long as the bias field is slowly stepped down to zero Gauss from saturation [141]. It is the slow reduction in field strength that allows the second vortex to form at the sample edge before one of the two extraneous walls are expelled from the sample which would otherwise result in a collapse to the regular Landau state. The slower the external magnetic field strength is reduced, the less likely one of the two domain walls will exit the structure, forming a stable double-Landau state within a square element. The double-Landau state is significantly more stable within rectangular elements due to the aspect ratio giving the vortices more room to move apart in order to reduce their energy of interaction.

In addition to the double-Landau state, we observed a distorted magnetic vortex state that can only form within thick ($>$50 nm) magnetic elements. This state is not producible within thin magnetic samples due to the great increase in surface charge this would induce, explained in section 2.1.5. However with thicker samples the increase in surface-volume charge is small enough to counteract the large increase in magnetostatic energy caused by the external magnetic field, that the core deforms into a wide region of out-of-plane magnetic moments. This out-of-plane magnetised region has a somewhat complex structure that appears to contain two vortex cores; one at each end of the distorted region. The dynamics of the distorted vortex are interesting as both ends gyrate independently of each other.

7.2 Results

This experiment was performed at the ESRF on beamline ID32 and utilised the in-chamber electromagnet system as shown in fig. 3.1. The electromagnets had a fixed position along the path of the x-ray beam, allowing a positive or negative bias field to be applied to the sample at the same angle of incidence as the x-ray beam. Imaging was performed at 45° to obtain in-plane magnetic contrast, thus the external bias field was applied to the sample at this angle due to the position of the electromagnet poles being fixed.

7.2.1 Double-Landau Structure

Field-dependent measurements were performed by applying a bias field with a pair of electromagnetic coils on either side of the sample, as shown in fig. 3.1. Figure 7.1 shows the reconstructed images of the magnetic contrast within the sample under an increasing bias field strength which was brought to saturation and then slowly reduced to zero Gauss. The initial state shown in fig. 7.1a was formed by saturating the field in the negative direction (-5000 G) then slowly increasing to -90 G. The regular Landau pattern in fig. 7.1b was subsequently formed from the collapse of the double Landau state by increasing the bias field from -90 G to 0 G. The vortex core began moving upwards as the bias field was increased in the positive direction in a step-like manner until saturation (+5000 G). Field strength was then slowly reduced back to zero as shown in fig. 7.1c where the double-Landau state can be seen reforming.

By comparing fig. 7.1a and the last image of fig. 7.1c, the chirality of the double-Landau state has switched, suggesting a dependence of the chirality on the direction of the saturating bias field. This was expected since the field has both an x and z component whilst the sample is at a 45° angle to the bias field. The collapse of the double Landau state into the regular Landau state was likely caused by one of the extraneous domain walls being expelled from the sample

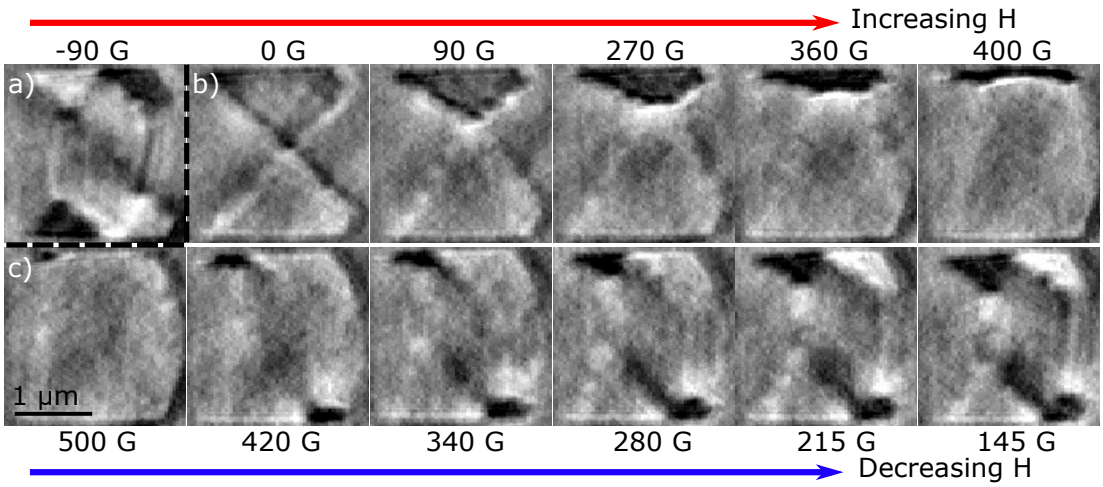

Figure 7.1: Reconstructed field-dependent images of the internal magnetic state of the sample. a) Initial state after saturating with a negative bias field and reducing the field to -90 G. b) Bias field increased to zero Gauss, collapsing the double-Landau state to the regular Landau state. The vortex core moved upwards as bias field strength increased. At 270 G we observed the vortex core begin to distort until 400 G where the sample is almost saturated. The bias field was then saturated in the positive direction and subsequently reduced to c) 500 G. A gradual formation of the double-Landau domain state was then observed as the field was slowly reduced. This process was repeated several times and always formed the double-Landau state, proving a reliable reproducibility. The double Landau state contains 2 vortices with chirality dependent upon the direction of the saturating bias field.

once the bias field approached 0 G too quickly, as outlined in [141].

As previously mentioned in section 7.1, based on the work published in [141], a slow reduction in bias field can somewhat reliably produce double-Landau structures within nanoscale thin-film Py squares. The detailed theory behind the production of the double Landau state is explained within the publication, however a brief summary would state that as the bias field strength falls below the samples saturation magnetisation, the demagnetising field begins to reduce the samples internal magnetic energy by forming domains. One vortex core is initially formed on the top edge from the c-state the sample exhibits when saturated, along with an extraneous domain wall. A second vortex then formed along the bottom edge since the first extraneous domain wall was not ejected from the structure. The first wall may be ejected from the structure if the bias field is removed too quickly [141]. For our investigation the bias field was reduced in a step-wise manner to the stated values and imaged as shown in fig. 7.1, and although our field is

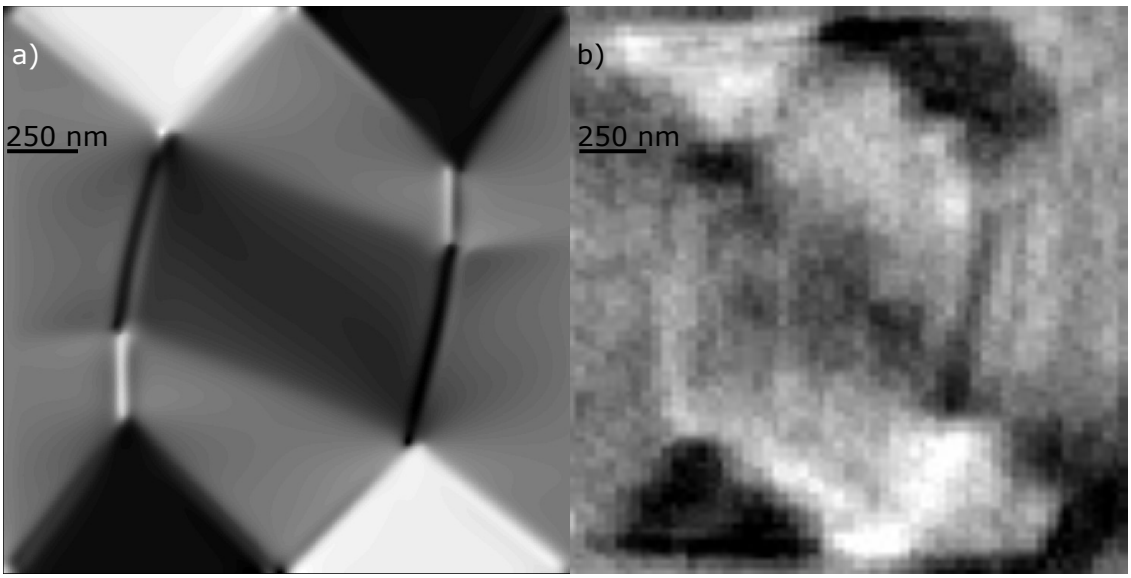

Figure 7.2: a) Simulated and b) experimental magnetic structure of the double Landau state with a -90 G bias field present. In both images the contrast represents a combination of both in-plane and out-of-plane magnetisation due to the off-axis imaging. The top-right and bottom-right corners of the domains on the right side in b) are cut out because of an overlap of the aperture hole with the sample due to imaging at a 45° angle.

stepped in relatively large increments compared to the results in the publication it did not seem to affect the ability for the sample to form the double Landau state. The process was repeated multiple times, each resulting in a double Landau state. We assume this was due to the speed of the electromagnet ramping down being sufficiently slow as to not collapse the double Landau state by ejecting one of the domain walls and its associated vortex core.

Figure 7.2 shows a comparison between the simulated and experimentally observed double Landau state when under a -90 G bias field. The two states share many similar features such as the curvature of the extraneous domain walls, the position of the vortices and the sizes and contrast of domains. Unfortunately, attempting to perform time-resolved pump-probe measurements on this state caused it to collapse to the regular Landau state so dynamics of the double Landau state were not able to be investigated. This is likely due to the remanent magnetic field from the electromagnet not being removed with a high enough degree of accuracy since this state is very sensitive to exsternal fields due to its relatively high energy compared to the regular Landau state.

From the structures shown in fig. 7.2 we can see the curved extraneous domain walls that extend between two vertically-opposite triangular magnetic domains of opposite colour. There are two of these domain walls, one for each of the vortices which are located at the tip of the top-left white domain and the same tip of the bottom-right white domains. Both vortices in the simulation were white, indicating that their polarity favours aligning with the bias field upon their nucleation, lowering the Zeeman energy associated with their interaction, as opposed to forming opposite chiralities and the lower magnetostatic energy that results from this configuration. This may explain why the structure was somewhat unstable once the magnetic field was removed since the stray fields from the vortices would interact with and repel each other, causing the double Landau structure to collapse into a regular Landau domain pattern. However, as mentioned above, the instability could have simply been caused by the remanent magnetic field of the electromagnet combined with too strong a magnetic pump pulse.

7.2.2 Distorted Vortex Dynamics with RF and Bias Field

Time-resolved measurements were carried out in the pulsed stroboscopic regime as shown in fig. 3.1. The facility was running in 16-bunch mode which produced a 176 ns period between successive x-ray probe pulses, resulting in a 176 ns period between magnetic pump pulses used to excite vortex core gyration dynamics. Figure 7.3 shows the experimental time-resolved images of vortex dynamics at various delay times for each of the bias field strengths used: a) 300 G, b) 260 G and c) 90 G. As bias field strength increased, the magnetic vortex core shifted further upwards and distorted to resemble a domain wall. This was particularly noticeable with the 300 G bias field as the top black domain had a relatively flat bottom edge and was thus no longer triangular in shape.

In fig. 7.3c (90 G) we observed a regular vortex gyration which implies that the bias field did not significantly affect the structure or dynamics, however in b) (260 G) we observed the vortex begin to distort into an elongated structure which

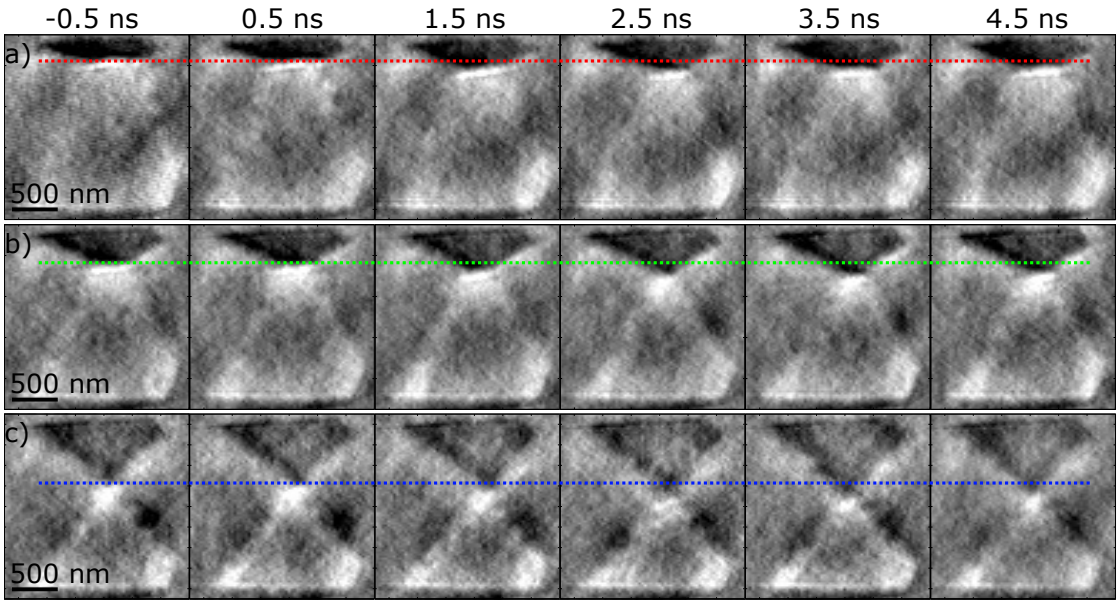

Figure 7.3: Time-resolved images of vortex dynamics under different bias field strengths of a) 300 G, b) 260 G and c) 90 G. Dotted lines act as a guide-to-eye in order to aid in observing the vortex displacement during gyration relative to the rest state in the far-left images before the magnetic pulse excites gyration (-0.5 ns).

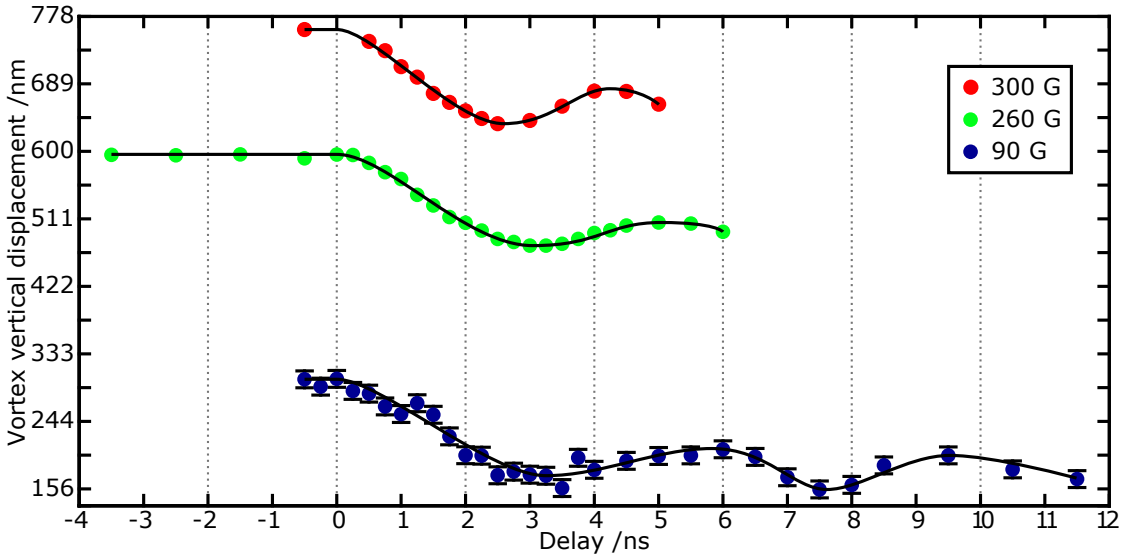

Figure 7.4: A plot of time-resolved vortex core vertical offset positions for each bias field strength. Black lines serve as a guide-to-eye. The error bars on the 260 G and 300 G are not visible due to the reduced error resulting from the greatly increased contrast of the data.

was even further pronounced in a) (300 G). In this state the vortex gyrated at an increased frequency and the radius of gyration was smaller than for the weaker bias fields, shown in fig. 7.4. This distorted structure in c) also contained a bright white region immediately below the black domain, indicating opposite out-of-plane polarised regions on either side of the distorted vortex.

Figure 7.4 is a plot of all data points gathered for each bias field at each delay time and their relative vertical displacement from the samples rest state. At least a single damped oscillation was observed in each case. As the applied bias field strength was increased the vortex gyration period decreased from 6 ns to 5 ns to 4.25 ns for 90 G, 260 G and 300 G respectively.

Beyond a critical field strength, and thus vertical displacement from its rest position, the vortex core distorted by stretching horizontally, leading to an asynchronous gyration between both ends of the distorted region once excited with a magnetic pulse. This asymmetrical motion is defined by having one end of the region move downwards before the other, as shown in fig. 7.5. The two ends also moved towards and then away from one another, resulting from them moving closer to the critical offset distance that the region began distorting at. If they had moved down past this critical region they would likely have reformed a single non-distorted vortex core. To further investigate this effect we measured the vertical and horizontal displacement of both ends of the stretched vortex at each point in time for each magnetic pulse delay time. Figure 7.5 shows this plot and the clear asymmetry between the gyration of the two ends. One side of the extended structure starts higher than the other at rest, possibly due to the fact that the sample was at a slight angle within the chamber.

Mr. C. McKeever ran some more specific simulations, after which it became clear that this structure is indeed entirely composed of out-of-plane magnetic moments, however the two ends of this region have particularly strong out-of-plane moments, akin to vortex cores, one located towards the top and and one to the bottom layer of the element. This could explain the asynchronous nature between the oscillation of the two ends of this region since they are separated by a distance large enough to affect the strength of the magnetic field that excites them. Between these two ”vortices” is a similarly out-of-plane magnetised region that extends between them, though to a lesser magnitude. A visual representation of this structure is displayed in fig. 7.6.

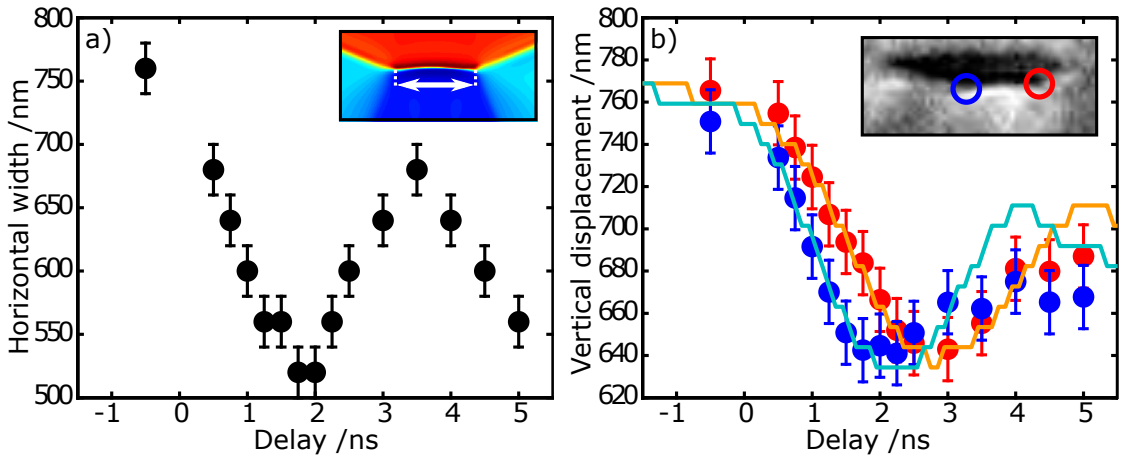

Figure 7.5: Comparison of a) horizontal and b) vertical displacements of the two ends of the distorted region. a) the horizontal width between the ends of the region shows a clear oscillation between them. The ends start at 750 nm apart then move to 520 nm then begin oscillating within this range. Inset shows an image of the simulated state with the white arrow indicating the measurement of the horizontal displacement. b) compares the vertical displacements of the two ends of this region. Red and blue points represent experimental data for the right and left ends respectively whilst the orange and cyan lines represent the simulated data for this state for the right and left ends respectively. Inset shows this visually for clarity.

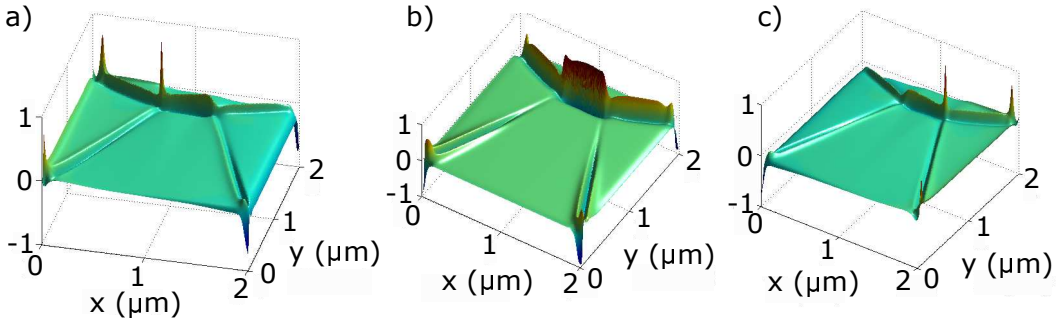

Figure 7.6: Simulated images of the rest state of an 80 nm thick square Py element. Images correspond to different layers within a 16-layer tall simulation: a) the bottom 1st layer, b) the central 8th layer and c) the top 16th layer. Each layer represents 5 nm of magnetic material. Colour corresponds to the magnitude of the out-of-plane magnetic component, m_z, ranging from dark blue (-1) to green (0) to dark red (+1), positive represents vectors in the upwards direction. Images courtesy of Mr. C McKeever.

Note that the distorted region in fig. 7.6 is formed from parallel regions of upwards (red) and downwards (blue) magnetic moments (downwards moments not clearly visible due to the image orientation). This agrees with experimental observations since the distorted region was composed of a bright white region parallel to a dark black region. Individual vortex cores however were not particularly visible in the experimental data, likely caused by an averaging out of the magnetic

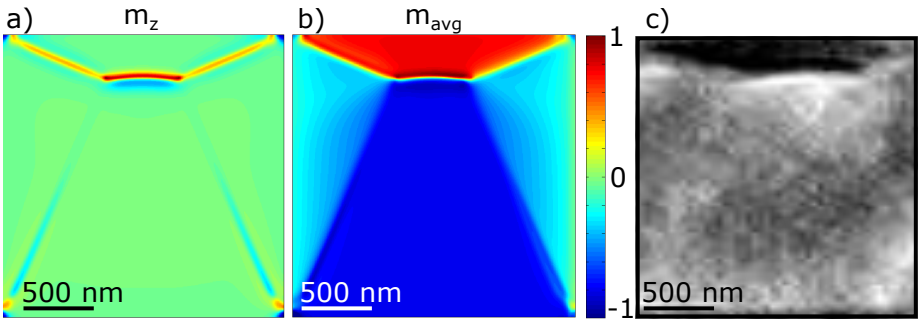

Figure 7.7: Comparison between simulated images of a) m_z, b) m_{avg} and c) experimental images of the distorted vortex state. The averaged state observed in b) shows emulates the magnetic state that is measured by the CCD when the sample is at a 45° angle to the incoming x-ray beam, shown in c). Colour bar represents the magnitude of simulated magnetic vectors, with red (+1) and blue (-1) corresponding to an a) upwards or downwards out-of-plane polarity and b) combined right and upwards or left and downwards combined x and z magnetic vectors respectively. A 200 G magnetic field is present within the simulations whilst the experimental image has a 300 G magnetic field. Simulations were performed by Mr. C. McKeever.

moments throughout the entire thickness of the structure. A comparison between the experimentally observed ground state and a comparable simulated state is shown in fig. 7.7. The simulated state was performed with an averaging step that aimed to emulate the experimentally observed system such that the simulation shows what is observed by the CCD when the sample was rotated to 45° relative to the x-ray propagation direction.

Comparing the distorted regions in fig. 7.7 they appear curved and contain intensely magnetised regions above and below denoted by the dark blue and dark red in the simulations, a) and b), and by the bright white and dark black in the experimental image c). Unlike in fig. 7.6 however, the vortices at the ends of the region are once again indistinguishable, likely resulting from the aforementioned averaging of the observed magnetic moments throughout the thickness of the sample. The distorted region in fig. 7.7c is higher up and wider than that seen in fig. 7.7a) and b) due to the difference in magnetic field strength present, with the experimental image having a 300 G bias field and the simulation having a 200 G bias field. This vortex distortion effect is only observed within samples thicker than at least 20 nm, as shown in fig. 7.8a.

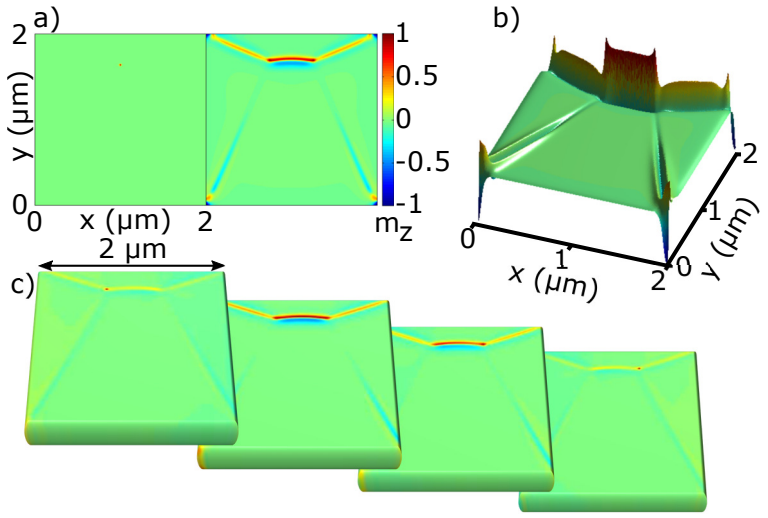

Figure 7.8: Simulated images of a 2 μm square Py element under a 300 G bias field. a) out-of-plane magnetic moments, m_z, within a 20 nm thick element (left) and an 80 nm thick element (right). b) 3D plot of out-of-plane magnetic moments averaged through the entire thickness of the element. c) a series of images of the out-of-plane magnetic vectors within various vertical layers of the simulation. The layers are, in order of left to right, the first layer (bottom), eighth layer (middle), twelfth layer (middle-top) and sixteenth layer (top) out of a total of sixteen layers. This shows the existence of two vortex cores, at opposite ends of the distorted region that exist in opposite vertical layers to one another.

7.3 Conclusions

In summary we observed the reproducible field-dependent production of the double Landau state within a nanoscale Py square element as well as the time-resolved dynamics of a magnetic vortex whilst under the application of an external magnetic field by utilising the x-ray holography technique HERALDO. Micromagnetic simulations have confirmed the measured structure as being a double Landau state with seven domains and two vortices, including similarities between the contrast of domain walls and domain regions.

We also observed that the deformed vortex state shows a lateral distortion of the region when under a relatively high bias field. The ends of this distorted region form distinct vortices; one side forms at the bottom of the element whilst the other side forms at the top of the element. Once the sample was excited with a magnetic pulse the vortices oscillate out-of-phase with one another, moving closer together or further apart based on the direction of the magnetic pulse. The

vortices also gyrate vertically out-of-phase with one another, with one vortex moving up or down at a slight delay to the other, though both oscillate at roughly the same frequency. This was demonstrated in both the simulated and experimental cases and they have a good agreement with one another. The asynchronous gyration behaviour observed with the distorted vortex state was likely due to vortices being separated on opposite ends of the vertical planes of the sample. Since one vortex forms at the bottom of the element and the other forms at the top of the element, the vortex at the top received a weaker magnetic excitation pulse due to its reduced proximity to the CPW which produced the magnetic pulse. This would explain why its motion is delayed compared to the vortex located at the bottom of the element that is in direct contact with the CPW and thus received the full strength of the magnetic pulse.

7.4 Discussion

Unfortunately the double Landau state was not stable enough to perform time-dependent vortex excitation measurements on, however the simulations show that it should be possible to investigate. This was likely caused by the vortices being of the same polarity and thus being more unstable than if they were of opposite polarities due to the repelling interactions of their stray fields.

Simulations of distortion of the vortex core was observed within an 80 nm Py element but not within a 20 nm thick element. The critical thickness for this effect is likely around $\sim$50 nm since this is the threshold that beyond which Bloch walls begin to form in thicker samples whilst Néel walls exist within thinner samples, as discussed in section 2.1.5. However, further investigation involving simulations of different sample thickness must be performed before drawing this conclusion. It can however be hypothesised that a thicker sample could lead to quicker distortion of the vortex core, one that begins distorting at lower external field strength values and thus closer to the vortex cores' rest position.

Chapter 8

Future Work and Conclusions

Throughout this thesis we have observed various dynamic effects occur within different geometries of nanoscale Py elements. In particular it was found that square geometries harbour, in theory, out-of-plane magnetic singularities at each corner which can be switched in polarity by bullet-like propagations that run along the domain walls within the Landau structure after excitation by an external magnetic pulse. This could have significant practical applications in the design of a non-volatile magnetic storage device as additional modes of binary data storage. Thick magnetic elements also showed a complex internal magnetic structure, especially when exposed to an external bias field. The vortex core was observed to distort into an extended structure composed of out-of-plane magnetic moments that changed throughout the height of the element. Understanding these phenomena will allow a greater knowledge of how magnetism behaves when confined to the nanoscale.

Forming a larger magnetic structure from multiple square magnetic elements showed two possible ground states based on sample geometry and magnetic history. The initial ground state contains a Landau structure with a magnetic vortex within each element joined by a domain wall harbouring an AV at its mid-point. If the individual elements were fabricated close together to form a large overlap ($>$200 nm) then a saturating in-plane bias field can be applied and removed in or-

der to form a ”continuous” state where the domain wall and AV are now replaced by an in-plane magnetised region that links the opposite chiralities of the Landau structures within the two elements. This continuous state resulted in a cleaner vortex gyration due to the removal of the AV which disturbed the gyration of the vortices and thus has potential to allow creation of a large array of vortices with synchronised vortex gyration upon excitation with an external magnetic field. This effect has potential applications in signal propagation. Additionally the creation of such an array could benefit the fabrication of a non-volatile magnetic storage device by increasing the storage density by allowing individual vortex cores to be closer in proximity to one another without the negative interaction of their stray-fields influencing vortex gyration.

Vortex core polarity switching has previously been reported being possible via multiple methods, however here we have shown that a topological structure within the surface of the magnetic element is capable of switching vortex polarity. This could be exploited in controlling vortex polarity within an array of elements for a non-volatile magnetic storage device, however it is also important to know that if an element has such a topological structure within its geometry that it can affect vortex polarity in such a drastic way. The effect has yet to be proven experimentally, however we did observe that such a topological structure increased the size of the vortex core and affected its gyration dynamics. Polarity switching via a topological defect will be investigated further at a facility with no remanent bias field affecting the samples ground state as this was likely the explanation as to why switching was not observed.

Further investigation into the multiple-element structures would involve the imaging of the dynamics within square elements that do not lay directly on the CPW that generates the magnetic excitation field. In order to correctly judge the capability of such a geometry to propagate a magnetic signal we must first observe how far such a propagation can move before sufficient damping has occurred. Therefore new samples must be fabricated wherein a single element lies along the CPW and various lengths of arrays are made where all other elements

are not in direct proximity of the CPW. The objective and reference will be located on the last element in order to observe if a significant gyration is still observed.

Additionally the gyration dynamics of the double Landau state within nanoscale magnetic square elements should be further investigated experimentally. Numerical simulations show that this state is stable enough to apply external excitation fields to initiate vortex core gyration without the state collapsing to the regular Landau state. Complications arose due to the remanent field within the electromagnet used to create the double Landau state, however with a fine calibration of the field created by the electromagnet should allow for the stable formation of the double Landau state.

Appendix A

MuMax Simulation Script

Below is a copy of a script used to simulate 2 μm x 2 μm x 80 nm square element with Py material parameters (”msat”, ”aex” and ”alpha”) within a 512 x 512 x 16 grid. Each cell in this grid represents 3.90625 nm in the x and y dimensions and 5 nm in the z dimension. All size and time values are in metres or seconds respectively, therefore ”e-9” and ”e-12” are used to represent nano and pico prefixes respectively.

In this particular simulation script there are three magnetic pulses, represented by (DELAYA, DELAYB and DELAYC, WIDTH1, WIDTH2 and WIDTH3 etc.) however the latter two start after the simulation has finished so are essentially unused. The first magnetic pulse has a delay, ”DELAYA” of 50 ps relative to the simulation start, a width, ”WIDTH1”, of 10 ns, amplitude, ”AMP1”, of 8 mT (0.008 T), rise time, ”RISE”, of 1 ns and is applied at an angle of 0° in the x, y and z planes, ”ANGLExy1” and ”ANGLEz1”, corresponding to an in-plane field with a positive x-axis component and no y-axis or z-axis components.

The defect is formed from the ”cylinder” shapes defined in b-i and are subtracted from the ”cuboid” defined in a. The parameters of the cylinder are: cylinder(diameter,thickness) and are positioned with the ”transl” function, of which has parameters: transl(x,y,z).

Multiple regions are defined with the ”DefRegion” function and correspond to

the 16 vertical layers within the grid, with each region corresponding to 5 nm of the 80 nm thick element. These are used for applying different field strengths to each layer based on the 1/r weakening from bottom to top, as shown in the section stating ”B_ext.SetRegion...”, where ”B_ext” is the function creating the magnetic field within the defined region ”SetRegion”.

The ”tableadd(...)” function is used to add the values of the specified parameter to a .txt file at each interval of the simulation, defined by ”SAMPLE_PERIOD”. Images in .jpg or .png format are saved at each simulation interval by the function ”autosnapshot(...,SAMPLE_PERIOD)”, whilst ”autosave(...,SAMPLE_PERIOD)” saves images in the .ovf format which is useful for analysing the image in MatLab.

Planar bias field components are defined by the values ”bx1”, ”by1” and ”bz1” for the first magnetic pulse and are used in the ”B_ext.SetRegion(...” section for applying the correct field strengths in each dimension.

Finally the simulation is run with the ”run(time)” command for the defined number of seconds, after which the final magnetic state is saved in .ovf format with the ”save(m)” function. This is so that it could be used as the initial state in a subsequent simulation should it be necessary, without the need to re-run this particular part of the simulation. The same is done before the simulation starts with the same command but stated before the run command within the script for a similar reason.

$setGridSize(512, 512, 16)$

$setCellSize(3.90625e-9, 3.90625e-9, 5e-9)$

$//\ Independant\ variables$

$DELAYA := 50e-12$

$WIDTH1 := 10e-9$

$AMP1 := 0.008$

$ANGLEz1 := (0 * pi/180)$

$ANGLExy1 := (0 * pi/180)$

$DELAYB := 21e-9$

$WIDTH2 := 3e-9$

$AMP2 := 0.013$

$ANGLEz2 := (0 * pi/180)$

$ANGLExy2 := (0 * pi/180)$

$DELAYC := 25e-9$

$WIDTH3 := 3e-9$

$AMP3 := 0.013$

$ANGLEz3 := (0 * pi/180)$

$ANGLExy3 := (0 * pi/180)$

$RISE := 1e-9$

$//\ Parameters\ to\ remain\ constant\ in\ time$

$//\ Permalloy\ rectangle\ dimension\ in\ m$

$//EDGE\_LENGTH := 2000e-9$

$//DEPTH := 80e-9$

$a := cuboid(2000e-9, 2000e-9, 80e-9)$

$b := cylinder(100e-9, 5e-9).transl(0, 200e-9, 2.5e-9)$

$c := cylinder(104.79e-9, 5e-9).transl(0, 200e-9, 7.5e-9)$

$d := cylinder(109.59e-9, 5e-9).transl(0, 200e-9, 12.5e-9)$

$e := cylinder(114.38e-9, 5e-9).transl(0, 200e-9, 17.5e-9)$

$f := cylinder(119.18e-9, 5e-9).transl(0, 200e-9, 22.5e-9)$

$g := cylinder(123.97e-9, 5e-9).transl(0, 200e-9, 27.5e-9)$

$h := cylinder(128.77e-9, 5e-9).transl(0, 200e-9, 32.5e-9)$

$i := cylinder(133.56e-9, 5e-9).transl(0, 200e-9, 37.5e-9)$

$setgeom(a.sub(b).sub(c).sub(d).sub(e).sub(f).sub(g).sub(h).sub(i))$

$saveas(geom, "cuboid")$

$// Permalloy\ material\ properties$

$msat = 8e5\ A/m\ Magnetisation\ Saturation$

$aex = 13e-12\ Exchange\ stiffness$

$alpha = 0.008\ Gilbert\ damping$

$// Define\ regions\ for\ 1/r$

$DefRegion(1, zrange(-40e-9, -35e-9))$

$DefRegion(2, zrange(-35e-9, -30e-9))$

$DefRegion(3, zrange(-30e-9, -25e-9))$

$DefRegion(4, zrange(-25e-9, -20e-9))$

$DefRegion(5, zrange(-20e-9, -15e-9))$

$DefRegion(6, zrange(-15e-9, -10e-9))$

$DefRegion(7, zrange(-10e-9, -5e-9))$

$DefRegion(8, zrange(-5e-9, 0e-9))$

$DefRegion(9, zrange(0e-9, 5e-9))$

$DefRegion(10, zrange(5e-9, 10e-9))$

$DefRegion(11, zrange(10e-9, 15e-9))$

$DefRegion(12, zrange(15e-9, 20e-9))$

$DefRegion(13, zrange(20e-9, 25e-9))$

$DefRegion(14, zrange(25e-9, 30e-9))$

$DefRegion(15, zrange(30e-9, 35e-9))$

$DefRegion(16, zrange(35e-9, 40e-9))$

$// Select table output$

$tableadd(E\_total)$

$tableadd(B\_exch)$

$tableadd(B\_demag)$

$tableadd(B\_anis)$

$tableadd(torque)$

$tableadd(LLtorque)$

$tableadd(maxTorque)$

$// Select save frame rate in s$

$SAMPLE\_PERIOD := 50e-12$

$//Chooseimageoutput$

$autosnapshot(m, SAMPLE\_PERIOD)$

$autosnapshot(torque, SAMPLE\_PERIOD)$

$autosnapshot(B_demag, SAMPLE\_PERIOD)$

$autosnapshot(B_exch, SAMPLE\_PERIOD)$

$autosave(Crop(m, 0, 512, 0, 512, 7, 8), SAMPLE\_PERIOD)$

$tableautosave(SAMPLE\_PERIOD)$

$//Load\ relaxed\ initial\ state$

$//m = vortex(1, 1)\ //\ vortex(chirality, polarity)$

$//minimize()$

$//save(m)$

$m.LoadFile("initial.ovf")$

$bx1 := cos(ANGLEz1) * cos(ANGLExy1)$

$by1 := cos(ANGLEz1) * sin(ANGLExy1)$

$bz1 := sin(ANGLEz1)$

$bx2 := cos(ANGLEz2) * cos(ANGLExy2)$

$by2 := cos(ANGLEz2) * sin(ANGLExy2)$

$bz2 := sin(ANGLEz2)$

$bx3 := cos(ANGLEz3) * cos(ANGLExy3)$

$by3 := cos(ANGLEz3) * sin(ANGLExy3)$

$bz3 := sin(ANGLEz3)$

$//\ Define\ temporal\ profile\ of\ excitiaton$

$//bt1 := ((AMP1)/4*(2-erfc((t-DELAYA)/(RISE)))*erfc((t-DELAYA-WIDTH1)/(RISE)))$

$//bt2 := ((AMP2)/4*(2-erfc((t-DELAYB)/(RISE)))*erfc((t-DELAYB-WIDTH2)/(RISE)))$

$//bt3 := ((AMP3)/4*(2-erfc((t-DELAYC)/(RISE)))*erfc((t-DELAYB-WIDTH3)/(RISE)))$

$// Implememnt\ excitation\ field$

$// Normal\ bias\ field\ strength$

$//B_ext = vector((bx*bt1+bx*bt2),(by*bt1+by*bt2),(bz*bt1+bz*bt2))$

$// Bias\ field\ with\ 1/r\ strength\ reduction$

$B\_ext.SetRegion(1, vector((((1/((1)+0*(0.1875)))*bx1*((AMP1)/4*(2-erfc((t-DELAYA)/(RISE)))*erfc((t-DELAYA-WIDTH1)/(RISE))))+((1/((1)+0*(0.1875)))*bx2*((AMP2)/4*(2-erfc((t-DELAYB)/(RISE)))*erfc((t-DELAYB-WIDTH2)/(RISE))))+((1/((1)+0*(0.1875)))*bx3*((AMP3)/4*(2-erfc((t-DELAYC)/(RISE)))*erfc((t-DELAYC-WIDTH3)/(RISE))))),(((1/((1)+0*(0.1875)))*by1*((AMP1)/4*(2-erfc((t-DELAYA)/(RISE)))*erfc((t-DELAYA-WIDTH1)/(RISE))))+((1/((1)+0*(0.1875)))*by2*((AMP2)/4*(2-erfc((t-DELAYB)/(RISE)))*erfc((t-DELAYB-WIDTH2)/(RISE))))+((1/((1)+0*(0.1875)))*by3*((AMP3)/4*(2-erfc((t-DELAYC)/(RISE)))*erfc((t-DELAYC-WIDTH3)/(RISE))))),(((1/((1)+0*(0.1875)))*bz1*((AMP1)/4*(2-erfc((t-DELAYA)/(RISE)))*erfc((t-DELAYA-WIDTH1)/(RISE))))+((1/((1)+0*(0.1875)))*bz2*((AMP2)/4*(2-erfc((t-DELAYB)/(RISE)))*erfc((t-DELAYB-WIDTH2)/(RISE))))+((1/((1)+0*(0.1875)))*bz3*((AMP3)/4*(2-erfc((t-DELAYC)/(RISE)))*erfc((t-DELAYC-WIDTH3)/(RISE)))))))$

$B\_ext.SetRegion(2, vector((((1/((1)+1*(0.1875)))*bx1*((AMP1)/4*(2-erfc((t-DELAYA)/(RISE)))*erfc((t-DELAYA-WIDTH1)/(RISE))))+((1/((1)+1*(0.1875)))*bx2*((AMP2)/4*(2-erfc((t-DELAYB)/(RISE)))*erfc((t-DELAYB-WIDTH2)/(RISE))))+((1/((1)+1*(0.1875)))*bx3*((AMP3)/4*(2-erfc((t-DELAYC)/(RISE)))*erfc((t-DELAYC-$

$WIDTH3)/(RISE))))), (((1/((1)+1*(0.1875)))*by1*((AMP1)/4*(2-erfc((t-DELAYA)/(RISE)))*erfc((t-DELAYA-WIDTH1)/(RISE))))+((1/((1)+1*(0.1875)))*by2*((AMP2)/4*(2-erfc((t-DELAYB)/(RISE)))*erfc((t-DELAYB-WIDTH2)/(RISE))))+((1/((1)+1*(0.1875)))*by3*((AMP3)/4*(2-erfc((t-DELAYC)/(RISE)))*erfc((t-DELAYC-WIDTH3)/(RISE))))), (((1/((1)+1*(0.1875)))*bz1*((AMP1)/4*(2-erfc((t-DELAYA)/(RISE)))*erfc((t-DELAYA-WIDTH1)/(RISE))))+((1/((1)+1*(0.1875)))*bz2*((AMP2)/4*(2-erfc((t-DELAYB)/(RISE)))*erfc((t-DELAYB-WIDTH2)/(RISE))))+((1/((1)+1*(0.1875)))*bz3*((AMP3)/4*(2-erfc((t-DELAYC)/(RISE)))*erfc((t-DELAYC-WIDTH3)/(RISE)))))))$

$B\_ext.SetRegion(3, vector((((1/((1)+2*(0.1875)))*bx1*((AMP1)/4*(2-erfc((t-DELAYA)/(RISE)))*erfc((t-DELAYA-WIDTH1)/(RISE))))+((1/((1)+2*(0.1875)))*bx2*((AMP2)/4*(2-erfc((t-DELAYB)/(RISE)))*erfc((t-DELAYB-WIDTH2)/(RISE))))+((1/((1)+2*(0.1875)))*bx3*((AMP3)/4*(2-erfc((t-DELAYC)/(RISE)))*erfc((t-DELAYC-WIDTH3)/(RISE))))), (((1/((1)+2*(0.1875)))*by1*((AMP1)/4*(2-erfc((t-DELAYA)/(RISE)))*erfc((t-DELAYA-WIDTH1)/(RISE))))+((1/((1)+2*(0.1875)))*by2*((AMP2)/4*(2-erfc((t-DELAYB)/(RISE)))*erfc((t-DELAYB-WIDTH2)/(RISE))))+((1/((1)+2*(0.1875)))*by3*((AMP3)/4*(2-erfc((t-DELAYC)/(RISE)))*erfc((t-DELAYC-WIDTH3)/(RISE))))), (((1/((1)+2*(0.1875)))*bz1*((AMP1)/4*(2-erfc((t-DELAYA)/(RISE)))*erfc((t-DELAYA-WIDTH1)/(RISE))))+((1/((1)+2*(0.1875)))*bz2*((AMP2)/4*(2-erfc((t-DELAYB)/(RISE)))*erfc((t-DELAYB-WIDTH2)/(RISE))))+((1/((1)+2*(0.1875)))*bz3*((AMP3)/4*(2-erfc((t-DELAYC)/(RISE)))*erfc((t-DELAYC-WIDTH3)/(RISE)))))))$

$B\_ext.SetRegion(4, vector((((1/((1)+3*(0.1875)))*bx1*((AMP1)/4*(2-erfc((t-DELAYA)/(RISE)))*erfc((t-DELAYA-WIDTH1)/(RISE))))+((1/((1)+3*(0.1875)))*bx2*((AMP2)/4*(2-erfc((t-DELAYB)/(RISE)))*erfc((t-DELAYB-WIDTH2)/(RISE))))+((1/((1)+3*(0.1875)))*bx3*$

$((AMP3)/4 * (2 - erfc((t - DELAYC)/(RISE))) * erfc((t - DELAYC - WIDTH3)/(RISE)))))), (((1/((1) + 3 * (0.1875))) * by1 * ((AMP1)/4 * (2 - erfc((t - DELAYA)/(RISE))) * erfc((t - DELAYA - WIDTH1)/(RISE)))) + ((1/((1) + 3 * (0.1875))) * by2 * ((AMP2)/4 * (2 - erfc((t - DELAYB)/(RISE))) * erfc((t - DELAYB - WIDTH2)/(RISE)))) + ((1/((1) + 3 * (0.1875))) * by3 * ((AMP3)/4 * (2 - erfc((t - DELAYC)/(RISE))) * erfc((t - DELAYC - WIDTH3)/(RISE)))))), (((1/((1) + 3 * (0.1875))) * bz1 * ((AMP1)/4 * (2 - erfc((t - DELAYA)/(RISE))) * erfc((t - DELAYA - WIDTH1)/(RISE)))) + ((1/((1) + 3 * (0.1875))) * bz2 * ((AMP2)/4 * (2 - erfc((t - DELAYB)/(RISE))) * erfc((t - DELAYB - WIDTH2)/(RISE)))) + ((1/((1) + 3 * (0.1875))) * bz3 * ((AMP3)/4 * (2 - erfc((t - DELAYC)/(RISE))) * erfc((t - DELAYC - WIDTH3)/(RISE)))))))$

$B\_ext.SetRegion(5, vector((((1/((1) + 4 * (0.1875))) * bx1 * ((AMP1)/4 * (2 - erfc((t - DELAYA)/(RISE))) * erfc((t - DELAYA - WIDTH1)/(RISE)))) + ((1/((1) + 4 * (0.1875))) * bx2 * ((AMP2)/4 * (2 - erfc((t - DELAYB)/(RISE))) * erfc((t - DELAYB - WIDTH2)/(RISE)))) + ((1/((1) + 4 * (0.1875))) * bx3 * ((AMP3)/4 * (2 - erfc((t - DELAYC)/(RISE))) * erfc((t - DELAYC - WIDTH3)/(RISE)))))), (((1/((1) + 4 * (0.1875))) * by1 * ((AMP1)/4 * (2 - erfc((t - DELAYA)/(RISE))) * erfc((t - DELAYA - WIDTH1)/(RISE)))) + ((1/((1) + 4 * (0.1875))) * by2 * ((AMP2)/4 * (2 - erfc((t - DELAYB)/(RISE))) * erfc((t - DELAYB - WIDTH2)/(RISE)))) + ((1/((1) + 4 * (0.1875))) * by3 * ((AMP3)/4 * (2 - erfc((t - DELAYC)/(RISE))) * erfc((t - DELAYC - WIDTH3)/(RISE)))))), (((1/((1) + 4 * (0.1875))) * bz1 * ((AMP1)/4 * (2 - erfc((t - DELAYA)/(RISE))) * erfc((t - DELAYA - WIDTH1)/(RISE)))) + ((1/((1) + 4 * (0.1875))) * bz2 * ((AMP2)/4 * (2 - erfc((t - DELAYB)/(RISE))) * erfc((t - DELAYB - WIDTH2)/(RISE)))) + ((1/((1) + 4 * (0.1875))) * bz3 * ((AMP3)/4 * (2 - erfc((t - DELAYC)/(RISE))) * erfc((t - DELAYC - WIDTH3)/(RISE)))))))$

$B\_ext.SetRegion(6, vector((((1/((1) + 5 * (0.1875))) * bx1 * ((AMP1)/4 * (2 - erfc((t - DELAYA)/(RISE))) * erfc((t - DELAYA - WIDTH1)/(RISE)))) + ((1/((1) + 5 * (0.1875))) * bx2 * ((AMP2)/4 * (2 - erfc((t - DELAYB)/(RISE))) *$

$erfc((t-DELAYB-WIDTH2)/(RISE)))) + ((1/((1)+5*(0.1875))) * bx3 *$
$((AMP3)/4 * (2 - erfc((t-DELAYC)/(RISE))) * erfc((t-DELAYC -$
$WIDTH3)/(RISE))))), (((1/((1)+5*(0.1875))) * by1 * ((AMP1)/4 * (2 -$
$erfc((t-DELAYA)/(RISE))) * erfc((t-DELAYA-WIDTH1)/(RISE)))) +$
$((1/((1)+5*(0.1875))) * by2 * ((AMP2)/4 * (2 - erfc((t-DELAYB)/(RISE))) *$
$erfc((t-DELAYB-WIDTH2)/(RISE)))) + ((1/((1)+5*(0.1875))) * by3 *$
$((AMP3)/4 * (2 - erfc((t-DELAYC)/(RISE))) * erfc((t-DELAYC -$
$WIDTH3)/(RISE))))), (((1/((1)+5*(0.1875))) * bz1 * ((AMP1)/4 * (2 - erfc((t -$
$DELAYA)/(RISE))) * erfc((t-DELAYA-WIDTH1)/(RISE)))) + ((1/((1) +$
$5*(0.1875))) * bz2 * ((AMP2)/4 * (2 - erfc((t-DELAYB)/(RISE))) * erfc((t -$
$DELAYB-WIDTH2)/(RISE)))) + ((1/((1)+5*(0.1875))) * bz3 * ((AMP3)/4 * (2 -$
$erfc((t-DELAYC)/(RISE))) * erfc((t-DELAYC-WIDTH3)/(RISE)))))))$

$B\_ext.SetRegion(7, vector((((1/((1)+6*(0.1875))) * bx1 * ((AMP1)/4 * (2 -$
$erfc((t-DELAYA)/(RISE))) * erfc((t-DELAYA-WIDTH1)/(RISE)))) +$
$((1/((1)+6*(0.1875))) * bx2 * ((AMP2)/4 * (2 - erfc((t-DELAYB)/(RISE))) *$
$erfc((t-DELAYB-WIDTH2)/(RISE)))) + ((1/((1)+6*(0.1875))) * bx3 *$
$((AMP3)/4 * (2 - erfc((t-DELAYC)/(RISE))) * erfc((t-DELAYC -$
$WIDTH3)/(RISE))))), (((1/((1)+6*(0.1875))) * by1 * ((AMP1)/4 * (2 -$
$erfc((t-DELAYA)/(RISE))) * erfc((t-DELAYA-WIDTH1)/(RISE)))) +$
$((1/((1)+6*(0.1875))) * by2 * ((AMP2)/4 * (2 - erfc((t-DELAYB)/(RISE))) *$
$erfc((t-DELAYB-WIDTH2)/(RISE)))) + ((1/((1)+6*(0.1875))) * by3 *$
$((AMP3)/4 * (2 - erfc((t-DELAYC)/(RISE))) * erfc((t-DELAYC -$
$WIDTH3)/(RISE))))), (((1/((1)+6*(0.1875))) * bz1 * ((AMP1)/4 * (2 - erfc((t -$
$DELAYA)/(RISE))) * erfc((t-DELAYA-WIDTH1)/(RISE)))) + ((1/((1) +$
$6*(0.1875))) * bz2 * ((AMP2)/4 * (2 - erfc((t-DELAYB)/(RISE))) * erfc((t -$
$DELAYB-WIDTH2)/(RISE)))) + ((1/((1)+6*(0.1875))) * bz3 * ((AMP3)/4 * (2 -$
$erfc((t-DELAYC)/(RISE))) * erfc((t-DELAYC-WIDTH3)/(RISE)))))))$

$B\_ext.SetRegion(8, vector((((1/((1)+7*(0.1875))) * bx1 * ((AMP1)/4 * (2 -$
$erfc((t-DELAYA)/(RISE))) * erfc((t-DELAYA-WIDTH1)/(RISE)))) +$

$((1/((1)+7*(0.1875)))*bx2*((AMP2)/4*(2-erfc((t-DELAYB)/(RISE)))*erfc((t-DELAYB-WIDTH2)/(RISE))))+((1/((1)+7*(0.1875)))*bx3*((AMP3)/4*(2-erfc((t-DELAYC)/(RISE)))*erfc((t-DELAYC-WIDTH3)/(RISE))))),(((1/((1)+7*(0.1875)))*by1*((AMP1)/4*(2-erfc((t-DELAYA)/(RISE)))*erfc((t-DELAYA-WIDTH1)/(RISE))))+((1/((1)+7*(0.1875)))*by2*((AMP2)/4*(2-erfc((t-DELAYB)/(RISE)))*erfc((t-DELAYB-WIDTH2)/(RISE))))+((1/((1)+7*(0.1875)))*by3*((AMP3)/4*(2-erfc((t-DELAYC)/(RISE)))*erfc((t-DELAYC-WIDTH3)/(RISE))))),(((1/((1)+7*(0.1875)))*bz1*((AMP1)/4*(2-erfc((t-DELAYA)/(RISE)))*erfc((t-DELAYA-WIDTH1)/(RISE))))+((1/((1)+7*(0.1875)))*bz2*((AMP2)/4*(2-erfc((t-DELAYB)/(RISE)))*erfc((t-DELAYB-WIDTH2)/(RISE))))+((1/((1)+7*(0.1875)))*bz3*((AMP3)/4*(2-erfc((t-DELAYC)/(RISE)))*erfc((t-DELAYC-WIDTH3)/(RISE)))))))$

$B\_ext.SetRegion(9,vector((((1/((1)+8*(0.1875)))*bx1*((AMP1)/4*(2-erfc((t-DELAYA)/(RISE)))*erfc((t-DELAYA-WIDTH1)/(RISE))))+((1/((1)+8*(0.1875)))*bx2*((AMP2)/4*(2-erfc((t-DELAYB)/(RISE)))*erfc((t-DELAYB-WIDTH2)/(RISE))))+((1/((1)+8*(0.1875)))*bx3*((AMP3)/4*(2-erfc((t-DELAYC)/(RISE)))*erfc((t-DELAYC-WIDTH3)/(RISE))))),(((1/((1)+8*(0.1875)))*by1*((AMP1)/4*(2-erfc((t-DELAYA)/(RISE)))*erfc((t-DELAYA-WIDTH1)/(RISE))))+((1/((1)+8*(0.1875)))*by2*((AMP2)/4*(2-erfc((t-DELAYB)/(RISE)))*erfc((t-DELAYB-WIDTH2)/(RISE))))+((1/((1)+8*(0.1875)))*by3*((AMP3)/4*(2-erfc((t-DELAYC)/(RISE)))*erfc((t-DELAYC-WIDTH3)/(RISE))))),(((1/((1)+8*(0.1875)))*bz1*((AMP1)/4*(2-erfc((t-DELAYA)/(RISE)))*erfc((t-DELAYA-WIDTH1)/(RISE))))+((1/((1)+8*(0.1875)))*bz2*((AMP2)/4*(2-erfc((t-DELAYB)/(RISE)))*erfc((t-DELAYB-WIDTH2)/(RISE))))+((1/((1)+8*(0.1875)))*bz3*((AMP3)/4*(2-erfc((t-DELAYC)/(RISE)))*erfc((t-DELAYC-WIDTH3)/(RISE)))))))$

$B\_ext.SetRegion(10,vector((((1/((1)+9*(0.1875)))*bx1*((AMP1)/4*(2-$

$erfc((t-DELAYA)/(RISE))) * erfc((t-DELAYA-WIDTH1)/(RISE)))) +$
$((1/((1)+9*(0.1875))) * bx2 * ((AMP2)/4 * (2-erfc((t-DELAYB)/(RISE))) *$
$erfc((t-DELAYB-WIDTH2)/(RISE)))) + ((1/((1)+9*(0.1875))) * bx3 *$
$((AMP3)/4 * (2-erfc((t-DELAYC)/(RISE))) * erfc((t-DELAYC-$
$WIDTH3)/(RISE))))), (((1/((1)+9*(0.1875))) * by1 * ((AMP1)/4 * (2-$
$erfc((t-DELAYA)/(RISE))) * erfc((t-DELAYA-WIDTH1)/(RISE)))) +$
$((1/((1)+9*(0.1875))) * by2 * ((AMP2)/4 * (2-erfc((t-DELAYB)/(RISE))) *$
$erfc((t-DELAYB-WIDTH2)/(RISE)))) + ((1/((1)+9*(0.1875))) * by3 *$
$((AMP3)/4 * (2-erfc((t-DELAYC)/(RISE))) * erfc((t-DELAYC-$
$WIDTH3)/(RISE))))), (((1/((1)+9*(0.1875))) * bz1 * ((AMP1)/4 * (2-erfc((t-$
$DELAYA)/(RISE))) * erfc((t-DELAYA-WIDTH1)/(RISE)))) + ((1/((1)+$
$9*(0.1875))) * bz2 * ((AMP2)/4 * (2-erfc((t-DELAYB)/(RISE))) * erfc((t-$
$DELAYB-WIDTH2)/(RISE))))+((1/((1)+9*(0.1875))) * bz3 * ((AMP3)/4 * (2-$
$erfc((t-DELAYC)/(RISE))) * erfc((t-DELAYC-WIDTH3)/(RISE)))))))$

$B\_ext.SetRegion(11, vector((((1/((1)+10*(0.1875))) * bx1 * ((AMP1)/4 * (2-$
$erfc((t-DELAYA)/(RISE))) * erfc((t-DELAYA-WIDTH1)/(RISE)))) +$
$((1/((1)+10*(0.1875))) * bx2 * ((AMP2)/4 * (2-erfc((t-$
$DELAYB)/(RISE))) * erfc((t-DELAYB-WIDTH2)/(RISE)))) + ((1/((1)+$
$10*(0.1875))) * bx3 * ((AMP3)/4 * (2-erfc((t-DELAYC)/(RISE))) *$
$erfc((t-DELAYC-WIDTH3)/(RISE))))), (((1/((1)+10*(0.1875))) * by1 *$
$((AMP1)/4 * (2-erfc((t-DELAYA)/(RISE))) * erfc((t-DELAYA-$
$WIDTH1)/(RISE)))) + ((1/((1)+10*(0.1875))) * by2 * ((AMP2)/4 * (2-$
$erfc((t-DELAYB)/(RISE))) * erfc((t-DELAYB-WIDTH2)/(RISE)))) +$
$((1/((1)+10*(0.1875))) * by3 * ((AMP3)/4 * (2-erfc((t-DELAYC)/(RISE))) *$
$erfc((t-DELAYC-WIDTH3)/(RISE))))), (((1/((1)+10*(0.1875))) * bz1 *$
$((AMP1)/4 * (2-erfc((t-DELAYA)/(RISE))) * erfc((t-DELAYA-$
$WIDTH1)/(RISE)))) + ((1/((1)+10*(0.1875))) * bz2 * ((AMP2)/4 * (2-$
$erfc((t-DELAYB)/(RISE))) * erfc((t-DELAYB-WIDTH2)/(RISE)))) +$
$((1/((1)+10*(0.1875))) * bz3 * ((AMP3)/4 * (2-erfc((t-$
$DELAYC)/(RISE))) * erfc((t-DELAYC-WIDTH3)/(RISE)))))))$

$$B\_ext.SetRegion(12, vector((((1/((1)+11*(0.1875)))*bx1*((AMP1)/4*(2-erfc((t-DELAYA)/(RISE)))*erfc((t-DELAYA-WIDTH1)/(RISE))))+((1/((1)+11*(0.1875)))*bx2*((AMP2)/4*(2-erfc((t-DELAYB)/(RISE)))*erfc((t-DELAYB-WIDTH2)/(RISE))))+((1/((1)+11*(0.1875)))*bx3*((AMP3)/4*(2-erfc((t-DELAYC)/(RISE)))*erfc((t-DELAYC-WIDTH3)/(RISE))))),(((1/((1)+11*(0.1875)))*by1*((AMP1)/4*(2-erfc((t-DELAYA)/(RISE)))*erfc((t-DELAYA-WIDTH1)/(RISE))))+((1/((1)+11*(0.1875)))*by2*((AMP2)/4*(2-erfc((t-DELAYB)/(RISE)))*erfc((t-DELAYB-WIDTH2)/(RISE))))+((1/((1)+11*(0.1875)))*by3*((AMP3)/4*(2-erfc((t-DELAYC)/(RISE)))*erfc((t-DELAYC-WIDTH3)/(RISE))))),(((1/((1)+11*(0.1875)))*bz1*((AMP1)/4*(2-erfc((t-DELAYA)/(RISE)))*erfc((t-DELAYA-WIDTH1)/(RISE))))+((1/((1)+11*(0.1875)))*bz2*((AMP2)/4*(2-erfc((t-DELAYB)/(RISE)))*erfc((t-DELAYB-WIDTH2)/(RISE))))+((1/((1)+11*(0.1875)))*bz3*((AMP3)/4*(2-erfc((t-DELAYC)/(RISE)))*erfc((t-DELAYC-WIDTH3)/(RISE)))))))$$

$$B\_ext.SetRegion(13, vector((((1/((1)+12*(0.1875)))*bx1*((AMP1)/4*(2-erfc((t-DELAYA)/(RISE)))*erfc((t-DELAYA-WIDTH1)/(RISE))))+((1/((1)+12*(0.1875)))*bx2*((AMP2)/4*(2-erfc((t-DELAYB)/(RISE)))*erfc((t-DELAYB-WIDTH2)/(RISE))))+((1/((1)+12*(0.1875)))*bx3*((AMP3)/4*(2-erfc((t-DELAYC)/(RISE)))*erfc((t-DELAYC-WIDTH3)/(RISE))))),(((1/((1)+12*(0.1875)))*by1*((AMP1)/4*(2-erfc((t-DELAYA)/(RISE)))*erfc((t-DELAYA-WIDTH1)/(RISE))))+((1/((1)+12*(0.1875)))*by2*((AMP2)/4*(2-erfc((t-DELAYB)/(RISE)))*erfc((t-DELAYB-WIDTH2)/(RISE))))+((1/((1)+12*(0.1875)))*by3*((AMP3)/4*(2-erfc((t-DELAYC)/(RISE)))*erfc((t-DELAYC-WIDTH3)/(RISE))))),(((1/((1)+12*(0.1875)))*bz1*((AMP1)/4*(2-erfc((t-DELAYA)/(RISE)))*erfc((t-DELAYA-WIDTH1)/(RISE))))+((1/((1)+12*(0.1875)))*bz2*((AMP2)/4*(2-erfc((t-DELAYB)/(RISE)))*erfc((t-DELAYB-WIDTH2)/(RISE))))+$$

$$((1/((1)+12*(0.1875)))*bz3*((AMP3)/4*(2-erfc((t-DELAYC)/(RISE)))*erfc((t-DELAYC-WIDTH3)/(RISE)))))))$$

$$B\_ext.SetRegion(14,vector((((1/((1)+13*(0.1875)))*bx1*((AMP1)/4*(2-erfc((t-DELAYA)/(RISE)))*erfc((t-DELAYA-WIDTH1)/(RISE))))+((1/((1)+13*(0.1875)))*bx2*((AMP2)/4*(2-erfc((t-DELAYB)/(RISE)))*erfc((t-DELAYB-WIDTH2)/(RISE))))+((1/((1)+13*(0.1875)))*bx3*((AMP3)/4*(2-erfc((t-DELAYC)/(RISE)))*erfc((t-DELAYC-WIDTH3)/(RISE))))),(((1/((1)+13*(0.1875)))*by1*((AMP1)/4*(2-erfc((t-DELAYA)/(RISE)))*erfc((t-DELAYA-WIDTH1)/(RISE))))+((1/((1)+13*(0.1875)))*by2*((AMP2)/4*(2-erfc((t-DELAYB)/(RISE)))*erfc((t-DELAYB-WIDTH2)/(RISE))))+((1/((1)+13*(0.1875)))*by3*((AMP3)/4*(2-erfc((t-DELAYC)/(RISE)))*erfc((t-DELAYC-WIDTH3)/(RISE))))),(((1/((1)+13*(0.1875)))*bz1*((AMP1)/4*(2-erfc((t-DELAYA)/(RISE)))*erfc((t-DELAYA-WIDTH1)/(RISE))))+((1/((1)+13*(0.1875)))*bz2*((AMP2)/4*(2-erfc((t-DELAYB)/(RISE)))*erfc((t-DELAYB-WIDTH2)/(RISE))))+((1/((1)+13*(0.1875)))*bz3*((AMP3)/4*(2-erfc((t-DELAYC)/(RISE)))*erfc((t-DELAYC-WIDTH3)/(RISE)))))))$$

$$B\_ext.SetRegion(15,vector((((1/((1)+14*(0.1875)))*bx1*((AMP1)/4*(2-erfc((t-DELAYA)/(RISE)))*erfc((t-DELAYA-WIDTH1)/(RISE))))+((1/((1)+14*(0.1875)))*bx2*((AMP2)/4*(2-erfc((t-DELAYB)/(RISE)))*erfc((t-DELAYB-WIDTH2)/(RISE))))+((1/((1)+14*(0.1875)))*bx3*((AMP3)/4*(2-erfc((t-DELAYC)/(RISE)))*erfc((t-DELAYC-WIDTH3)/(RISE))))),(((1/((1)+14*(0.1875)))*by1*((AMP1)/4*(2-erfc((t-DELAYA)/(RISE)))*erfc((t-DELAYA-WIDTH1)/(RISE))))+((1/((1)+14*(0.1875)))*by2*((AMP2)/4*(2-erfc((t-DELAYB)/(RISE)))*erfc((t-DELAYB-WIDTH2)/(RISE))))+((1/((1)+14*(0.1875)))*by3*((AMP3)/4*(2-erfc((t-DELAYC)/(RISE)))*erfc((t-DELAYC-WIDTH3)/(RISE))))),(((1/((1)+14*(0.1875)))*bz1*$$

$((AMP1)/4 * (2 - erfc((t - DELAYA)/(RISE))) * erfc((t - DELAYA - WIDTH1)/(RISE)))) + ((1/((1) + 14 * (0.1875))) * bz2 * ((AMP2)/4 * (2 - erfc((t - DELAYB)/(RISE))) * erfc((t - DELAYB - WIDTH2)/(RISE)))) + ((1/((1) + 14 * (0.1875))) * bz3 * ((AMP3)/4 * (2 - erfc((t - DELAYC)/(RISE))) * erfc((t - DELAYC - WIDTH3)/(RISE)))))))$

$B\_ext.SetRegion(16, vector((((1/((1) + 15 * (0.1875))) * bx1 * ((AMP1)/4 * (2 - erfc((t - DELAYA)/(RISE))) * erfc((t - DELAYA - WIDTH1)/(RISE)))) + ((1/((1) + 15 * (0.1875))) * bx2 * ((AMP2)/4 * (2 - erfc((t - DELAYB)/(RISE))) * erfc((t - DELAYB - WIDTH2)/(RISE)))) + ((1/((1) + 15 * (0.1875))) * bx3 * ((AMP3)/4 * (2 - erfc((t - DELAYC)/(RISE))) * erfc((t - DELAYC - WIDTH3)/(RISE))))), (((1/((1) + 15 * (0.1875))) * by1 * ((AMP1)/4 * (2 - erfc((t - DELAYA)/(RISE))) * erfc((t - DELAYA - WIDTH1)/(RISE)))) + ((1/((1) + 15 * (0.1875))) * by2 * ((AMP2)/4 * (2 - erfc((t - DELAYB)/(RISE))) * erfc((t - DELAYB - WIDTH2)/(RISE)))) + ((1/((1) + 15 * (0.1875))) * by3 * ((AMP3)/4 * (2 - erfc((t - DELAYC)/(RISE))) * erfc((t - DELAYC - WIDTH3)/(RISE))))), (((1/((1) + 15 * (0.1875))) * bz1 * ((AMP1)/4 * (2 - erfc((t - DELAYA)/(RISE))) * erfc((t - DELAYA - WIDTH1)/(RISE)))) + ((1/((1) + 15 * (0.1875))) * bz2 * ((AMP2)/4 * (2 - erfc((t - DELAYB)/(RISE))) * erfc((t - DELAYB - WIDTH2)/(RISE)))) + ((1/((1) + 15 * (0.1875))) * bz3 * ((AMP3)/4 * (2 - erfc((t - DELAYC)/(RISE))) * erfc((t - DELAYC - WIDTH3)/(RISE)))))))$

// Execute iteration

$run(15e - 9)$

$save(m)$

Appendix B

Parameters

B.1 FIB Defect Milling Parameters

FIB milling parameters were 30 kV, 50 pA for 100 passes as this produced a defect of depth of $\sim$40 nm $\pm$10 nm. A second generation of samples was produced that had different parameters; using a FIB beam of 30 kV, 50 pA and 500 passes. The difference was likely caused by a significant repair of the system over the time between milling sessions. Other parameters of the beam include; overlap x and y 50$\%$, pitch x and y 9.5 nm, volume per dose of 1.5$e^{-1}\mu m^3/nC$, loop time of 50 μs, area of 1.77 e^4nm^2, circular scan type, solid fill style, total diameter of 19 nm, saturation current density of 20nA/nm^2 and a total volume sputter rate of 7.5 e^6pm^3/nC.

B.2 Simulation Parameters

Material parameters for Py were $8e^5Am^{-1}$ for saturation magnetisation "msat", $13e^{-12}\,Jm^{-1}$ for the exchange stiffness constant "aex" and 0.008 for Gilbert damping "alpha". These are standard, accepted values for Py used elsewhere in published literature [142, 143]. Between different samples that were simulated the

main parameters that changed were those affecting sample geometry and magnetic pulse application, such as pulse amplitude and angle.

B.2.1 Grid and Cell Size

Values for cell dimensions were kept at or less than the materials exchange length of 5 nm since this is the scale upon which magnetism within the sample can vary. Therefore keeping to this length resulted in a more accurate representation of the magnetic vector interactions [144]. The scripts used to present data in this manuscript utilised a grid size of 512 x 512 or 1024 x 1024 in the x and y dimensions which allowed for a cell size of $2000/512 = 4000/1024 =$ **3.90625 nm** for a 2000 nm or 4000 nm wide simulation respectively. Grid height was 8 or 16 cells thick, resulting in a vertical cell size of $40/8 = 80/16 =$ **5 nm** for the z dimension of a 40 nm or 80 nm thick square respectively.

Magnetic pulse delay and width

The parameters "DELAYA" and "WIDTH1" define the time after the start of the simulation that the pulse begins to rise and for how long the pulse lasts, respectively, for the first pulse. "DELAYB" and "WIDTH2" are the same parameters for the second pulse and so on. "RISE" sets the rate in seconds at which the pulse rises from zero amplitude to maximum amplitude. Rise times of $0.2e^{-9}$, $1e^{-9}$ or $2e^{-9}$ were used to match those available from the Agilent 81150A pulse generator that created the magnetic pulses during experiments. With a rise time of $0.2e^{-9}$ the pulse caused the vortex polarity to switch immediately after gyration was initiated by the magnetic pulse. This was an issue when simulating polarity switching as the switch was investigated to arise from the presence of the physical defect and not from the pulse itself. Polarity switching via ultra-fast pulses has been previously documented [27, 42, 145].

Bibliography

[1] A. Aharoni. *Introduction to the Theory of Ferromagnetism*. Oxford University Press, 2nd edition, 2001.

[2] J. Stöhr and H. C. Siegmann. *Magnetism: from Fundamentals to Nanoscale Dynamics*. Springer-Verlag Berlin Heidelberg, 1 edition, 2006.

[3] G. Schönhense. Imaging of magnetic structures by photoemission electron microscopy. *Journal of Physics: Condensed Matter*, 11:9517–9547, 1999.

[4] C. Jacobsen. Soft x-ray microscopy. *Trends in Cell Biology*, 9:44–47, 1999.

[5] F. S. Jamaludin et. al. Controlling parameters of focussed ion beam (fib) on high aspect ratio mucro holes milling. *Microsystem Technologies*, 19:1873–1888, 2013.

[6] M. Madami et. al. Direct observation of a propagating spin wave induced by spin-transfer torque. *Nature Nanotechnology*, 6:635–638, 2011.

[7] V. S. Pribiag et. al. Magnetic vortex oscillator driven by d.c. spin-polarized current. *Nature Physics*, 3:498–503, 2007.

[8] A. Ruotolo et. al. Phase-locking of magnetic vortices mediated by antivortices. *Nature Nanotechnology*, 4:528–532, 2009.

[9] A. Dussaux et. al. Large microwave generation from current-driven magnetic vortex oscillators in magnetic tunnel junctions. *Nature Communications*, 1:1–6, 2010.

[10] C. Kittel. Theory of the structure of ferromagnetic domams in films and small particles. *Physical Review*, 70:965–971, 1946.

[11] B. E. Argyle et. el. Magnetic vortex dynamics using the optical cotton-mouton effect. *Physical Review Letters*, 53:190–194, 1984.

[12] S. Bohlens et. al. Current controlled random-access memory based on magnetic vortex handedness. *Applied Physics Letters*, 93:142508, 2008.

[13] A. Drews et. al. Current- and field-driven magnetic antivortices for non-volatile data storage. *Applied Physics Letters*, 94:062504, 2009.

[14] J. Han et. al. Skyrmion lattice in a two-dimensional chiral magnet. *Physical Review B*, 82:094429, 2010.

[15] F. Büttner et. al. Dynamics and inertia of skyrmionic spin structures. •*Nature Physics*, 11:225–228, 2015.

[16] J. Mulkers et. al. Cycloidal versus skyrmionic states in mesoscopic chiral magnets. *Physical Review B*, 93:1–8, 2016.

[17] A. Dussaux et. al. Phase locking of vortex based spin transfer oscillators to a microwave current. *Applied Physics Letters*, 98:132506, 2011.

[18] L. Landau and E Lifshits. On the theory of the dispersion of magnetic permeability in ferromagnetic bodies. *Phys. Zeitsch. der Sow.*, 8:153–169, 1935.

[19] T. Shinjo et. al. Magnetic vortex core observation in circular dots of permalloy. *Science*, 289:930–932, 2000.

[20] m. Rahm et. al. Vortex pinning at individual defects in magnetic nanodisks. *Journal of Applied Physics*, 93:7429–7431, 2003.

[21] M. Rahm et. al. Multistable switching due to magnetic vortices pinned at artificial pinning sites. *Applied Physics Letters*, 85:1553–1555, 2004.

[22] R. Silva et. al. Predicted defect-induced vortex core switching in thin magnetic nanodisks. *Physical Review B*, 78:054423, 2008.

[23] B. van Waeyenberge et. al. Magnetic vortex core reversal by excitation with short bursts of an alternating field. *Nature*, 444:461–464, 2006.

[24] Q. Xiao et. al. Dynamics of vortex core switching in ferromagnetic nanodisks. *Applied Physics Letters*, 89:262507, 2006.

[25] Q. Xiao et. al. Dynamics of magnetic vortex core switching in fe nanodisks by applying in-plane magnetic field pulse. *Journal of Applied Physics*, 102:103904, 2007.

[26] R. Hertel et. al. Ultrafast nanomagnetic toggle switching of vortex cores. *Physical Review Letters*, 98:117201, 2007.

[27] K. Lee et. al. Ultrafast vortex-core reversal dynamics in ferromagnetic nanodots. *Physical Review B*, 76:174410, 2007.

[28] V. Kravchuk et. al. Controlled vortex core switching in a magnetic nanodisk by a rotating field. *Journal of Applied Physics*, 102:043908, 2007.

[29] K. Yamada et. al. Electrical switching of the vortex core in a magnetic disk. *Nature Materials*, 6:270–273, 2007.

[30] S.-K. Kim et. al. Electric-current-driven vortex-core reversal in soft mahnetic nanodots. *Applied Physics Letters*, 91:082506, 2007.

[31] T. Kamionka et. al. Magnetic antivortex-core reversal by circular-rotational spin currents. *Physical Review Letters*, 105:137204, 2010.

[32] S. O. Demokritov and A. N. Slavin, editors. *Magnonics from Fundamentals to Applications*. Springer, 2013.

[33] J. A. Osborn. Demagnetizing factors of the general ellipsoid. *Physical Review*, 67:351–357, 1945.

[34] A. Hubert and R. Schäfer. *Magnetic Domains: The Analysis of Magnetic Microstructures*. Springer, 3rd edition, 2009.

[35] T. Trunk et. al. Domain wall structure in permalloy films with decreasing thickness at the bloch to néel transition. *Journal of Applied Physics*, 89:7606–7608, 2001.

[36] T. L. Gilbert. A phenomenological theory of damping in ferromagnetic materials. *IEEE Transactions on Magnetics*, 40:3443–3449, 2004.

[37] Y. Tserkovnyak et. al. Enhanced gilbert dampibg in thin ferromagnetic films. *Physical Review Letters*, 88:117601, 2002.

[38] A. Vansteenkiste. The design and verification of mumax3. *AIP Advances*, 4:107133, 2014.

[39] B. Dupé et. al. Engineering skyrmions in transition-metal multilayers for spintronics. *Nature Communications*, 7:11779, 2016.

[40] T. Okuno et. al. Mfm study of magnetic vortex cores in circular permalloy dots: behavior in external field. *Journal of Magnetism and Magnetic Materials*, 240:1–6, 2002.

[41] K.-S. Lee et. al. Gyrotropic linear and nonlinear motions of a magnetic vortex in soft magnetic nanodots. *Applied Physics Letters*, 91:132511, 2007.

[42] K. Guslienko et. al. Dynamic origin of vortex core switching in soft magnetic nanodots. *Physical Review Letters*, 100:027203, 2008.

[43] S. Wintz et. al. Magnetic vortex cores as tunable spin-wave emitters. *Nature Nanotechnology*, 11:1–7, 2016.

[44] V. Sluka et. al. Stacked topological spin textures as emitters for multidimensional spin wave modes. *2015 IEEE International Magnetics Conference (INTERMAG)*, 2015.

[45] M. Faraday. Experimental researches in electricity. *Philosophical Transactions of the Royal Society of London*, 136:1–20, 1846.

[46] J. Kerr. On rotation of the phase of polarization by reflection from the pole of a magnet. *Philosophical Magazine*, 5:321–343, 1877.

[47] A. Neudert et. al. Bloch-line generation in cross-tie walls by fast magnetic-field pulses. *Journal of Applied Physics*, 99:08F302, 2006.

[48] W. Yu et. al. Time resolved scanning kerr microscopy of hard disk writer structures with a multilayered yoke. *Applied Physics Letters*, 102:162407, 2013.

[49] Y. Au et. al. Direct excitation of propagating spin waves by focused ultra-short optical pulses. *Physical Review Letters*, 110:097201, 2013.

[50] Y. Au et. al. Observation of vortex dynamics in arrays of nanomagnets. *Physical Review B*, 91:174425, 2015.

[51] E. Beaurepaire et. al. Ultrafast spin dynamics in ferromagnetic nickel. *Physical Review Letters*, 76:4250–4253, 1996.

[52] M. R. Freeman et. al. Picosecond pulsed magnetic fields for studies of ultrafast magnetic phenomena. *IEEE Transactions on Magnetics*, 1991:4840–4182, 1991.

[53] P. Fischer. Magnetic imaging with polarized soft x-rays. *Journal of Physics D: Applied Physics*, 50:313002, 2017.

[54] J. J. Sáenz et. al. Observation of magnetic forces by the atomic force microscope. *Journal of Applied Physics*, 62:4293–4295, 1987.

[55] Y. Martin and H. K. Wickramasinghe. Magnetic imaging by ”force microscopy” with 1000 Å resolution. *Applied Physics Letters*, 50:1455–1457, 1987.

[56] M. R. Koblischka et. al. Improving the lateral resolution of the mfm technique to the 10nm range. *Journal of Magnetism and Magnetic Materials*, 272-276:2138–2140, 2004.

[57] P. Fischer et. al. Soft x-ray microscopy of nanomagnetism. *Materials Today*, 9(1-2):26–33, 2006.

[58] B. Thole et. al. Strong magnetic dichroism predicted in the m4,5 x-ray absorption spectra of magnetic rare-earth materials. *Physical Review Letters*, 55:2086–2088, 1985.

[59] G. van der Laan et. al. Experimental proof of magnetic x-ray dichroism. *Physical Review B*, 34:6529–6531, 1986.

[60] J. Stöhr. X-ray magnetic circular dichroism spectroscopy of transition metal thin films. *Journal of Electron Spectroscopy and Related Phenomena*, 75:253–272, 1995.

[61] G. Schütz et. al. Absorption of circularly polarized x rays in iron. *Physical Review Letters*, 58:737–740, 1987.

[62] S. Eisebitt et. al. Polarization effects in coherent scattering from magnetic specimen: Implications for x-ray holography, lensless imaging, and correlation spectroscopy. *Physical Review B*, 68:104419, 2003.

[63] W. F. Schlotter et. al. Multiple reference fourier transform holography with soft x rays. *Applied Physics Letters*, 89:163112, 2006.

[64] S. Streit-Nierobisch et. al. Magnetic soft x-ray holography study of focussed ion beam-patterned co/pt multilayers. *Journal of Applied Physics*, 106:083909, 2009.

[65] U. Fano. Spin orientation of photoelectrons ejected by circularly polarized light. *Physical Review*, 178:131–136, 1969.

[66] J. Vogel et. al. Time-resolved magnetic domain imaging by x-ray photoemission electron microscopy. *Applied Physics Letters*, 82:2299–2301, 2003.

[67] D. Neeb et. al. Sub-nanosecond resolution x-ray magnetic circular dichroism photoemission electron microscopy of magnetization processes in a

permalloy ring. *Journal of Physics: Condensed Matter*, 17:S1381–S1395, 2005.

[68] G. Schönhense. Peem with high time resolution - imaging of transient processes and novel concepts of chromatic and spherical aberration correction. *Surfaces and Interfaces*, 38:1578–1587, 2006.

[69] L. Aballe et. al. The alba spectroscopic leem-peem experimental station: layout and performance. *Journal of Synchrotron Radiation*, 22:745–752, 2015.

[70] J. Kirz. Phase zone plates for x rays and the extreme uv. *Journal of the Optical Society of America*, 64:301–309, 1974.

[71] O. E. Myers. Studies of transmission zone plates. *American Journal of Physics*, 19:359, 1951.

[72] A. V. Baez. A study in diffraction microscopy with special reference to x-rays. *Journal of the Optical Society of America*, 1952.

[73] E. H. Anderson et. al. Nanofabrication and diffractive optics for high-resolution x-ray applications. *Journal of Vacuum Science and Technology B: Microelectronics and Nanometer Structures*, 18:2970–2975, 2000.

[74] W. Chao et. al. Soft x-ray microscopy at a spatial resolution better than 15 nm. *Nature Letters*, 435:1210–1213, 2005.

[75] A. R. Jones. The focal properties of phase zone plates. *Journal of Physics D: Applied Physics*, 1969.

[76] T. Eimüller et. al. Spin-reorientation transition in co/pt multilayers on nanospheres. *Physical Review B*, 77:134415, 2008.

[77] J. Kirz et. al. Soft x-ray microscopes and their biological applications. *Quarterly Reviews of Biophysics*, 28:33–130, 1995.

[78] P. Fischer et. al. X-ray imaging of vortex cores in confined magnetic structures. *Physical Review B*, 83:212402, 2011.

[79] S.-G. Je et. al. Electric current control of creation and annihilation of sub-100 nm magnetic bubbles examined by full-field transmission soft x-ray microscopy. *Current Applied Physics*, 2018.

[80] H. Stoll et. al. High-resolution imaging of fast magnetization dynamics in magnetic nanostructures. *Applied Physics Letters*, 84:3328–3330, 2004.

[81] A. Puzic et. al. Spatially resolved ferromagnetic resonance: Imaging of ferromagnetic eigenmodes. *Journal of Applied Physics*, 97:10E704, 2005.

[82] H. Jung et. al. Observation of coupled vortex gyrations by 70-ps-time- and 20-nm-space-resolved full-field magnetic transmission soft x-ray microscopy. *Applied Physics Letters*, 97:222502, 2010.

[83] J.-S. Kim et. al. Synchronous precessional motion of multiple domain walls in a ferromagnetic nanowire by perpendicular field pulses. *Nature Communications*, 5(3429):1–8, 2014.

[84] D. J. Stigliani et. al. Resolving power of a zone plate. *Journal of the Optical Society of America*, 57:610–613, 1967.

[85] W. Chao et. al. Real space soft x-ray imaging at 10 nm spatial resolution. *Optics Express*, 20:9777–9783, 2012.

[86] J. C. Andrews et. al. Full-field transmission x-ray microscopy at ssrl. *Journal of Physics: Conference Series*, 186:012002, 2009.

[87] S. Eisebitt et. al. Lensless imaging of magnetic nanostructures by x-ray spectro-holography. *Nature*, 432:885–888, 2004.

[88] C. Tieg et. al. Imaging the in-plane magnetization in a co microstructure by fourier transform holography. *Optics Express*, 18:27251–27256, 2010.

[89] C. M. Günther et. al. Microscopic reversal behavior of magnetically capped nanospheres. *Physical Review B*, 81:064411, 2010.

[90] D. Stickler et. al. Soft x-ray holographic microscopy. *Applied Physics Letters*, 96:042501, 2010.

[91] S. Schaffert et. al. High-resolution magnetic-domain imaging by fourier transform holography at 21 nm wavelength. *New Journal of Physics*, 15:093042, 2013.

[92] R. L. Sandberg et. al. Tabletop soft-x-ray fourier transform holography with 50 nm resolution. *Optics Letters*, 34:1618–1920, 2009.

[93] C. La-O-Vorakiat et. al. Ultrafast demagnetization dynamics at the m edges of magnetic elements observed using a tabletop high-harmonic soft x-ray source. *Physical Review Letters*, 103:257402, 2009.

[94] E. O. Burgos-Parra et. al. Holographic magnetic imaging of single-layer nanocontact spin-transfer oscillators. *IEEE Transactions on Magnetics*, 52:6500304, 2016.

[95] F. Büttner et. al. Automatable sample fabrication process for pump-probe x-ray holographic imaging. *Optics Express*, 21:30563–30572, 2013.

[96] M. Guizar-Sicairos and R. Fineup. Holography with extended reference by autocorrelation linear differential operation. *Optics Express*, 15:17592–17612, 2007.

[97] J. F. James. *A Student's Guide to Fourier Transforms: With Applications in Physics and Engineering*. Cambridge University Press, 2011.

[98] A. C. Thompson et. al. X-ray data booklet. Center for X-Ray Optics and Advanced Light Source, Laurence Berkley National Laboratory, University of California, Berkley, CA 94720, 2009.

[99] T. Duckworth et. al. Magnetic imaging by x-ray holography using extended references. *Optics Express*, 19:16223, 2011.

[100] T. Duckworth et. al. Holographic imaging of interlayer coupling in co/pt/nife. *New Journal of Physics*, 15:023045, 2013.

[101] N. Bukin et. al. Time-resolved imaging of magnetic vortex dynamics using holography with extended reference autocorrelation by linear differential operator. *Scientific Reports*, 6:36307, 2016.

[102] M. Bolte et. al. Time-resolved x-ray microscopy of spin-torque-induced magnetic vortex gyration. *Physical Review Letters*, 100:176601, 2008.

[103] S. Mühlbauer et. al. Skyrmion lattice in a chiral magnet. *Science*, 323:915–919, 2009.

[104] M. Kammerer. Magnetic vortex core reversal by excitation of spin waves. *Nature Communications*, 2:276–279, 2011.

[105] M. D. Stiles and J. Miltat. *Spin-Transfer Torque and Dynamics*, volume 3. Springer, 2006.

[106] S. Kiselev et. al. Microwave oscillations of a nanomagnet driven by a spin-polarized current. *Nature*, 425:380–383, 2003.

[107] J. Katine et. al. Current-driven magnetization reversal and spin-wave excitations in co /cu /co pillars. *Physical Review Letters*, 84:3149–3152, 2000.

[108] A. Bisig et. al. Direct imaging of current induced magnetic vortex gyration in an asymmetric potential well. *Applied Physics Letters*, 96:152506, 2010.

[109] M. Weigand et. al. Vortex core switching by coherent excitation with single in-plane magnetic field pulses. *Physical Review Letters*, 102:077201, 2009.

[110] B. C. Koop et. al. Static and dynamic properties of vortex pairs in asymmetric nanomagnets. *AIP Advances*, 6:056406, 2016.

[111] D. Han et. al. Wave modes of collective vortex gyration in dipolar-coupled-dot-array magnonic crystals. *Scientific reports*, 3:2262, 2013.

[112] A. Barman et. al. Gyration mode splitting in magnetostatically coupled magnetic vortices in an array. *Journal of Physics D: Applied Physics*, 43:422001, 2010.

[113] O. Sukhostavets et. al. Magnetic vortex excitation frequencies and eigenmodes in a pair of coupled circular dots. *Applied Physics Express*, 4:065003, 2011.

[114] H. Jung et. al. Tunable negligible-loss energy transfer between dipolar-coupled magnetic disks by stimulated vortex gyration. *Scientific Reports*, 1:59, 2011.

[115] Logic operations based on magnetic-vortex-state networks. H. jung et. al. *ACS Nano*, 6:3712–3717, 2012.

[116] A. Drews et. al. Nonlinear magnetic vortex gyration. *Physical Review B*, 85:144417, 2012.

[117] K. Y. Guslienko et. al. Nonlinear gyrotropic vortex dynamics in ferromagnetic dots. *Physical Review B*, 82:014402, 2010.

[118] P. S. Keatley et. al. Ultrafast magnetization dynamics of spintronic nanostructures. *Philosophical Transactions of the Royal Society A*, 369:3115–3135, 2011.

[119] J. Raabe et. al. Quantitative analysis of magnetic excitations in landau flux-closure structures using synchrotron-radiation microscopy. *Physical Review Letters*, 94:217204, 2005.

[120] R. Antos et. al. Magnetic vortex dynamics. *Journal of the Physical Society of Japan*, 77:031004, 2008.

[121] J. Raabe et. al. Magnetization pattern of ferromagnetic nanodisks. *Journal of Applied Physics*, 88:4437, 2000.

[122] V. Chembrolu et. al. Time-resolved x-ray imaging of magnetization dynamics in spin-transfer torque devices. *Physical Review B*, 80:024417, 2009.

[123] A. Vogel et. al. Signal transfer in a chain of stray-field coupled ferromagnetic squares. *Applied Physics Letters*, 99:042506, 2011.

[124] J. Ewald et. al. A full-field transmission x-ray microscope for time-resolved imaging of magnetic nanostructures. *AIP Conference Proceedings*, 1696:020005, 2016.

[125] P. Wessels et. al. Time-resolved imaging of domain pattern destruction and recovery via nonequilibrium magnetization states. *Physical Review B*, 90:184417, 2014.

[126] B. Van der Wiele et. al. Micromagnetic simulations on gpu, a case study: Vortex core switching by high-frequency magnetic fields. *IEEE Transactions on Magnetics*, 48:2068–2072, 2012.

[127] V. Estévez and L. Laurson. Head-to-head domain wall structures in wide permalloy strips. *Physical Review B*, 91:054407, 2015.

[128] T.-M. Liu et. al. Nanoscale confinement of all-optical magnetic switching in tbfeco - competition with nanoscale heterogeneity. *Nano Letters*, 15:6862–6868, 2015.

[129] G. van der Laan. Applications of soft x-ray magnetic dichroism. *Journal of Physics: Conference Series*, 430:012127, 2013.

[130] A. Scherz et. al. Phase imaging of magnetic nanostructures using resonant soft x-ray holography. *Physical Review B*, 76:214410, 2007.

[131] L. Müller et. al. Ultrafast dynamics of magnetic domain structures probed by coherent free-electron laser light. *Synchrotron Radiation News*, 26:27–32, 2013.

[132] A. Vansteenkiste. Influence of domain wall pinning on the dynamic behavior of magnetic vortex structures: Time-resolved scanning x-ray transmission microscopy in nife thin film structures. *Physical Review B*, 77:144420, 2008.

[133] V. Novosad et. al. Spin excitations of magnetic vortices in ferromagnetic nanodots. *Physical Review B*, 66:052407, 2002.

[134] W. Rave and A. Hubert. Magnetic ground state of a thin-film element. *IEEE Transactions on Magnetics*, 36:3886–3899, 2000.

[135] R. V. Velba et. al. Spin-wave excitation modes in thick vortex-state circular ferromagnetic nanodots. *Physical Review B*, 93:214437, 2016.

[136] S. Jain et. al. Coupled vortex oscillations in mesoscale ferromagnetic double-disk structures. *Physical Review B*, 86:214418, 2012.

[137] G. Mihajlovic et. al. Enhanced spin signals due to native oxide formation in ni80fe20/ag lateral spin valves. *Applied Physics Letters*, 97:112502, 2010.

[138] H. Koo et. al. Current-controlled bi-stable domain configurations in ni 81fe19 elements: An approach to magnetic memory devices. *Applied Physics Letters*, 81:862–868, 2002.

[139] U. Quietsch et. al. Domain wall induced modes of high-frequency response in ferromagnetic elements. *Journal of Applied Physics*, 100:093911, 2006.

[140] D.-H. Kim et. al. Magnetic vortex-antivortex dynamics on a picosecond timescale in a rectangular permalloy pattern. Technical Report LBNL-2459E, Lawrence Berkley National Laboratory, 2010.

[141] J. Lau et.al. Direct correlation of reversal rate dynamics to domain configurations in micron-sized permalloy elements. *Journal of Applied Physics*, 97:10E702, 2005.

[142] J. Leliaert et. al. Current-driven domain wall mobility in polycrystalline permalloy nanowires: A numerical study. *Journal of Applied Physics*, 115:233903, 2014.

[143] A. Baker et. al. Proposal of a micromagnetic standard problem for ferromagnetic resonance simulations. *Journal of Magnetism and Magnetic Materials*, 421:428–439, 2017.

[144] A. Vansteenkiste et. al. Implementation of a finite-difference micromagnetic model on gpu hardware. *International Journal of Numerical Modelling: Electronic Networks, Devices and Fields*, 26:366–375, 2012.

[145] R. Wang et. al. Sub-nanosecond switching of vortex cores using a resonant perpendicular magnetic field. *Applied Physics Letters*, 100:082402, 2012.